Hierarchical Design of Connected Cruise Control: Perception, Planning, and Execution

by

Linjun Zhang

A dissertation submitted in partial fulfillment
of the requirements for the degree of
Doctor of Philosophy
(Mechanical Engineering)
in the University of Michigan
2017

Doctoral Committee:

Assistant Professor Gábor Orosz, Chair
Dr. Mrdjan Jankovic, Ford Motor Company
Professor Jing Sun
Professor A. Galip Ulsoy

2017

To my parents,
Baoyou Zhang and Liqing E,
with gratitude and love.

ACKNOWLEDGMENTS

First of all, I would like to express my sincerest appreciation to my advisor Gábor Orosz, who brought me into the field of connected and automated vehicles. For the past four years, he had been providing me with insightful and enlightening advices about my research. It was his encouragement and support that made me complete a wide range of research in the design of connected and automated vehicles. I would also like to thank my committee members, Professor Galip Ulsoy, Professor Jing Sun, and Dr. Mrdjan Jankovic, for their insightful comments and constructive suggestions throughout the completion of my dissertation.

Secondly, I would like to thank the University of Michigan Transportation Research Institute (UMTRI) for sharing with us the experimental data collected in the Safety Pilot Project. These data played an important role in validating my algorithms. Moreover, I would like to thank my colleagues in the lab, Chaozhe He, Jin Ge, Wubing Qin, Mehdi Sadeghpour, and Sergei Avedisov, for the valuable discussions with them.

Finally, I would like to appreciate my parents for their unconditional love and support. Even though we were away by half of the earth, their care and encouragement made me never feel apart from them. This provided me with confidence and strength to overcome any problems in my research and life.

TABLE OF CONTENTS

LIST OF FIGURES

LIST OF APPENDICES

LIST OF ABBREVIATIONS

ACC Adaptive Cruise Control

ASMC Adaptive Sliding-Mode Control

CACC Cooperative Adaptive Cruise Control

CVN Connected Vehicle Network

CCC Connected Cruise Control

DSRC Dedicated Short-Range Communication

HTTF Head-to-Tail Transfer Function

ITS Intelligent Transportation Systems

LPF Leader-Predecessor-Follower

LTI Linear Time-Invariant

PF Predecessor-Follower

V2V Vehicle-to-Vehicle

ABSTRACT

The emerging wireless Vehicle-to-Vehicle (V2V) communication technologies can be exploited to monitor the motion of distant vehicles, even those beyond the line of sight. Incorporating the data provided by V2V communication into vehicle control systems has great potentials for enhancing vehicle safety, improving traffic mobility, and reducing fuel consumption. In this dissertation, Connected Cruise Control (CCC) is proposed to regulate the longitudinal motion of vehicles by incorporating motion data received from multiple vehicles ahead via V2V communication. CCC allows the incorporation of human-driven vehicles that do not broadcast information. Moreover, it needs neither a designated leader nor a prescribed connectivity topology. Such flexibility makes CCC practical for implementation in real traffic, leading to a Connected Vehicle Network (CVN) that is comprised of CCC vehicles and conventional human-driven vehicles. The design of CCC is challenging since V2V communication leads to complex connectivity topologies and may have significant information delays. Moreover, uncertainties arising from the vehicle dynamics and the varying traffic environment lead to additional complexity for CCC design.

To reduce design complexity, a hierarchical framework is utilized for systematically designing CCC that remains scalable for complex vehicle networks. This framework is comprised of three levels: perception level, planning level, and execution level. At the *perception level*, a causality detector is proposed to determine whether the information received from V2V communication is relevant to the CCC vehicle. Then, we design a link-length estimator to identify the number of vehicles between the broadcasting vehicle and the receiving vehicle. Based on the output of the link length estimator, we also design a

network-dynamics identifier to approximate the nonlinear time-delayed dynamics of vehicle networks, which can be used to predict the motion of the vehicle immediately ahead by using the information received from distant vehicles. At the *planning level*, a general controller is presented to generate the desired longitudinal dynamics by incorporating information delays and connectivity topologies. We derive conditions for choosing control gains which can ensure the asymptotic stability of the equilibrium and can also attenuate perturbations from vehicles ahead. A motif-based approach is proposed for modular design of complex vehicle networks that is scalable when the number of vehicles increases. Simulation results show the advantages of V2V communication in improving traffic dynamics by attenuating disturbances. At the *execution level*, we consider a physics-based vehicle model that includes uncertain vehicle parameters and external disturbances such as aerodynamic drag. An adaptive sliding-mode controller is designed to regulate the engine torque, in order to make the vehicle state track the desired longitudinal dynamics.

CHAPTER 1

Introduction

1.1 Motivation

The ground transportation system plays an important role in modern society. However, the dramatically growing number of vehicles has led to many problems such as vehicle collisions, traffic congestion, and excessive greenhouse gas emissions. Over the past decade in the United States of America, road transportation has been responsible for 30,000 fatalities in road accidents per year, 4.2 billion hours wasted in traffic congestion (equivalent to one full work week per person), and 20 percent of the carbon dioxide produced from tailpipe emissions [1]. The demands for higher level of safety and mobility motivate the development of Intelligent Transportation Systems (ITS) [2, 3].

To reduce driver workload, cruise control was implemented in vehicles to maintain a constant speed by tuning the throttle position. However, cruise control cannot adjust the speed of the vehicle according to the speed of surrounding vehicles, and thus, it cannot be applied in dense traffic where acceleration and deceleration frequently occur. The desire for automatic speed adjustment led to the development of Adaptive Cruise Control (ACC) [4–8], which monitors the motion of the vehicle immediately ahead by using range sensors (e.g., radar, LiDAR) and adjusts the vehicle speed accordingly. Although ACC may improve ride comfort [9], its improvement on the traffic flow dynamics is not significant since the range sensors can only monitor the motion of the vehicles within the line of sight.

The emerging wireless V2V communication technologies enable vehicles to monitor multiple distant vehicles, even those beyond the line of sight. Moreover, compared with range sensors, V2V communication can provide more information such as acceleration. Therefore, incorporating the data received from V2V communication into vehicle control systems has great potentials for increasing mobility [10–12], enhancing vehicle safety [13,14], reducing fuel consumption [15,16], and improving ride comfort. However, V2V

communication leads to complex connectivity topologies and may have significant information delays, which increases the difficulty for control design. Moreover, real traffic may contain vehicles that do not broadcast information, which leads to uncertainties in the traffic environment and results in additional complexity for exploiting V2V communication. In this dissertation, we seek for systematic methods for incorporating V2V communication into vehicle control systems, in order to improve the traffic flow dynamics by alleviating congestion.

1.2 Preliminaries

1.2.1 Dedicated Short-Range Communication

In practice, the wireless V2V communication can be realized via Dedicated Short-Range Communication (DSRC) that is standardized as IEEE 802.11p [17]. DSRC is a peer-to-peer wireless communication that permits high-speed data transmission for communication-based active safety applications. In the United States, the Federal Communications Commission allocated 75 MHz of spectrum in the 5.9 GHz band for use by ITS vehicle safety and mobility applications [18]. DSRC sends basic safety messages (BSMs) every 0.1 second. According to SAE J2735 Message Set Dictionary standard [19], BSMs contain core state information about the broadcasting vehicle, including position, velocity, vehicle size, and system status. The latency and the data rate of DSRC are 200 μs and 6 Mb/s, respectively. The communication range is within 1000 meters [20]. The high reliability of DSRC makes it practical to implement our proposed CCC in practice.

1.2.2 Basic Assumptions

The results of this dissertation are based on several assumptions. First, since this dissertation is focused on the longitudinal control of vehicles, we assume that all vehicles are in the same lane. But we also consider cases where vehicles cut into or cut off the lane. Moreover, we neglect the deteriorating effects of environment (e.g., block of buildings) on the success of V2V communication. To simplify analysis, we assume that the longitudinal dynamics of human-driven vehicles are known and they can be described by using car-following models. In particular, the optimal velocity model [21] will be used in this dissertation. In practice, there are information delays that may be caused by human reaction, digital processing, or intermittency and packet drops in V2V communication. We assume that information delays are constant and known, although their values may vary stochastically in practice.

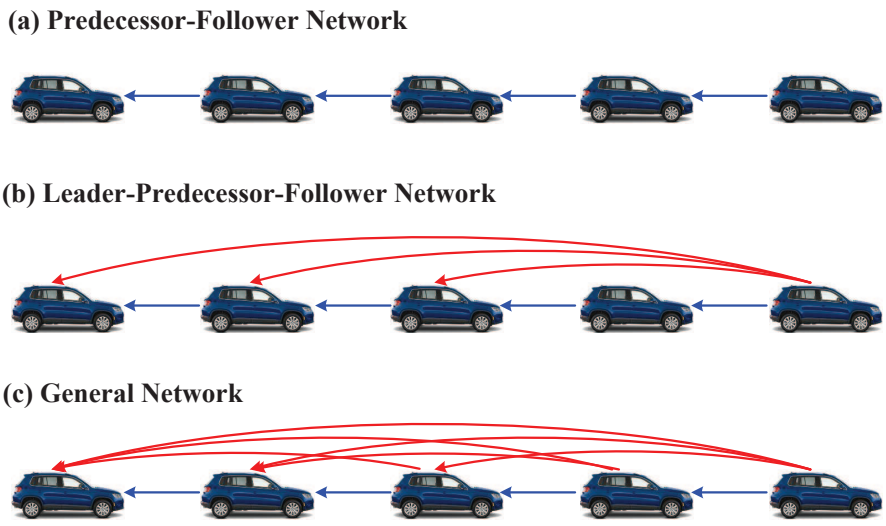

Figure 1.1: Connectivity topologies in connected vehicle networks: (a) predecessor-following network where each vehicle only responds to the vehicle immediately ahead; (b) leader-predecessor-following network where each vehicle responds to the vehicle immediately ahead and also to the designated leader; (c) general network where the communication can be established between any pairs of vehicles.

1.3 Related Work on Connected Vehicle Networks

In conventional traffic, each vehicle only responds to the vehicles within the line of sight, typically just the vehicle immediately ahead. Exploiting V2V communication enables vehicles to get access to the motion information of multiple distant vehicles, even those beyond the line of sight. This leads to complex connectivity topologies of information flow among vehicles, yielding a connected vehicle network (CVN). The amount of research on the design of CVN for improving traffic dynamics has increased rapidly in recent years. One way to classify these results is according to the connectivity topologies built by information flow. There are researchers investigated bi-directional connectivity topology [22, 23], where each vehicle responds to both the motion of vehicles ahead and the motion of vehicles behind. However, in terms of mobility and safety, the motion of vehicles ahead is more important than that of vehicles behind. Thus, we focus on the "forward-looking" scenarios such that each vehicle only responds to the motion of vehicles ahead.

The simplest connectivity topology is the Predecessor-Follower (PF) scenario, where each vehicle only responds to the motion of the vehicle immediately ahead; see Figure 1.1(a). This scenario is indeed the same as the conventional traffic but V2V communication can provide additional information such as acceleration, which cannot be detected by human perception or range sensors. Incorporating the acceleration data of the vehicle

immediately ahead into vehicle control systems for attenuating disturbances in traffic dynamics was investigated in [24–27] while the study [28] also showed that inappropriate use of acceleration information might degrade the ride comfort and even lead to safety hazards. The effects of intermittency and stochastic packet drops of V2V communication on the dynamics of PF vehicle networks were studied in [29]. Taking the possible sensor failures into account, the authors in [30] designed a switched controller to stabilize a vehicle platoon. For heavy-duty vehicle platoons, a decentralized controller was designed in [31] by applying the linear quadratic control framework, while in [32] nonlinear range policies were used to increase the traffic throughput. In [33], the authors investigated the dynamics of nonlinear vehicle networks by using a ring configuration and provided a method for decomposition to simplify the analysis. Impacts of PF vehicle network on road traffic dynamics were also investigated by experimental projects such as California PATH [34, 35].

PF vehicle networks do not take advantage of V2V communication in monitoring the motion of distant vehicles beyond the line of sight. When each vehicle responds to the motion of the vehicle immediately ahead and also responds to the motion of a designated leader via V2V communication, it leads to the Leader-Predecessor-Follower (LPF) network; see Figure 1.1(b). When losing the communication with the leading vehicle, LPF networks degrade to PF networks. The corresponding performance degradation was shown in [36]. Effects of communication delays on the dynamics of LPF vehicle platoons were investigated in [37]. The study in [38] showed the benefits of the LPF connection for improving traffic flow dynamics by attenuating disturbances. It was shown in [39] that disturbance attenuation may be achieved by using the motion data of the vehicle immediately ahead and the velocity data of the platoon leader. The potentials of the LPF vehicle network for reducing fuel consumption and improving safety have also been studied by experimental projects such as SARTRE [40] and the grand cooperative driving challenge (GCDC) [41].

Indeed, neither the PF network nor the LPF network can make full use of V2V communication due to their strong restrictions on the connectivity topologies. In this dissertation, we relax these restrictions and investigate the design of general vehicle networks, which allow communication between any pair of vehicles and require no designated leader; see Figure 1.1(c). The study in [42] showed that connectivity topologies and information delays had significant impacts on the dynamics of vehicle networks. Assuming that a vehicle receives information from all vehicles ahead within the communication range, the research in [43] optimized the control gains by using the linear quadratic regulator (LQR) framework. In [44–46], the effect of nonlinear dynamics on disturbance attenuation along vehicle networks was investigated. Assuming that all vehicles have the same dynamics and neglecting information delays, the authors in [47] investigated the stability and scalability

of vehicle networks.

1.4 Connected Cruise Control

One way to utilize V2V communication in vehicle longitudinal control systems is to construct Cooperative Adaptive Cruise Control (CACC) [48]. This corresponds to an LPF platoon of vehicles such that all vehicles automatically respond to the vehicle immediately ahead using ACC while also monitoring the motion of a designated platoon leader via V2V communication. However, implementing CACC in daily traffic is challenging since it requires that multiple ACC vehicles travel next to each other, which rarely occurs in practice due to the low penetration of such vehicles. Moreover, CACC relies on a designated platoon leader, which may be not available in daily traffic. Furthermore, the LPF connectivity topology of CACC may limit the length of the platoon by the communication range. Relaxing the aforementioned restrictions, we propose the concept of connected cruise control (CCC) [49, 50], which exploits the information received from multiple vehicles ahead via V2V communication. CCC allows the incorporation of vehicles that are not equipped with range sensors or V2V communication devices. Moreover, CCC requires neither a designated platoon leader nor a prescribed connectivity topology. Such flexibility makes it practical to implement CCC in real traffic.

However, the design of CCC is challenging due to the following facts. First, a CCC vehicle may receive information from a large number of vehicles that are not relevant to the motion of the CCC vehicle. Therefore, one needs to determine whether the received information is relevant to the CCC vehicle before incorporating the information into the vehicle controller. Then, to make appropriate use of motion data provided by V2V communication, the CCC vehicle shall be able to identify the dynamics of the vehicle network, which is typically nonlinear and includes time delays. Furthermore, CCC should be designed to allow a large variety of connectivity topologies and remain robust against information delays and uncertain vehicle dynamics.

Figure 1.2(a) shows a vehicle network where the CCC vehicle i at the tail receives motion data from vehicles $j = p, \ldots, i-1$, where vehicle p denotes the furthest broadcasting vehicle within the communication range. The motion of the vehicle immediately ahead can be monitored by human perception, range sensors, or V2V communication, while distant vehicles can only be monitored by using V2V communication since they are beyond the line of sight. Note that CCC allows the incorporation of vehicles that do not broadcast information (e.g., vehicle $i-2$). For simplicity and consistency, in the remaining parts of this dissertation, we use red vehicles for CCC vehicles, blue vehicles for non-CCC vehicles

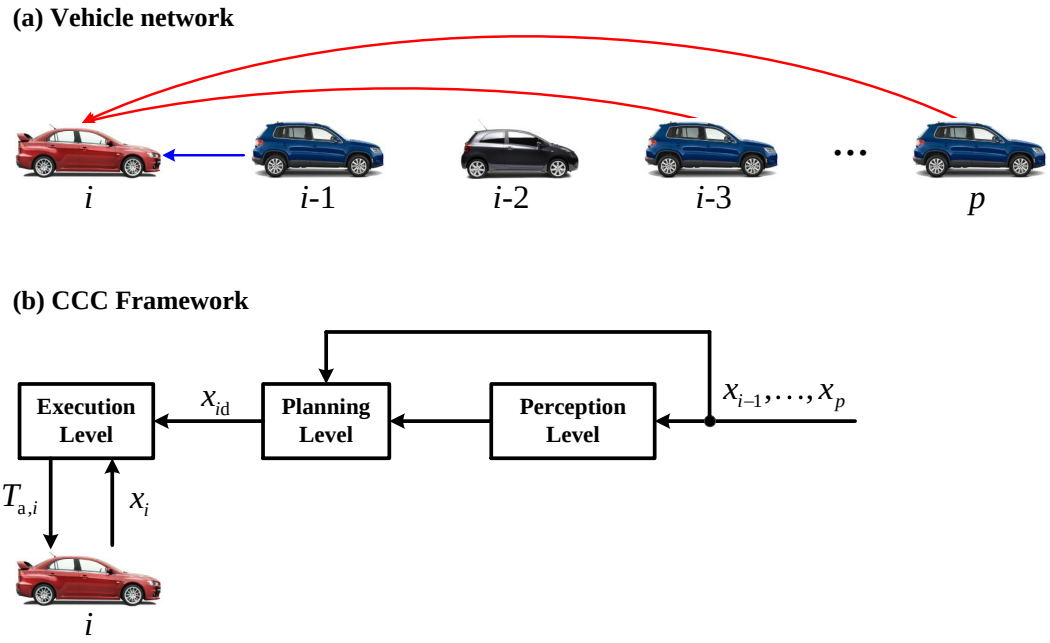

Figure 1.2: (a) A vehicle network where a CCC vehicle (red) at the tail receives information broadcasted by multiple vehicles ahead. Vehicle p denotes the furthest broadcasting vehicle within the communication range of vehicle i. Note that it allows the incorporation of vehicles that do not broadcast information; see the black vehicle $i-2$. (b) A hierarchical framework for CCC design that exploits the motion data x_j received from vehicles $j = p, \ldots, i-1$ via V2V communication.

that broadcast information, and black vehicles for non-CCC vehicles that do not broadcast information; see Figure 1.2(a).

To reduce the complexity for CCC design, we utilize a hierarchical framework in this dissertation, which is comprised of perception level, planning level, and execution level, as displayed in Figure 1.2(b). *Perception level* is designed to enable the CCC vehicle to be aware of the surrounding traffic environment by exploiting the motion data received from vehicles $p, \ldots, i-1$. In particular, this level determines whether the received information is relevant to the motion of the CCC vehicle, and it also identifies the dynamics of the vehicle network for subsequent control design. At the *planning level*, the desired state $x_{i\mathrm{d}}$ for the CCC vehicle i is generated by incorporating the motion data of multiple vehicles ahead and the information provided by the perception level. Note that connectivity topologies and information delays are taken into account at the planning level. *Execution level* controls the axle torque $T_{\mathrm{a},i}$ by determining the engine torque and selecting appropriate gears, in order to regulate the vehicle state x_i to track the desired state $x_{i\mathrm{d}}$ while counteracting the

uncertainties in vehicle dynamics.

1.5 Contributions and Dissertation Outline

To realize the hierarchical CCC design mentioned in Section 1.4, this research has achieved the following contributions.

First, we propose a general controller for the planning level, which includes information delays and allows all possible "forward-looking" connectivity topologies. This controller guarantees the existence of a unique uniform flow equilibrium that is independent of the network size, connectivity topologies, control gains, and information delays. This property is important for ensuring the CCC performance in uncertain traffic scenarios. Then, we investigate the dynamics in the vicinity of the equilibrium by using the linearized model. In particular, we study the impacts of connectivity topologies and information delays on the dynamics of vehicle networks. In order to achieve modular and scalable design of CVNs, we propose a motif-based approach inspired by recent results in systems biology [51]. The key idea is that any complex vehicle networks can be constructed by combining fundamental motifs (simple networks that contain one CCC vehicle at the tail). Thus, by analyzing the dynamics of individual motifs and characterizing the effects of motif combinations, one can modularly construct vehicle networks that are robust against information delays and remain scalable for a large number of vehicles. Moreover, a systematic method is derived to calculate head-to-tail transfer functions of complex networks in an efficient way, which is crucial for characterizing stability and disturbance attenuation of CVNs. The corresponding results are presented in Chapter 2 [42, 49, 52].

Considering that the results obtained from linearized dynamics may only be valid when the state is in the vicinity of the equilibrium, we further investigate the nonlinear time-delayed dynamics of CVNs by applying the Lyapunov-Krasovskii approach. We derive conditions for stability and disturbance attenuation, which are simple and thus can be applied for large vehicle networks. Particularly, we present a condition that ensures disturbance attenuation for nonlinear time-delayed networks but only requires the analysis of the linearized dynamics. Numerical simulation are used to show that the nonlinear analysis lead to results that are more accurate than those given by linear analysis. The corresponding results are presented in Chapter 3 [44–46, 53].

The planning level is designed to generate desired CCC dynamics based on a simplified vehicle model, where the physical effects such as aerodynamic drag and rolling resistance are not taken into account. However, in practice these effects significantly affect the vehicle dynamics. To ensure that the vehicle state tracks the desired dynamics, at the execution

level we consider a physics-based vehicle model and design a control scheme for regulating the engine torque. In particular, an adaptive sliding-mode controller is designed to guarantee the tracking performance in the presence of uncertainties in parameters and external disturbances. The corresponding results are provided in Chapter 4 [54, 55].

Note that information may be broadcasted by a vehicle that is not relevant for the CCC vehicle. Moreover, the dynamics of the vehicle network may not be known, especially when there exist vehicles that do not broadcast information. Therefore, to realize CCC in real traffic, at the perception level we determine whether the received information is relevant for the CCC vehicle and we also identify the dynamics of the vehicle network. In particular, we first propose a causality detector which determines the relevance by evaluating the causality between the motion of the broadcasting vehicle and the vehicle immediately ahead of the CCC vehicle. Then, we design an estimator to identify the number of non-broadcasting vehicles between the broadcasting vehicle and the CCC vehicle, which plays an important role for identifying the dynamics of the vehicle network. Finally, we use a linear discrete-time model to approximate the nonlinear time-delayed dynamics of vehicle networks, where the coefficients of the model are obtained by solving an optimization problem with constraints for stability of the model. We propose an algorithm to solve the stability-constrained optimization problem in an efficient way. The corresponding details are presented in Chapter 5 [56, 57].

In Chapter 6, we conclude our results about the hierarchical framework for CCC design and discuss future research directions.

CHAPTER 2

Planning Level: Motif-Based Design of Connected Vehicle Networks

In this chapter, we focus on the planning level and design the car-following dynamics by incorporating the motion data received from multiple vehicles ahead, in order to generate the desired state for the CCC vehicle i

$$x_{i\mathrm{d}}(t) = \begin{bmatrix} s_{i\mathrm{d}}(t) \\ v_{i\mathrm{d}}(t) \end{bmatrix}, \tag{2.1}$$

see Figure 1.2, where the symbols s and v represent the position and the velocity, respectively. Here, we consider the vehicle longitudinal kinematics, which can be described by a second-order integrator

$$\dot{x}_{i\mathrm{d}}(t) = \begin{bmatrix} 0 & 1 \\ 0 & 0 \end{bmatrix} x_{i\mathrm{d}}(t) + \begin{bmatrix} 0 \\ 1 \end{bmatrix} u_{i\mathrm{d}}(t)\,. \tag{2.2}$$

Such a model can be obtained by neglecting the effects of aerodynamic drag and rolling resistance in the physics-based model [58]. Then, we design the acceleration input $u_{i\mathrm{d}}$ for the desired CCC dynamics by exploiting the motion data of multiple vehicles ahead received via V2V communication. As will be explained later, one needs to design $u_{i\mathrm{d}}$ for plant stability, head-to-tail string stability, and eventual string stability of the uniform flow equilibrium, in order to guarantee safety and mobility.

Definition 1 A vehicle network is in uniform flow equilibrium if all vehicles move at the identical constant speed v^* while maintaining the same distance h^* from the vehicle immediately ahead, i.e.,

$$x_j^*(t) = \begin{bmatrix} s_j^*(t) \\ v_j^*(t) \end{bmatrix} = \begin{bmatrix} v^* t + \overline{s}_j \\ v^* \end{bmatrix}, \tag{2.3}$$

for all j-s, where the constant $\overline{s}_j$ satisfies $\overline{s}_{j-1} - l_{j-1} - \overline{s}_j = h^*$ with l_{j-1} denoting the length of vehicle $j-1$; see [42, 46].

Definition 2 Plant stability means that, if all vehicles $j = 0, \ldots, i-1$ have reached the uniform flow equilibrium (2.3), then vehicle i can asymptotically approach the uniform flow equilibrium (2.3), i.e.,

$$x_i(t) \to x_i^*(t)\,, \quad \text{as } t \to \infty\,. \tag{2.4}$$

In practice, disturbances may arise from some vehicles and propagate backward along the vehicle chain. This may degrade the traffic flow performance and may even cause traffic congestion if the disturbances are amplified when propagating along the vehicle chain [59]. We define the perturbation about the equilibrium (2.3) as

$$\tilde{x}_j(t) = \begin{bmatrix} \tilde{s}_j(t) \\ \tilde{v}_j(t) \end{bmatrix} = x_j(t) - x_j^*(t)\,, \tag{2.5}$$

for all j-s. Then, we evaluate the disturbance attenuation along the vehicle network by using the concepts of head-to-tail string stability and eventual string stability.

Definition 3 Consider an $(n+1)$-vehicle network where the head and the tail vehicles are indexed by 0 and n, respectively. This vehicle network is said to be head-to-tail string stable in $\mathcal{L}_p$ norm ($\mathcal{L}_p$-HT string stable) if and only if

$$\|\tilde{v}_n^{(\mathrm{s})}\|_{\mathcal{L}_p} < \|\tilde{v}_0^{(\mathrm{s})}\|_{\mathcal{L}_p}\,, \tag{2.6}$$

where the superscript "(s)" is used to represent the steady state and $p = 1, 2, \ldots$; see [46].

Here, we consider the steady-state perturbation to make the results independent of initial conditions. Note that the condition (2.6) depends on the choice of norms, and thus one may obtain different conclusions about the head-to-tail string stability for the same network by using different norms. Moreover, the condition (2.6) is defined for a network of given size, and thus, it may not ensure that disturbances tend to be eliminated when the network scales up with repeated connectivity patterns. To address these two issues, we construct an infinitely long vehicle network by cascading the original network such that the tail vehicle of a block becomes the lead vehicle of another block. In such cascading networks, the tail vehicle of the k-th block is indexed by kn. For the cascading vehicle networks, head-to-tail string stability (2.6) may not ensure $\|\tilde{v}_{kn}^{(\mathrm{s})}\|_{\mathcal{L}_p} < \|\tilde{v}_{(k-1)n}^{(\mathrm{s})}\|_{\mathcal{L}_p}$ for all k-s when the dynamics is nonlinear.

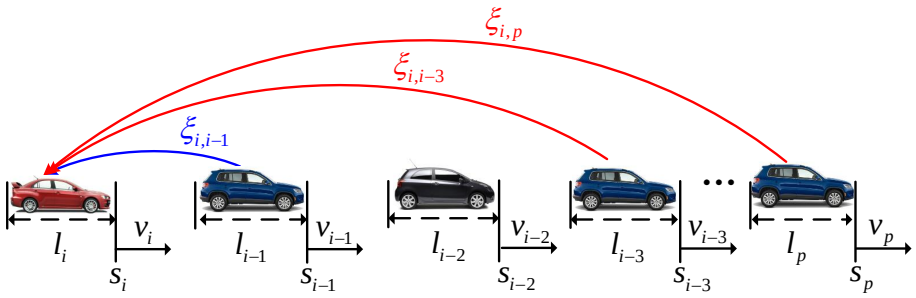

Figure 2.1: A CCC vehicle (red) monitors the motion of multiple vehicles ahead.The short-range link (blue) can be realized by a human driver, range sensors (e.g., radar and LiDAR), and V2V communication, while the long-range links (red) can only be realized by using V2V communication. Symbols s_j, l_j, v_j denote the position, length, and velocity of vehicle j, respectively. The information delays between vehicles i and j are denoted by $\xi_{i,j}$ for $j = p, \ldots, i-1$.

Definition 4 A vehicle network is said to be eventually string stable if and only if the perturbations are eliminated in the corresponding cascade, that is,

$$\tilde{x}_{kn}(t) \to 0\,, \quad \text{as } t \to \infty\,,\ k \to \infty\,, \tag{2.7}$$

see [46].

Different from the conventional definition of string stability [60, 61] that requires the disturbance to be attenuated by each vehicle, Definitions 3 and 4 allow disturbances to be amplified by some vehicles in the network. Such flexibility is useful for vehicle networks that contain human-driven vehicles, for which the dynamics cannot be designed. Indeed, Definitions 3 and 4 are independent of each other and describe the disturbance attenuation in a vehicle network from different aspects. The head-to-tail string stability evaluates whether the disturbance arising from the head vehicle can be attenuated when reaching the tail vehicle in a given network, while the eventual string stability evaluates whether the disturbance can be eliminated in an infinitely long vehicle chain with cascading patterns.

In practice, plant stability is a fundamental requirement for vehicle safety, while head-to-tail string stability and eventual string stability are used for congestion mitigation.

Figure 2.1 shows a vehicle network where the CCC vehicle i monitors the position s_j and the velocity v_j of vehicles $j = p, \ldots, i-1$ with vehicle p denoting the furthest broadcasting vehicle within the communication range. We assume that the position s_j is measured at the front bumper of vehicle j. Here, the symbol l_j denotes the length of vehicle j while the symbol $\xi_{i,j}$ represents the information delay between vehicles j and i, which may be human reaction time, sensing delay, or communication delay. Note that communication

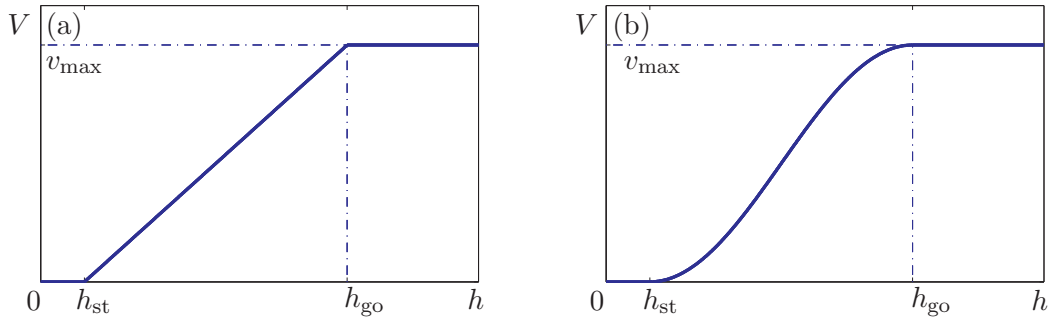

Figure 2.2: Range policy functions defined by (2.9). Panels (a) and (b) correspond to formulae (2.10) and (2.11), respectively.

delays are caused by intermittency and packet drops in V2V communication [62].

For human-driven vehicle k, we assume that its car-following dynamics can be described by the optimal velocity model [21], that is,

$$\begin{aligned} \dot{s}_k(t) &= v_k(t)\,, \\ \dot{v}_k(t) &= \alpha_{k,k-1}\big(V\big(h_{k,k-1}(t-\xi_{k,k-1})\big) - v_k(t-\xi_{k,k-1})\big) \\ &\quad + \beta_{k,k-1}\big(v_{k-1}(t-\xi_{k,k-1}) - v_k(t-\xi_{k,k-1})\big)\,, \end{aligned} \tag{2.8}$$

where $\alpha_{k,k-1}$ and $\beta_{k,k-1}$ denote the control gains for inter-vehicle distance and relative velocity, respectively. The range policy $V(h)$ yields the desired velocity as a function of the distance h. Based on behaviors of human drivers [59], we assume the range policy in the form

$$V(h) = \begin{cases} 0\,, & \text{if} \quad h \le h_{\rm st}\,, \\ F(h)\,, & \text{if} \quad h_{\rm st} < h < h_{\rm go}\,, \\ v_{\max}\,, & \text{if} \quad h \ge h_{\rm go}\,, \end{cases} \tag{2.9}$$

where $h_{\rm st}$, $h_{\rm go}$, and $v_{\max}$ are positive constants. This means that the vehicle tends to stop for small distances $h \le h_{\rm st}$ while aiming to maintain the preset maximum speed $v_{\max}$ for large distances $h \ge h_{\rm go}$. In the middle range $h_{\rm st} < h < h_{\rm go}$, the desired velocity is determined by the function $F(h)$. Typically, the function $F(h)$ is an increasing function so that the range policy $V(h)$ is continuous. The two possible choices

$$F(h) = v_{\max}\frac{h - h_{\rm st}}{h_{\rm go} - h_{\rm st}}\,, \tag{2.10}$$

$$F(h) = \frac{v_{\max}}{2}\left[1 - \cos\left(\frac{\pi(h - h_{\rm st})}{h_{\rm go} - h_{\rm st}}\right)\right] \tag{2.11}$$

are shown in Figure 2.2(a,b), respectively. The linear function (2.10) makes $V(h)$ non-smooth at $h = h_{\rm st}$ and $h = h_{\rm go}$, which leads to discontinuities in the jerk that may degrade the ride comfort. Thus, we use the nonlinear function (2.11) that results in smooth derivatives of $V(h)$ at $h = h_{\rm st}$ and $h = h_{\rm go}$. In the remainder of this dissertation, we will use the nonlinear function (2.11) in the range policy function (2.9).

To mimic the human driving behavior and also incorporate the information received from multiple vehicles ahead, for the CCC vehicle i with dynamics (2.2), we generalize (2.8) by incorporating "forward-looking" connectivity topologies, that is,

$$u_{i\rm d}(t) = \sum_{j=p}^{i-1} \Big[\alpha_{i,j}\big(V\big(h_{i{\rm d},j}(t-\xi_{i,j})\big) - v_{i\rm d}(t-\xi_{i,j})\big) + \beta_{i,j}\big(v_j(t-\xi_{i,j}) - v_{i\rm d}(t-\xi_{i,j})\big)\Big] , \quad (2.12)$$

where the the constants

$$\alpha_{i,j} = \gamma_{i,j}\overline{\alpha}_{i,j} , \quad \beta_{i,j} = \gamma_{i,j}\overline{\beta}_{i,j} \quad (2.13)$$

denote the effective control gains along the link from vehicle j to vehicle i. Here, $\overline{\alpha}_{i,j}, \overline{\beta}_{i,j}$ are the actual control gains, and $\gamma_{i,j}$ is determined by the connectivity topology such that

$$\gamma_{i,j} = \begin{cases} 1 , & \text{if vehicle } i \text{ uses the data of vehicle } j , \\ 0 , & \text{otherwise} . \end{cases} \quad (2.14)$$

Note that the vehicle immediately ahead is always monitored for safety reasons such that $\gamma_{i,i-1} = 1$ always holds. We emphasize that the CCC vehicle can choose not to use the information received from certain distant vehicles.

In (2.12), the quantity

$$h_{i{\rm d},j} = \frac{1}{i-j}\left(s_j - s_{i\rm d} - \sum_{k=j}^{i-1} l_k\right) \quad (2.15)$$

denotes the average distance between vehicles i and j. Such averaging is used to make the distance comparable for different j-s and also make the uniform flow equilibrium independent of the network size.

Theorem 1 If the control gains $\overline{\alpha}_{i,j}$ in (2.13) are positive for $j = i-1, \ldots, p$, the controller (2.12) guarantees the existence of a unique uniform flow equilibrium (2.3) that is independent of the network size, connectivity topologies, control gains, and information delays. Moreover, the equilibrium satisfies the range policy (2.9), that is,

$$v^* = V(h^*) . \quad (2.16)$$

The proof is presented in Appendix A.1. The uniqueness and the independence of the uniform flow equilibrium are crucial for ensuring the performance of vehicle networks in uncertain traffic environment. To simplify notations, here we assume that the vehicle state x_i precisely tracks the desired state $x_{i\mathrm{d}}$ and hence will not spell out the subscript "d" in the rest of this chapter. Then, combining the model (2.2) and the controller (2.12) leads to the car-following dynamics

$$\begin{aligned}
&\dot{s}_i(t) = v_i(t)\,,\\
&\dot{v}_i(t) = \sum_{j=p}^{i-1} \Big[\alpha_{i,j}\big(V\big(h_{i,j}(t-\xi_{i,j})\big) - v_i(t-\xi_{i,j})\big) + \beta_{i,j}\big(v_j(t-\xi_{i,j}) - v_i(t-\xi_{i,j})\big)\Big]\,.
\end{aligned} \tag{2.17}$$

In this chapter, we investigate the dynamics of vehicle networks in the vicinity of the uniform flow equilibrium by using the linearized model. Linearizing (2.17) about the equilibrium at (2.3) and (2.16) yields a Linear Time-Invariant (LTI) system

$$\begin{aligned}
&\dot{\tilde{x}}_i(t) = A_{i,0}\,\tilde{x}_i(t) + \sum_{j=p}^{i-1}\Big(A_{i,j}\,\tilde{x}_i(t-\xi_{i,j}) + B_{i,j}\,\tilde{x}_j(t-\xi_{i,j})\Big)\,,\\
&\tilde{v}_i(t) = C\tilde{x}_i(t)\,,
\end{aligned} \tag{2.18}$$

where $\tilde{x}_j$ is given in (2.5) and other matrices are given by

$$\begin{aligned}
&A_{i,0} = \begin{bmatrix} 0 & 1 \\ 0 & 0 \end{bmatrix}\,, \qquad A_{i,j} = \begin{bmatrix} 0 & 0 \\ -\varphi_{i,j} & -\kappa_{i,j} \end{bmatrix}\,,\\
&B_{i,j} = \begin{bmatrix} 0 & 0 \\ \varphi_{i,j} & \beta_{i,j} \end{bmatrix}\,, \quad C = \begin{bmatrix} 0 & 1 \end{bmatrix}\,,
\end{aligned} \tag{2.19}$$

with

$$\varphi_{i,j} = \frac{\alpha_{i,j}V'(h^*)}{i-j}\,, \quad \kappa_{i,j} = \alpha_{i,j} + \beta_{i,j}\,, \quad i > j\,. \tag{2.20}$$

Here, $V'(h)$ represents the derivative of $V(h)$ with respect to h, i.e., $V'(h) = \mathrm{d}V(h)\big/\mathrm{d}h$. In the remainder of this chapter, we will use the model (2.18)–(2.20) to investigate the design of control gains $\alpha_{i,j}$ and $\beta_{i,j}$ for plant stability, head-to-tail string stability, and eventual string stability of vehicle networks.

2.1 Calculation of Head-to-Tail Transfer Function

The stability of the LTI system (2.18) can be evaluated by using the Head-to-Tail Transfer Function (HTTF), which represents the dynamic relationship between the motion of the head vehicle and the tail vehicle in the Laplace domain. Here, we provide a systematic method to calculate HTTFs in an efficient way. Assuming zero initial condition, we obtain the Laplace transform of (2.18)

$$\tilde{V}_i(s) = \sum_{j=p}^{i-1} T_{i,j}(s)\tilde{V}_j(s)\,, \tag{2.21}$$

where $\tilde{V}_i(s)$ denotes the Laplace transform of $\tilde{v}_i(t)$ and

$$T_{i,j}(s) = \mathrm{e}^{-s\xi_{i,j}} C\left(sI_2 - A_{i,0} - \sum_{j=p}^{i-1} \mathrm{e}^{-s\xi_{i,j}} A_{i,j}\right)^{-1} B_{i,j} E(s) \tag{2.22}$$

is called the *link transfer function* that acts as a dynamic weight along the link between vehicles i and j; see the weighted graph Figure 2.3. Here, I_2 denotes the 2-dimensional identity matrix and $E(s) = [s^{-1}\,, 1]^{\mathrm{T}}$ links the state and the velocity such that $\tilde{X}_j(s) = E(s)\tilde{V}_j(s)$. Substituting (2.19) into (2.22) yields

$$T_{i,j}(s) = \frac{(s\beta_{i,j} + \varphi_{i,j})\mathrm{e}^{-s\xi_{i,j}}}{s^2 + \sum_{k=p}^{i-1}(s\kappa_{i,k} + \varphi_{i,k})\mathrm{e}^{-s\xi_{i,k}}}\,, \tag{2.23}$$

where $\varphi_{i,j}$ and $\kappa_{i,j}$ are given by (2.20).

The dynamic relationship between vehicles i and m can be represented by the transfer function $G_{i,m}(s)$ such that

$$\tilde{V}_i(s) = G_{i,m}(s)\tilde{V}_m(s)\,. \tag{2.24}$$

Note that the transfer function $G_{i,m}(s)$ includes the dynamics of all vehicles between vehicle m and vehicle i, and it can be obtained by using the relationship (2.21). To evaluate the performance of a vehicle network, we use the HTTF $G_{n,0}(s)$ that evaluates how the perturbation arising from the head vehicle 0 affects the motion of the tail vehicle n. Based on the signal-propagation principle, $G_{n,0}(s)$ can be calculated by summing up the products of link transfer functions along the paths connecting the vehicles n and 0. However, finding these paths manually is difficult for complex networks. To address this problem systematically, one may use a graph theoretical approach [63]. Using the link transfer functions $T_{i,j}(s)$ in (2.23), we define the dynamic coupling matrix $T(s) = [T_{i,j}(s)]$ where $i, j = 0, \ldots, n$.

Without loops, the longest path of an $(n+1)$-vehicle network is of length n. Then, considering $T(s)$ as the adjacency matrix of a weighted graph, the transfer function matrix $G(s) = [G_{i,j}(s)] \in \mathbb{C}^{(n+1)\times(n+1)}$, where $i, j = 0, \ldots, n$, can be calculated by

$$G(s) = \sum_{k=1}^{n} \big(T(s)\big)^k . \tag{2.25}$$

However, for analyzing plant stability and string stability, only the HTTF $G_{n,0}(s)$ is needed. To directly calculate $G_{n,0}(s)$, we propose an efficient approach by defining the modified coupling matrix

$$\widehat{T}(s) = R\big(T(s) + I_{n+1}\big)R^{\mathrm{T}} , \tag{2.26}$$

where $R = [0_{n\times 1}\,, I_n]$ and I_n denotes the n-dimensional identity matrix while $0_{n\times 1}$ is an n-by-1 zero vector. Indeed, $\widehat{T}(s) \in \mathbb{C}^{n\times n}$ can be obtained by deleting the first row and last column of the matrix $T(s) + I_{n+1}$.

Theorem 2 The HTTF $G_{n,0}(s)$ is given by the permanent of the modified coupling matrix (2.26), that is,

$$G_{n,0}(s) = \mathrm{perm}\Big(\widehat{T}(s)\Big) \triangleq \sum_{\sigma_i \in S_n} \prod_{i=1}^{n} \widehat{T}_{i,\sigma_i}(s) = \frac{N(s)}{D(s)} , \tag{2.27}$$

where the sum is computed over all permutations of the set $S_n = \{1, 2, \ldots, n\}$.

Note that the calculation of permanent in (2.27) is similar with the formula for determinant but without the change of signs. The proof of Theorem 2 is given as follows. For an $(n+1)$-vehicle network, the paths from vehicle i to vehicle n can be divided into two groups. One group contains vehicle $(i+1)$, yielding the transfer function $G_{n,i+1}(s)T_{i+1,i}(s)$. The other group does not contain vehicle $(i+1)$ but includes the long links connecting vehicles i and n, leading to the transfer function $\overline{G}_{n,i}(s)$. That is, we have $G_{n,i}(s) = G_{n,i+1}(s)T_{i+1,i}(s) + \overline{G}_{n,i}(s)$. Applying this formula recursively from $i = 0$ to $i = n-2$ leads to (2.27), which completes the proof.

To demonstrate the applications of (2.25) and (2.27), we consider the (4+1)-vehicle network in Figure 2.3 as an example and calculate the corresponding HTTF. The coupling

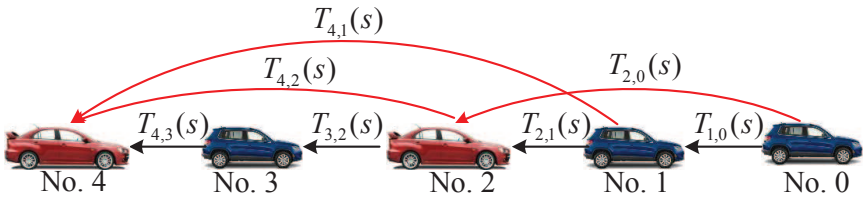

Figure 2.3: Example of a (4+1)-vehicle network: link transfer functions act as dynamic weights along the links.

matrix of this network is given by

$$T(s) = \begin{bmatrix} 0 & 0 & 0 & 0 & 0 \\ T_{1,0}(s) & 0 & 0 & 0 & 0 \\ T_{2,0}(s) & T_{2,1}(s) & 0 & 0 & 0 \\ 0 & 0 & T_{3,2}(s) & 0 & 0 \\ 0 & T_{4,1}(s) & T_{4,2}(s) & T_{4,3}(s) & 0 \end{bmatrix}. \tag{2.28}$$

Applying (2.25) yields the HTTF

$$G_{4,0}(s) = T_{4,1}(s)T_{1,0}(s) + \big(T_{4,2}(s) + T_{4,3}(s)T_{3,2}(s)\big)\big(T_{2,0}(s) + T_{2,1}(s)T_{1,0}(s)\big)\,, \tag{2.29}$$

which can be also obtained by applying the formula (2.27) with the modified coupling matrix

$$\widehat{T}(s) = \begin{bmatrix} T_{1,0}(s) & 1 & 0 & 0 \\ T_{2,0}(s) & T_{2,1}(s) & 1 & 0 \\ 0 & 0 & T_{3,2}(s) & 1 \\ 0 & T_{4,1}(s) & T_{4,2}(s) & T_{4,3}(s) \end{bmatrix}. \tag{2.30}$$

2.2 Stability Conditions

In this section, we present conditions for plant stability, head-to-tail string stability, and eventual string stability by using the HTTF (2.27). Note that the information delays $\xi_{i,j}$ lead to infinitely many characteristic roots $\lambda_i \in \mathbb{C}$ $(i = 1, 2 \ldots)$ that satisfy the characteristic equation $D(\lambda_i) = 0$.

Theorem 3 A connected vehicle network with dynamics given by (2.18) is plant stable if and only if the real parts of all characteristic roots are strictly negative, i.e.,

$$\mathrm{Re}(\lambda_i) < 0\,, \quad i = 1, 2, \ldots, \infty\,. \tag{2.31}$$

The proof of this theorem can be referred to [64]. Indeed, when there are no external disturbances, negative real parts of characteristic roots indicate the decaying of the initial perturbations, which leads to plant stability. Note that there are infinitely many characteristic roots for the system (2.18) due to the information delays.

For plant stable vehicle networks with dynamics (2.18), the $\mathcal{H}_\infty$ norm of the HTTF $G_{n,0}(s)$ is equal to the amplification ratio between the output $\tilde{v}_n(t)$ and the input $\tilde{v}_0(t)$ in $\mathcal{L}_2$ norm [65], that is,

$$\|G_{n,0}\|_{\mathcal{H}_\infty} \triangleq \sup_{\omega>0} \left|G_{n,0}(\mathrm{j}\omega)\right| = \frac{\|\tilde{v}_n\|_{\mathcal{L}_2}}{\|\tilde{v}_0\|_{\mathcal{L}_2}}\,, \tag{2.32}$$

where $\mathrm{j}^2 = -1$.

Theorem 4 A connected vehicle network with dynamics given by (2.18) is $\mathcal{L}_2$-HT string stable if and only if

$$\sup_{\omega>0} |G_{n,0}(\mathrm{j}\omega)| < 1\,. \tag{2.33}$$

This theorem can be proved by combining Definition 3 and (2.32). We remark that, for LTI systems in presence of sinusoidal disturbances, $\mathcal{L}_2$-HT string stability is equivalent to $\mathcal{L}_\infty$-HT string stability due to the following two facts. On the one hand, for LTI systems, sinusoidal input leads to sinusoidal output with the same frequency. On the other hand, for sinusoidal signals, both $\mathcal{L}_2$ and $\mathcal{L}_\infty$ norms are given by the magnitude of the signal.

Theorem 5 A connected vehicle network with dynamics given by (2.18) is eventual string stable if and only if it is $\mathcal{L}_2$-HT string stable.

The proof of Theorem 5 is given as follows. When the given vehicle network (2.18) is $\mathcal{L}_2$-HT string stable, it follows that $\|\tilde{v}_{kn}\|_{\mathcal{L}_2} < \|\tilde{v}_{(k-1)n}\|_{\mathcal{L}_2}$ for $k = 1, 2, \ldots$ in the cascading network. Since $\|\tilde{v}_{kn}\|_{\mathcal{L}_2}$ is lower bounded by zero, we have $\lim_{k\to\infty} \|\tilde{v}_{kn}\|_{\mathcal{L}_2} = 0$, which implies that $\tilde{v}_{kn} \to 0$ as $k \to \infty$. At the limit $\lim_{k\to\infty} \tilde{v}_{kn}(t) \equiv 0$, there are no persistent disturbances to vehicles $\ell > kn$, then $\tilde{s}_\ell(t) \to 0$ as $t \to \infty$ due to plant stability. This implies that $\mathcal{L}_2$-HT string stability leads to eventual string stability in LTI systems. On the other hand, if the network is $\mathcal{L}_2$-HT string unstable, it follows that $\|\tilde{v}_{kn}\|_{\mathcal{L}_2} \geq \|\tilde{v}_{(k-1)n}\|_{\mathcal{L}_2}$ for $k = 1, 2, \ldots$ in the cascading network. Since the perturbations are amplified along the network, they cannot approach zero when the network size increases so that the eventual string stability cannot be achieved as well. This indicates that $\mathcal{L}_2$-HT string stability is also a necessary condition for eventual string stability.

Considering Theorem 5, we only need to investigate plant stability and $\mathcal{L}_2$-HT string stability of CVNs with dynamics (2.18). To obtain analytical conditions for designing

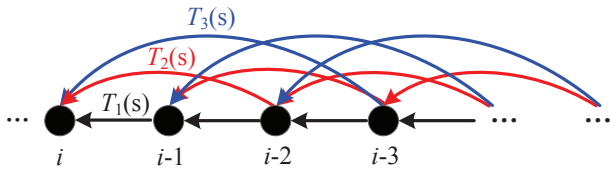

Figure 2.4: A network with a repetitive connectivity patterns, where each node responds to the nearest three nodes ahead.

control gains to ensure plant stability and string stability, one may apply approximations and inequalities to Theorems 3 and 4, but such results are typically quite conservative. To obtain exact (necessary & sufficient) stability conditions, we use the D-subdivision method [66] and solve for stability boundaries. The plant stability boundaries correspond to purely imaginary characteristic roots $\pm \mathrm{j}\Omega$ ($\Omega \geq 0$) that satisfy $D(\pm \mathrm{j}\Omega) = 0$. This is equivalent to

$$\mathrm{Re}\big(D(\mathrm{j}\Omega)\big) = 0\,, \quad \mathrm{Im}\big(D(\mathrm{j}\Omega)\big) = 0\,. \tag{2.34}$$

Solving these two equations for $\alpha_n(\Omega)$ and $\beta_n(\Omega)$ with $\Omega > 0$ leads to plant stability boundaries in the (β_n, α_n)-plane. For $\Omega = 0$, the condition (2.34) can be reduced to

$$D(0) = 0\,, \tag{2.35}$$

which yields additional plant stability boundaries in the (β_n, α_n)-plane.

At the $\mathcal{L}_2$-HT string stability boundaries, we have $\max_\omega |G_{n,0}(\mathrm{j}\omega)| = 1$, which is equivalent to

$$|G_{n,0}(\mathrm{j}\omega_{\mathrm{cr}})| = 1\,, \;\; |G_{n,0}(\mathrm{j}\omega_{\mathrm{cr}})|' = 0\,, \;\; |G_{n,0}(\mathrm{j}\omega_{\mathrm{cr}})|'' < 0\,, \tag{2.36}$$

where the prime denotes the partial derivative with respect to ω, while ω_{cr} is the critical frequency where the maximum occurs. Solving (2.36) for $\alpha_n(\omega_{\mathrm{cr}})$ and $\beta_n(\omega_{\mathrm{cr}})$ gives the $\mathcal{L}_2$-HT string stability boundaries in the (β_n, α_n)-plane. For the vehicle networks (2.18)–(2.20), $|G_{n,0}(0)| = 1$ and $|G_{n,0}(0)|' = 0$ always hold. Thus, $\mathcal{L}_2$-HT string stability boundaries for $\omega_{\mathrm{cr}} = 0$ can be obtained by solving

$$|G_{n,0}(0)|'' = 0\,. \tag{2.37}$$

Then, in order to find feasible regions for designing control gains, one can construct stability diagrams by combining the boundaries (2.34)–(2.37).

The $\mathcal{L}_2$-HT string stability condition (2.33) requires the calculation of HTTF which is challenging for large networks. This motivates us to investigate stability conditions that are

scalable when network size increases. Indeed, such conditions may not exist for general networks. Here, we focus on a class of networks with repetitive connectivity patterns where each node exploits the information received from the nearest ℓ nodes ahead; see Figure 2.4 for $\ell = 3$. Such networks can be realized by using a chain of identical CCC vehicles. In this case, the link transfer function of the same length are equal, i.e., $T_{i,j}(s) = T_{i-j}(s)$. Substituting this into (2.21) yields

$$\tilde{V}_i(s) = \sum_{k=1}^{\ell} T_k(s)\tilde{V}_{i-k}(s)\,, \quad i \geq \ell\,, \tag{2.38}$$

where $T_k(s)$ is the link transfer function for links of length k. Note that (2.24) implies that $\tilde{V}_{i-k}(s) = G_{i-k,0}(s)\tilde{V}_0(s)$. Combining this with (2.38) yields the recursive formula

$$G_{i,0}(s) = \sum_{k=1}^{\ell} T_k(s)G_{i-k,0}(s)\,, \quad i \geq \ell\,, \tag{2.39}$$

which can be rewritten into the matrix form

$$\hat{G}_i(s) = \hat{P}(s)\hat{G}_{i-1}(s)\,, \tag{2.40}$$

where

$$\hat{G}_i(s) = \begin{bmatrix} G_{i,0}(s) \\ G_{i-1,0}(s) \\ G_{i-2,0}(s) \\ \vdots \\ G_{i-\ell,0}(s) \end{bmatrix}\,, \quad \hat{P}(s) = \begin{bmatrix} T_1(s) & T_2(s) & \dots & T_{\ell-1}(s) & T_\ell(s) \\ 1 & 0 & \dots & 0 & 0 \\ 0 & 1 & \dots & 0 & 0 \\ \vdots & \vdots & \ddots & \vdots & \vdots \\ 0 & 0 & \dots & 1 & 0 \end{bmatrix}\,. \tag{2.41}$$

For networks with repetitive connectivity patterns (2.38)–(2.41), we provide a condition that guarantees disturbance attenuation as the network scales up.

Theorem 6 For networks with repetitive connectivity patterns (2.38), as the network size increases to infinity, the disturbance on the tail approaches zero if and only if

$$\sup_{\omega>0} \left|\lambda_k\big(\hat{P}(\mathrm{j}\omega)\big)\right| < 1\,, \quad k = 1, \dots, \ell\,, \tag{2.42}$$

where $\lambda_k(\hat{P}(\mathrm{j}\omega))$ denotes the k-th eigenvalue of $\hat{P}(\mathrm{j}\omega)$ in (2.41).

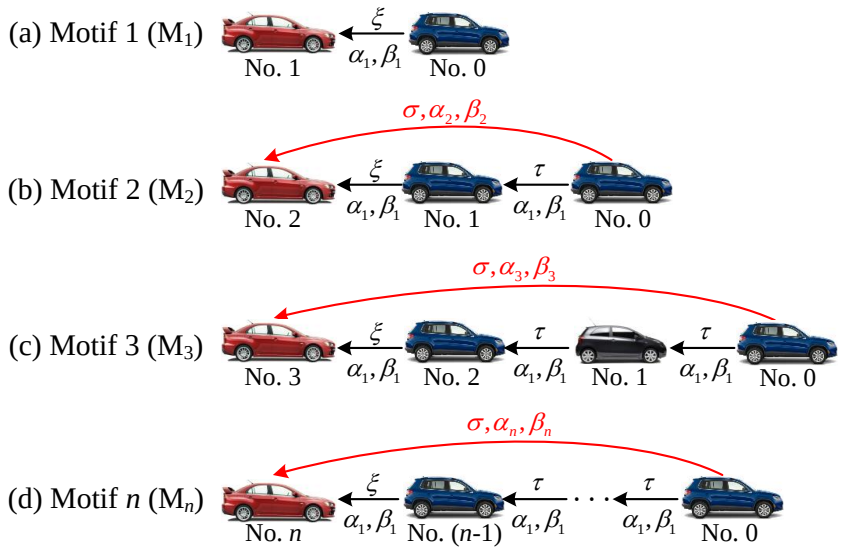

Figure 2.5: Network motifs 1, 2, 3, and n. Symbols τ, σ, ξ denote information delays while α_k, β_k are control gains along the link of length k for $k = 1, 2, \ldots$.

The proof of Theorem 6 is presented as follows. The model (2.40) can be considered as a discrete system in terms of the vehicle index i. Based on the linear discrete system theory [67], we have that $\lim_{i\to\infty} \|\hat{G}_i(\mathrm{j}\omega)\| = 0$ for $\forall \omega > 0$ if and only if the condition (2.42) holds. This completes the proof for Theorem 6. Note that condition (2.42) only utilizes link transfer functions without calculating the HTTF. This reduces the complexity of analysis and design for large networks.

2.3 Network Motifs and Their Stability

In this section, we define network motifs in connected vehicle networks and investigate their stability. In general, network motifs are recurrent subnetworks in complex networks [51]. In vehicle networks, we define motif n (denoted by M_n) as follows.

Definition 5 Motif n (M_n) is a network where a CCC vehicle exploits information received from the vehicle immediately ahead and the vehicle that is n-vehicles away, while each of the other vehicles only responds to the motion of the vehicle immediately ahead.

Figure 2.5 shows motif n for different values of n. The advantage of the motif-based approach is that, by analyzing the dynamics of motifs and characterizing the effects of motif combinations, one can modularly design robust vehicle networks which remain scalable when the network size increases.

Characterizing the system dynamics with a large number of independent parameters is typically not feasible. To make the analysis tractable while keeping the essential heterogeneity, we make the following assumptions. First, we consider three kinds of delays: human reaction time, sensing delay, and communication delay. We assume that the same kind of delays have the same value. Specifically, we use $\tau \approx 0.5$–1.5 [s] for human reaction time and use $\sigma \approx 0.1$–0.4 [s] for communication delay. The symbol ξ may represent human reaction time ($\xi = \tau$) if CCC is used to assist a human driver, communication delay ($\xi = \sigma$) if the CCC vehicle is automatically controlled based on communication, or sensing delay $\xi \approx 0.1$–0.2 [s] if the CCC vehicle monitors the motion of the vehicle immediately ahead by using range sensors. Moreover, we assume that the control gains for links of length k are the same and denoted by α_k, β_k; see Figure 2.5. Finally, we assume that human drivers can be modelled by using the framework (2.17) with $\alpha_{i,j} = \beta_{i,j} = 0$ for $j \neq i-1$. This human driver model has been validated by using traffic data in [68].

Hence, applying (2.17) to each vehicle in M_n leads to

$$
\begin{aligned}
\dot{s}_j(t) &= v_j(t)\,, \\
\dot{v}_j(t) &= \alpha_1\big(V\big(h_{j,j-1}(t-\tau)\big) - v_j(t-\tau)\big) + \beta_1\big(v_{j-1}(t-\tau) - v_j(t-\tau)\big)\,, \\
\dot{s}_n(t) &= v_n(t)\,, \\
\dot{v}_n(t) &= \alpha_1\big(V\big(h_{n,n-1}(t-\xi)\big) - v_n(t-\xi)\big) + \beta_1\big(v_{n-1}(t-\xi) - v_n(t-\xi)\big) \\
&\quad + \alpha_n\big(V\big(h_{n,0}(t-\sigma)\big) - v_n(t-\sigma)\big) + \beta_n\big(v_0(t-\sigma) - v_n(t-\sigma)\big)\,,
\end{aligned}
\tag{2.43}
$$

for $j = 1, \ldots, n-1$. The network M_1 contains only one following vehicle so that its dynamics is governed by the first two equations in (2.43) but with delay ξ. Considering the worst-case scenario for robustness, we assume that all vehicles (including the CCC vehicle) are driven by human drivers. Thus, the stability diagrams are generated for $\xi = \tau$, although formulae are derived for general delay ξ.

Linearizing (2.43) about the equilibrium (2.3) and (2.16) yields

$$
\begin{aligned}
\dot{\tilde{x}}_j(t) &= A_0\tilde{x}_j(t) + A_1\tilde{x}_j(t-\tau) + B_1\tilde{x}_{j-1}(t-\tau)\,, \\
\tilde{v}_j(t) &= C\tilde{x}_j(t)\,, \\
\dot{\tilde{x}}_n(t) &= A_0\tilde{x}_n(t) + A_1\tilde{x}_n(t-\xi) + B_1\tilde{x}_{n-1}(t-\xi) + A_n\tilde{x}_n(t-\sigma) + B_n\tilde{x}_0(t-\sigma)\,, \\
\tilde{v}_n(t) &= C\tilde{x}_n(t)\,,
\end{aligned}
\tag{2.44}
$$

for $j = 1, \ldots, n-1$, where the matrices are given by

$$A_0 = \begin{bmatrix} 0 & 1 \\ 0 & 0 \end{bmatrix}, \quad A_m = \begin{bmatrix} 0 & 0 \\ -\varphi_m & -\kappa_m \end{bmatrix}, \quad B_m = \begin{bmatrix} 0 & 0 \\ \varphi_m & \beta_m \end{bmatrix}, \quad C = \begin{bmatrix} 0 & 1 \end{bmatrix}, \tag{2.45}$$

and

$$\varphi_m = \frac{\alpha_m V'(h^*)}{m}, \quad \kappa_m = \alpha_m + \beta_m, \tag{2.46}$$

for $m = 1, \ldots, n$; cf. (2.18)–(2.20).

Corresponding to the connectivity topology of M_n, formula (2.23) leads to the link transfer functions

$$\begin{aligned} T_{j,j-1}(s) &= \frac{\beta_1 s + \varphi_1}{s^2 \mathrm{e}^{s\tau} + \kappa_1 s + \varphi_1} := T_{\mathrm{h}}(s), \\ T_{n,n-1}(s) &= \frac{(\beta_1 s + \varphi_1)\mathrm{e}^{s(\sigma-\xi)}}{s^2 \mathrm{e}^{s\sigma} + (\kappa_1 s + \varphi_1)\mathrm{e}^{s(\sigma-\xi)} + \kappa_n s + \varphi_n}, \\ T_{n,0}(s) &= \frac{\beta_n s + \varphi_n}{s^2 \mathrm{e}^{s\sigma} + (\kappa_1 s + \varphi_1)\mathrm{e}^{s(\sigma-\xi)} + \kappa_n s + \varphi_n}, \end{aligned} \tag{2.47}$$

for $j = 1, \ldots, n-1$, where $T_{\mathrm{h}}(s)$ denotes the link transfer function for human-driven vehicles. Applying the formula (2.27) yields the HTTF of M_n

$$G_{n,0}(s) = \big(T_{\mathrm{h}}(s)\big)^{n-1} T_{n,n-1}(s) + T_{n,0}(s). \tag{2.48}$$

First, we investigate the plant stability of M_n. Substituting (2.47) into (2.48) leads to the characteristic equation

$$D(s) = \big(s^2 \mathrm{e}^{s\tau} + \kappa_1 s + \varphi_1\big)^{n-1} \big(s^2 \mathrm{e}^{s\sigma} + (\kappa_1 s + \varphi_1)\mathrm{e}^{s(\sigma-\xi)} + \kappa_n s + \varphi_n\big) = 0, \tag{2.49}$$

where the first term is indeed the characteristic polynomial of M_1. When $\Omega > 0$, substituting (2.49) into (2.34), the first term yields

$$\begin{aligned} \alpha_1 &= \frac{\Omega^2 \cos(\Omega\tau)}{V'(h^*)}, \\ \beta_1 &= \Omega \sin(\Omega\tau) - \alpha_1, \end{aligned} \tag{2.50}$$

while the second term leads to

$$\begin{aligned} \alpha_n &= \frac{n}{V'(h^*)} \Big[\Omega^2 \cos(\Omega\sigma) - \varphi_1 \cos\big(\Omega(\sigma-\xi)\big) + \kappa_1 \Omega \sin\big(\Omega(\sigma-\xi)\big)\Big], \\ \beta_n &= \Omega \sin(\Omega\sigma) - \frac{\varphi_1}{\Omega} \sin\big(\Omega(\sigma-\xi)\big) - \kappa_1 \cos\big(\Omega(\sigma-\xi)\big) - \alpha_n, \end{aligned} \tag{2.51}$$

for $n > 1$. When $\Omega = 0$, substituting (2.49) into (2.35) while considering (2.46) leads to the plant stability boundary

$$\alpha_n = -n\alpha_1 \,. \tag{2.52}$$

Using (2.47) and (2.48) in (2.36) yields the $\mathcal{L}_2$-HT string stability boundary

$$\begin{aligned} \alpha_n &= \frac{-2\omega_{\rm cr}^2 Q_1 + P_1 + P_2 Q_2 \pm \sqrt{\Delta}}{2\omega_{\rm cr}^2(1+2Q_2)} \,, \\ \beta_n &= Q_1 + Q_2\alpha_n \,, \end{aligned} \tag{2.53}$$

for $\omega_{\rm cr} > 0$ and $n > 1$. Here, the expressions for $P_1, P_2, Q_1, Q_2, \Delta$ are given by

$$\begin{aligned} P_1 &= \frac{2V'(h^*)}{n} \cdot \mathrm{Re}\Big[\big(\mathrm{j}\beta_1\omega_{\rm cr} + \varphi_1 \mathrm{e}^{\mathrm{j}\omega_{\rm cr}(\sigma-\xi)}\big)\big(T_{\rm h}(\mathrm{j}\omega_{\rm cr})\big)^{n-1}\Big] + 2\omega_{\rm cr}^3 \sin(\omega_{\rm cr}\sigma) \\ &\quad + \frac{2V'(h^*)}{n}\omega_{\rm cr}^2\cos(\omega_{\rm cr}\sigma) + 2\omega_{\rm cr}\left(\frac{V'(h^*)\kappa_1}{n} - \varphi_1\right)\sin(\omega_{\rm cr}(\sigma-\xi)) \\ &\quad - 2\left(\frac{V'(h^*)\varphi_1}{n} + \kappa_1\omega_{\rm cr}^2\right)\cos(\omega_{\rm cr}(\sigma-\xi)) \,, \\ P_2 &= 2\omega_{\rm cr} \cdot \mathrm{Im}\Big[\big(\mathrm{j}\beta_1\omega_{\rm cr} + \varphi_1 \mathrm{e}^{\mathrm{j}\omega_{\rm cr}(\sigma-\xi)}\big)\big(T_{\rm h}(\mathrm{j}\omega_{\rm cr})\big)^{n-1}\Big] \\ &\quad + 2\omega_{\rm cr}^3\sin(\omega_{\rm cr}\sigma) - 2\varphi_1\omega_{\rm cr}\sin(\omega_{\rm cr}(\sigma-\xi)) - 2\kappa_1\omega_{\rm cr}^2\cos(\omega_{\rm cr}(\sigma-\xi)) \,, \end{aligned} \tag{2.54}$$

and

$$\begin{aligned} Q_1 = \frac{\omega_{\rm cr}^2 W' - 2\omega_{\rm cr} W}{2\omega_{\rm cr}P_2 - \omega_{\rm cr}^2 P_2'} \,, \quad Q_2 = \frac{\omega_{\rm cr}^2 P_1' - 2\omega_{\rm cr}P_1}{2\omega_{\rm cr}P_2 - \omega_{\rm cr}^2 P_2'} \,, \\ \Delta = (-2\omega_{\rm cr}^2 Q_1 + P_1 + P_2 Q_2)^2 + 4\omega_{\rm cr}^2(1+2Q_2)(W + P_2 Q_1) \,, \end{aligned} \tag{2.55}$$

where the prime denotes the derivative with respect to $\omega_{\rm cr}$ and

$$W = \Big|\mathrm{j}\beta_1\omega_{\rm cr} + \varphi_1 \mathrm{e}^{\mathrm{j}\omega_{\rm cr}(\sigma-\xi)}\Big|^2 \big|T_{\rm h}(\mathrm{j}\omega_{\rm cr})\big|^{2(n-1)} - \Big|(\mathrm{j}\kappa_1\omega_{\rm cr} + \varphi_1)\mathrm{e}^{\mathrm{j}\omega_{\rm cr}(\sigma-\xi)} - \omega_{\rm cr}^2 \mathrm{e}^{\mathrm{j}\omega_{\rm cr}\sigma}\Big|^2 \,. \tag{2.56}$$

In (2.54)–(2.56), the transfer function $T_{\rm h}(\mathrm{j}\omega_{\rm cr})$ is given in (2.47).

For $\omega_{\rm cr} = 0$, we use (2.47) and (2.48) in (2.37) and obtain the $\mathcal{L}_2$-HT string stability boundaries

$$\alpha_n = -n\alpha_1 \,, \tag{2.57}$$

and

$$\alpha_n = -2\beta_n - \alpha_1 + 2(V'(h^*) - \beta_1) \,. \tag{2.58}$$

Plotting the stability boundaries (2.50)–(2.58) in the $(\beta_n,\, \alpha_n)$-plane leads to the stability diagram, which indicates the feasible regions for choosing control gains to achieve plant stability and $\mathcal{L}_2$-HT string stability.

2.3.1 Stability Diagrams for Motif 1

The head-to-tail transfer function of motif M_1 is $G_{1,0}(s) = T_{\mathrm{h}}(s)$ with delay ξ; cf. (2.47) and (2.48). The plant stability boundaries of M_1 are given by (2.50) and (2.52). For $\omega_{\mathrm{cr}} > 0$, $\mathcal{L}_2$-HT string stability boundaries (2.53) can be simplified to

$$\begin{aligned} \alpha_1 &= \frac{1}{R_3}\left(R_2 \pm \sqrt{R_2^2 + R_3 R_1}\right), \\ \beta_1 &= \frac{\alpha_1\big(\big(V'(h^*)\xi - 1\big)\sin(\omega_{\mathrm{cr}}\xi) - \omega_{\mathrm{cr}}\xi\cos(\omega_{\mathrm{cr}}\xi)\big) + \omega_{\mathrm{cr}}}{\sin(\omega_{\mathrm{cr}}\xi) + \omega_{\mathrm{cr}}\xi\cos(\omega_{\mathrm{cr}}\xi)}, \end{aligned} \tag{2.59}$$

where

$$\begin{aligned} R_1 &= \omega_{\mathrm{cr}}^2(\sin(\omega_{\mathrm{cr}}\xi) - \omega_{\mathrm{cr}}\xi\cos(\omega_{\mathrm{cr}}\xi)), \\ R_2 &= V'(h^*)\big(\omega_{\mathrm{cr}}\xi + \sin(\omega_{\mathrm{cr}}\xi)\cos(\omega_{\mathrm{cr}}\xi)\big) - \omega_{\mathrm{cr}}, \\ R_3 &= \big(2V'(h^*)\xi - 1\big)\sin(\omega_{\mathrm{cr}}\xi) - \omega_{\mathrm{cr}}\xi\cos(\omega_{\mathrm{cr}}\xi). \end{aligned} \tag{2.60}$$

For $\omega_{\mathrm{cr}} = 0$, using $\alpha_n = \beta_n = 0$ in (2.57) and (2.58) yields two solutions

$$\alpha_1 = 0, \tag{2.61}$$

and

$$\alpha_1 = 2(V'(h^*) - \beta_1). \tag{2.62}$$

The stability diagram of motif M_1 is shown in Figure 2.6(a) for the delay $\xi = 0.2$ [s], where the plant stable domain and the $\mathcal{L}_2$-HT string stable domain are shaded by light gray and dark gray, respectively. The red curves denote the plant stability boundaries (2.50) and (2.52) while the blue curves represent the $\mathcal{L}_2$-HT string stability boundaries (2.59)–(2.62). These notations are used in the stability diagrams in the rest of this dissertation. Figure 2.6(b) shows the frequencies Ω and ω_{cr} at which M_1 loses plant stability and $\mathcal{L}_2$-HT string stability, respectively.

In Figure 2.6(a), points A–C are marked to show how plant stability changes when control gains are varied. Figure 2.6(d)–(f) show the corresponding leading characteristic roots, which are obtained by using the numerical continuation package DDE-BIFTOOL [69]. When crossing the plant stability boundary, a pair of complex conjugate characteristic

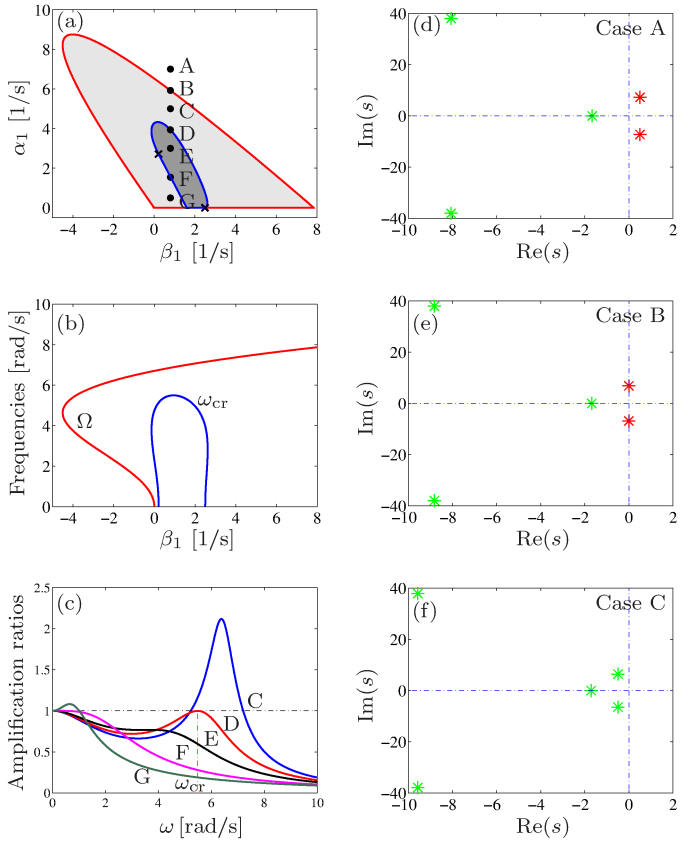

Figure 2.6: (a): Stability diagram of motif M_1 for delay $\xi = 0.2$ [s], showing the plant stable domain (light gray) and the $\mathcal{L}_2$-HT string stable domain (dark gray). The red and the blue curves represent the plant stability boundaries (2.50), (2.52) and the $\mathcal{L}_2$-HT string stability boundaries (2.59)–(2.62), respectively. (b): Frequencies Ω for plant stability (red curve) and ω_{cr} for $\mathcal{L}_2$-HT string stability (blue curve). (c): Amplification ratio curves corresponding to control gains marked by points C–G. (d)–(f): Leading characteristic roots for gains marked by points A–C.

roots move to the right half complex plane. That is, M_1 loses plant stability through a Hopf bifurcation. Points C–G are marked to show how $\mathcal{L}_2$-HT string stability changes with control gains. The corresponding Bode plots are depicted in Figure 2.6(c). Control gains at point E ensures $\mathcal{L}_2$-HT string stability where $|G_{1,0}(\mathrm{j}\omega)| < 1$ for $\forall \omega > 0$. When crossing the boundary for $\omega_{\mathrm{cr}} > 0$ (gains at point D), the system becomes $\mathcal{L}_2$-HT string unstable for mid-range frequencies (gains at point C). On the other hand, gains at point F shows marginal $\mathcal{L}_2$-HT string stability at $\omega_{\mathrm{cr}} = 0$, implying $\mathcal{L}_2$-HT string instability at low frequencies for the gains at point G.

The stability diagrams of motif M_1 are compared in Figure 2.7 for different values of delay ξ, where the same notation is used as in Figure 2.6(a). When the delay ξ increases,

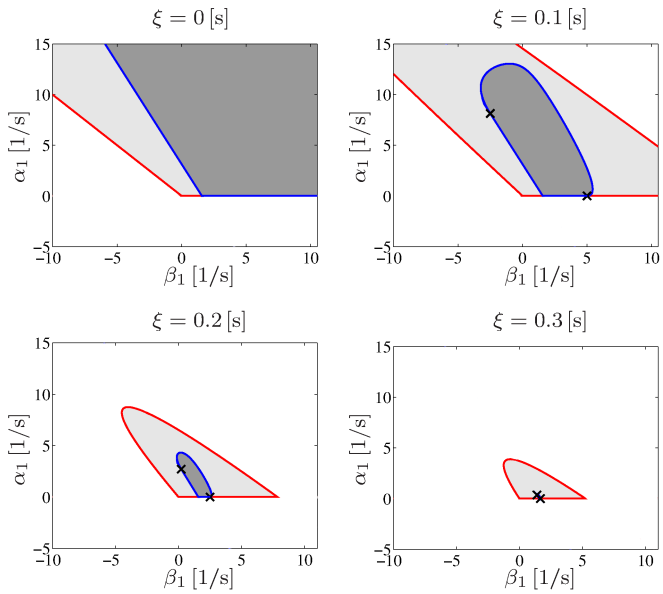

Figure 2.7: Stability diagrams of motif M_1 for different values of delay ξ as indicated. The same notations are used as in Figure 2.6(a).

the stable domains shrink and the $\mathcal{L}_2$-HT string stable domain disappears for a sufficiently large delay. To calculate the critical delay, we investigate how the "anchor points" (marked by crosses) move when the delay ξ varies. Substituting $\omega_{\mathrm{cr}} = 0$ into (2.59) and applying L'Hospital's rule yields the locations of the two crosses:

$$\begin{aligned}(\alpha_1^-, \beta_1^-) &= \left(\frac{2V'(h^*)\xi - 1}{\xi\big(V'(h^*)\xi - 1\big)}, \frac{2\big(V'(h^*)\xi\big)^2 - 4V'(h^*)\xi + 1}{2\xi\big(V'(h^*)\xi - 1\big)} \right), \\ (\alpha_1^+, \beta_1^+) &= \left(0, \frac{1}{2\xi} \right).\end{aligned} \tag{2.63}$$

The $\mathcal{L}_2$-HT string stable domain disappears when these two points meet at $(V'(h^*), 0)$, i.e., $\beta_1^- = \beta_1^+ = V'(h^*)$ and $\alpha_1^- = \alpha_1^+ = 0$, yielding the critical delay

$$\xi_{\mathrm{cr}} = \frac{1}{2V'(h^*)} = \frac{T_{\mathrm{gap}}}{2}. \tag{2.64}$$

If $\xi > \xi_{\mathrm{cr}}$, the $\mathcal{L}_2$-HT string stability of M_1 cannot be achieved for any combination of control gains. For the range policy (2.9) and (2.11) at $h^* = 20$ [m], the critical delay is $\xi_{\mathrm{cr}} \approx 0.325$ [s].

In the remaining part of this chapter, we assume the human reaction time $\tau = 0.5$ [s], which is larger than the critical delay. This implies that human-driven vehicles cannot maintain $\mathcal{L}_2$-HT string stability when $h^* = 20$ [m]. We also assume the control gains

$\alpha_1 = 0.6$ [1/s] and $\beta_1 = 0.7$ [1/s], that is, the human-driven vehicles are plant stable but amplify the disturbance from the vehicle immediately ahead. These parameters will be used for other motifs and motif combinations.

2.3.2 Stability Diagrams for Motif n ($n > 1$)

For motif M_n ($n > 1$), we consider a conservative case where all vehicles (including the CCC vehicle) are driven by human drivers. Based on (2.51)–(2.58), we construct the stability diagram of M_2 for the communication delay $\sigma = 0.2$ [s], which is displayed in Figure 2.8(a). The corresponding frequencies Ω and ω_{cr} are shown in Figure 2.8(e). Points H and I are marked in Figure 2.8(a) to illustrate how the $\mathcal{L}_2$-HT string stability changes when the control gains are varied. For the control gains at point H ($\alpha_2 = \beta_2 = 0$), the V2V communication is not utilized, which leads to the amplification of low-frequency disturbances; see Figure 2.8(b). For the gains at point I, the CCC vehicle 2 exploits the motion data of vehicle 0 received via V2V communication. The amplification ratio curve in Figure 2.8(c) shows that the CCC vehicle 2 can attenuate disturbances at all frequencies even though vehicle 1 amplifies them.

We also demonstrate this phenomenon by simulating the nonlinear model (2.43), as shown in Figure 2.8(f,g). Here, the velocity of vehicle 0 is assumed to be $v_0(t) = v^* + v_{\mathrm{amp}} \sin(\omega t)$, where the sinusoidal term denotes the disturbance. Specifically, we use $v^* = 15$ [m/s], $v_{\mathrm{amp}} = 1$ [m/s], $\omega = 1.45$ [rad/s], and assume the initial distances $h_1(t) \equiv 19$ [m], $h_2(t) \equiv 21$ [m] and initial velocities $v_1(t) \equiv 12$ [m/s], $v_2(t) \equiv 16$ [m/s] along the time interval $t \in [-\tau, 0]$. Vehicle 1 always amplifies the disturbance due to the large delay. For vheicle 2, it will further amplify the disturbance if the V2V communication is not exploited (case H), but it can also attenuate the disturbance by appropriately using the data provided by V2V communication (case I).

For motifs M_n ($n > 1$), $\mathcal{L}_2$-HT string instability may occur for multiple frequency ranges due to the intersection of $\mathcal{L}_2$-HT string stability boundaries for different values of $\omega_{\mathrm{cr}} > 0$; cf. blue curves in Figure 2.8(e). Point J is marked in the vicinity of the intersection in Figure 2.8(a) and the corresponding Bode plot is displayed in Figure 2.8(d), which shows that $|G_{2,0}(\mathrm{j}\omega)| > 1$ in two distinct frequency ranges. To demonstrate this performance, simulations are carried out using the nonlinear model (2.43) and the results are shown in Figure 2.8(h). The velocity of vehicle 0 is prescribed as $v_0(t) = v^* + v_{\mathrm{amp},1} \sin(\omega_1 t) + v_{\mathrm{amp},2} \sin(\omega_2 t)$ with $v^* = 15$ [m/s], $v_{\mathrm{amp},1} = 1$ [m/s], $v_{\mathrm{amp},2} = 1$ [m/s], $\omega_1 = 1.45$ [rad/s], and $\omega_2 = 3.75$ [rad/s], where ω_1 and ω_2 are selected from the first and the second $\mathcal{L}_2$-HT string unstable frequency ranges, respectively. The simulation result in Figure 2.8(h)

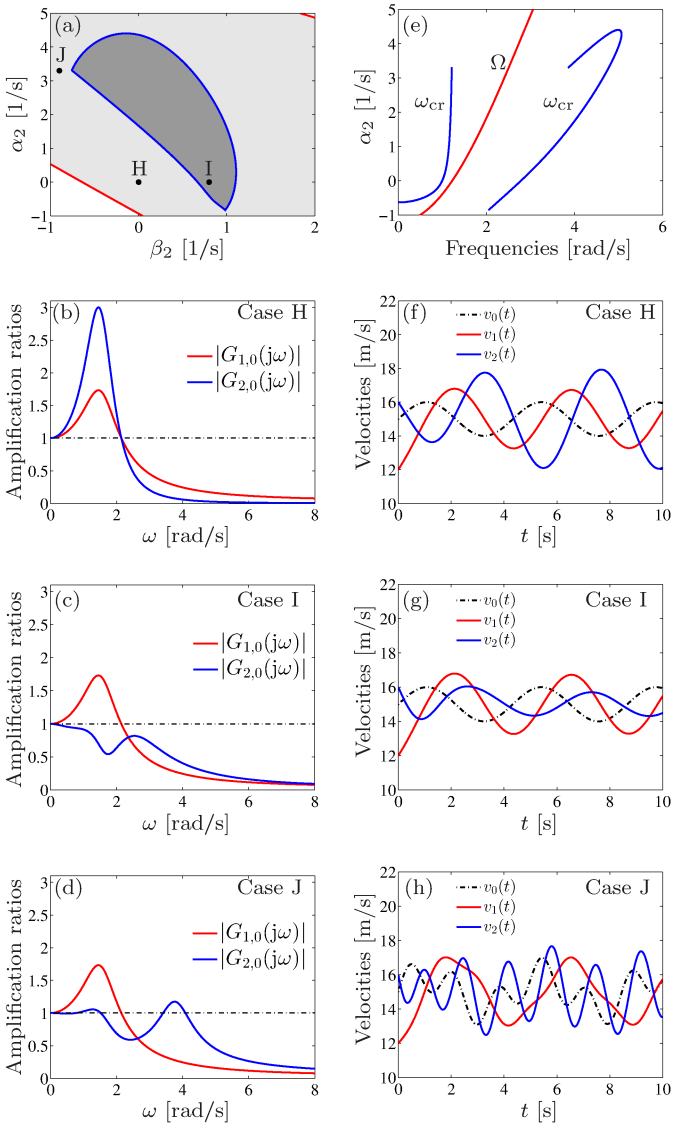

Figure 2.8: (a): Stability diagram of motif M_2 when $\alpha_1 = 0.6$ [1/s], $\beta_1 = 0.7$ [1/s], $\tau = 0.5$ [s], and $\sigma = 0.2$ [s]. The same notation is used as in Figure 2.6(a). (b)–(d): Amplification ratio curves for cases H–J. (e): Frequencies corresponding to the stability boundaries in panel (a). (f)–(h): Simulation results for cases H–J.

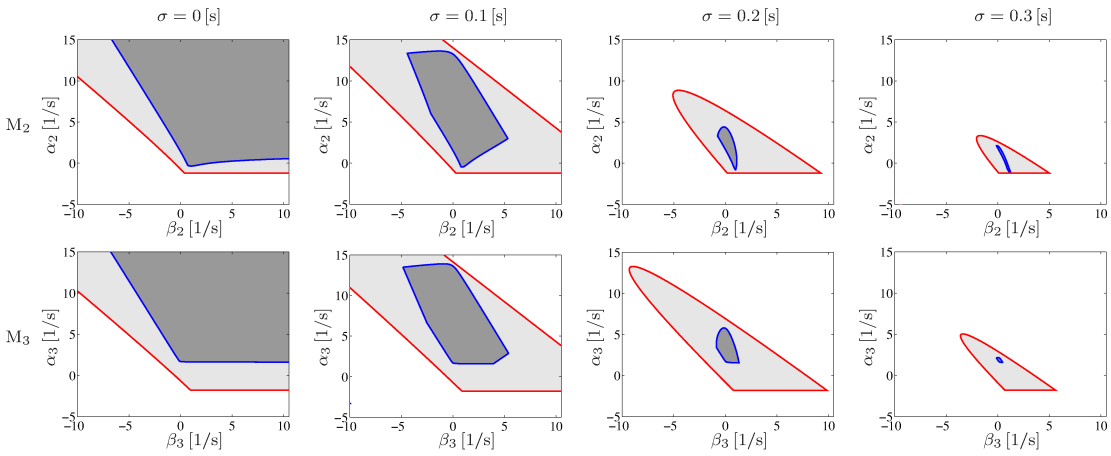

Figure 2.9: Stability diagrams for motifs M_2 (top row) and M_3 (bottom row) for different values of the communication delay σ when $\alpha_1 = 0.6$ [1/s], $\beta = 0.7$ [1/s], and $\tau = 0.5$ [s]. The same notation is used as in Figure 2.6(a).

indicates that vehicle 2 amplifies the disturbances for both frequencies, while vehicle 1 only amplifies the low-frequency disturbance. This implies that CCC vehicles may deteriorate the performance of traffic flow if the control gains are not appropriately designed.

For different values of communication delay σ, we display stability diagrams for M_2 and M_3 in Figure 2.9. Note that control gains α_2, β_2 are used for M_2 while α_3, β_3 are used for M_3. As σ increases, $\mathcal{L}_2$-HT string stable domains decrease and disappear for $\sigma_{\mathrm{cr}} \gtrsim 0.3$ [s], which is larger than the typical communication delay σ=0.1–0.2 [s]. The stability diagrams for M_3 imply that the CCC vehicle may ensure the $\mathcal{L}_2$-HT string stability for a network which contains more than one vehicles that amplify disturbances.

2.4 Motif Combinations

Here, we investigate the effects of motif combinations on the dynamics of complex vehicle networks. In particular, we construct vehicle networks by using the motif combinations *cascade*, *union*, *embedment*, and *intersection*, which are denoted by "$+$", "$\bigcup$", "$\subset$" and "$\bigcap$", respectively. Figure 2.10(a)–(d) display these combinations for general motifs M_m and M_n ($n > m > 1$) while specific examples are presented in Figure 2.10(e)–(h) for 4 vehicles.

Cascades and intersections are defined literally. A union of motifs is formed when the CCC vehicle receives information from multiple distant vehicles ahead. Particularly, for the union network $\mathrm{M}_1 \bigcup \mathrm{M}_2 \bigcup \ldots \bigcup \mathrm{M}_n$, the CCC vehicle makes maximum use of V2V communication; see Figure 2.10(f). A combination is called embedment if a motif is entirely

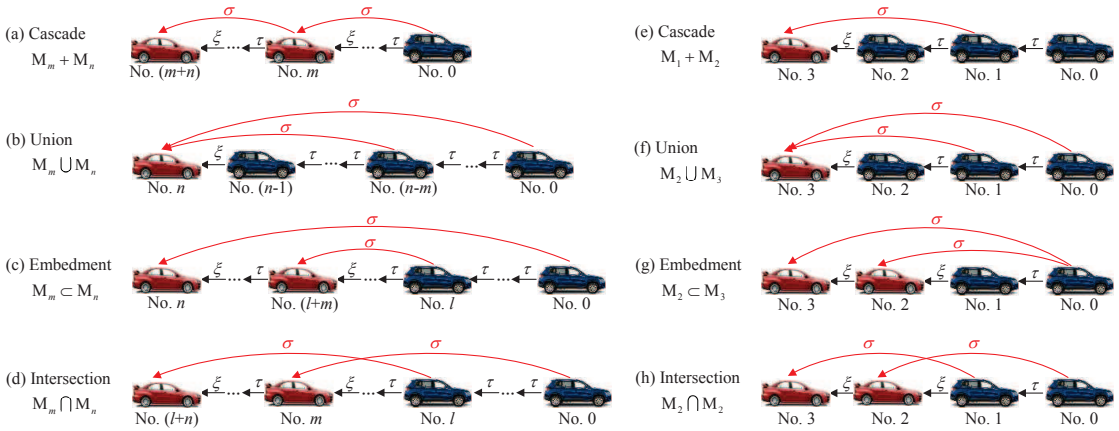

Figure 2.10: Motif combinations (left column) and corresponding examples for (3+1)-vehicle networks (right column).

enclosed by another motif without intersection of links. In this case, each CCC vehicle only receives information from one distant vehicle. We remark that CACC can be considered as a particular embedment network where all vehicles monitor the designated leader; see Figure 2.10(g).

2.4.1 Cascade of Motifs

Cascade networks can be realized by placing motifs one after another such that the tail vehicle of a motif becomes the lead vehicle of another motif. Particularly, the cascade of M_1's represents the conventional car-following scenario where each vehicle only responds to the motion of the vehicle immediately ahead. The stability of cascade networks can be ensured by the stability of each included motif, as stated in the following theorem.

Theorem 7 A cascade network is

1) plant stable if and only if each included motif is plant stable;

2) $\mathcal{L}_2$-HT string stable if each included motif is $\mathcal{L}_2$-HT string stable.

Since the HTTF of a cascade network is equal to the product of the transfer functions of all included motifs, the following two facts hold. 1) The characteristic roots of the cascade network are indeed the characteristic roots of all included motifs; 2) The head-to-tail amplification ratio of the cascade network is the product of the amplification ratios of all included motifs. Then, the proof of Theorem 7 can be completed by using the aforementioned two facts in the conditions (2.31) and (2.33), respectively.

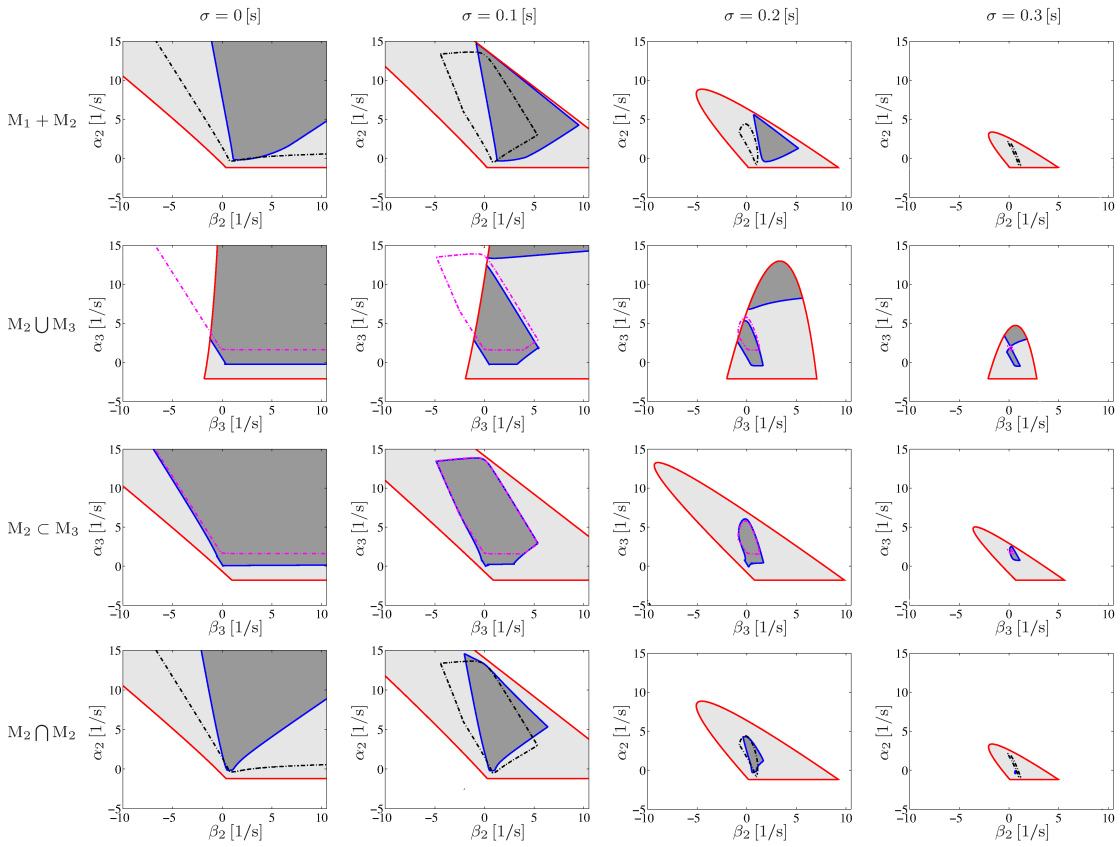

Figure 2.11: Stability diagrams for cascade $\mathrm{M}_1 + \mathrm{M}_2$ (first row), union $\mathrm{M}_2 \bigcup \mathrm{M}_3$ (second row), embedment $\mathrm{M}_2 \subset \mathrm{M}_3$ (third row) and intersection $\mathrm{M}_2 \bigcap \mathrm{M}_2$ (fourth row) for $\alpha_1 = 0.6$ [1/s], $\beta_1 = 0.7$ [1/s], $\xi = \tau = 0.5$ [s], and different values of the communication delay σ as indicated. For $\mathrm{M}_2 \bigcup \mathrm{M}_3$ and $\mathrm{M}_2 \subset \mathrm{M}_3$, $\alpha_2 = 0$ [1/s] and $\beta_2 = 0.8$ [1/s] are also used. The same notation is used as in Figure 2.6(a). For comparison, the stability boundaries of M_2 and M_3 are given by the dashed-dotted black and magenta curves, respectively.

Note that condition 2) in Theorem 7 is only a sufficient condition. It implies that a cascade network can still be $\mathcal{L}_2$-HT string stable even when some motifs in it amplify disturbances. To demonstrate this, we investigate the network $\mathrm{M}_1 + \mathrm{M}_2$ (Figure 2.10(e)). In this case, according to (2.27), the HTTF is

$$G_{3,0}(s) = T_{\mathrm{h}}(s)\big(T_{3,1}(s) + T_{3,2}(s)T_{\mathrm{h}}(s)\big)\,, \tag{2.65}$$

where the link transfer functions $T_{\mathrm{h}}(s)$, $T_{3,1}(s) = T_{2,0}(s)$, $T_{3,2}(s) = T_{2,1}(s)$ are given in (2.47). The human-driven vehicles 1 and 2 amplify disturbances due to large human reaction time; see Section 2.3.1.

Then, using (2.65) in (2.34)–(2.37), one can construct the stability diagrams in the (β_2, α_2)-plane, as displayed in the top row of Figure 2.11, which imply that the CCC ve-

hicle 3 can attenuate disturbances of vehicle 0 when $\sigma \lesssim 0.2$ [s]. Comparing the stable domains of $\mathrm{M}_1 + \mathrm{M}_2$ with those of M_2 (enclosed by black dashed-dotted curve), one may notice that for $\mathrm{M}_1 + \mathrm{M}_2$ the $\mathcal{L}_2$-HT string stable domain disappears for $\sigma = 0.3$ [s], while M_2 can still be stabilized for this delay value. This implies that including string unstable motifs in the cascade may degrade the robustness of the network against communication delays.

2.4.2 Union of Motifs

A union network is formed when a CCC vehicle exploits information of multiple distant vehicles ahead. The network $\mathrm{M}_1 \bigcup \mathrm{M}_2 \bigcup \ldots \bigcup \mathrm{M}_n$ can be observed in Figure 2.1 setting $p = 0$ and $i = n$ while all vehicles broadcast information. Based on (2.27), we obtain the corresponding HTTF

$$G_{n,0}(s) = \sum_{j=0}^{n-1} T_{n,j}(s)\big(T_{\mathrm{h}}(s)\big)^j , \tag{2.66}$$

where $T_{n,j}(s)$ and $T_{\mathrm{h}}(s)$ are given by (2.23) and (2.47), respectively.

Here, we investigate $\mathrm{M}_2 \bigcup \mathrm{M}_3$ as displayed in Figure 2.10(f). For M_2, we set $\alpha_2 = 0$ [1/s] and $\beta_2 = 0.8$ [1/s]; see case I in Figure 2.8(a). This ensures that, when vehicles 0 and 3 are disconnected, M_2 (comprised of vehicles 1,2,3) is still $\mathcal{L}_2$-HT string stable. Substituting (2.66) into (2.34)–(2.37) with $n = 4$, one can generate stability diagrams in the (β_3, α_3)-plane, as shown in the second row of Figure 2.11. Comparing these stable domains with those of M_3 (enclosed by magenta dashed-dotted curve), one may observe that exploiting the information from more vehicles ahead can improve the robustness of vehicle networks against communication delays.

2.4.3 Embedment of Motifs

For the embedment $\mathrm{M}_m \subset \mathrm{M}_n$ $(1 < m < n)$ shown in Figure 2.10(c), we apply the formula (2.27) and get the HTTF

$$G_{n,0}(s) = T_{n,0}(s) + T_{n,n-1}(s)\big(T_{\mathrm{h}}(s)\big)^{n-m-1}\big(T_{l+m,l+m-1}(s)\big(T_{\mathrm{h}}(s)\big)^{m-1} + T_{l+m,l}(s)\big) , \tag{2.67}$$

where link transfer functions are given by (2.47) such that $T_{l+m,l+m-1}(s)$ and $T_{l+m,l}(s)$ are equal to $T_{m,m-1}(s)$ and $T_{m,0}(s)$, respectively.

Substituting (2.67) into (2.34)–(2.37) with $m = 2$ and $n = 3$, one can construct the stability diagrams for $\mathrm{M}_2 \subset \mathrm{M}_3$, as shown in the third row of Figure 2.11. The $\mathcal{L}_2$-HT string

stable domains of $\mathrm{M}_2 \subset \mathrm{M}_3$ are larger than those of M_3 (enclosed by magenta dashed-dotted curves). This implies that embedding CCC vehicles in the network may improve the dynamics of vehicle networks by attenuating disturbances. Comparing the stability diagrams for $\mathrm{M}_2 \bigcup \mathrm{M}_3$ and $\mathrm{M}_2 \subset \mathrm{M}_3$ (the second and the third rows of Figure 2.11), one may observe that utilizing motion data received from multiple vehicles can improve the robustness against communication delays. Moreover, using union instead of embedment also decreases the required number of CCC vehicles to stabilize the network.

2.4.4 Intersection of Motifs

Intersection networks can be constructed by using any motifs. Here, we focus on M_2 intersections where each CCC vehicle monitors the vehicle that is two vehicles ahead, which results in a network with a repetitive connectivity pattern; cf. Figure 2.4 with no links of length 3. We begin with $\mathrm{M}_2 \bigcap \mathrm{M}_2$ (Figure 2.10(h)), for which the formula (2.27) gives the HTTF

$$G_{3,0}(s) = T_{3,1}(s)T_{\mathrm{h}}(s) + T_{3,2}(s)\big(T_{2,1}(s)T_{\mathrm{h}}(s) + T_{2,0}(s)\big)\,, \tag{2.68}$$

where the link transfer functions $T_{\mathrm{h}}(s)$, $T_{3,2}(s) = T_{2,1}(s)$, and $T_{3,1}(s) = T_{2,0}(s)$ are given by (2.47).

Using (2.68) in (2.34)–(2.37) leads to the stability diagrams in (β_2, α_2)-plane, as shown in the fourth row of Figure 2.11. Comparing these stable domains with those of M_2 (enclosed by the black dashed-dotted curve), one may notice that intersecting links deteriorates $\mathcal{L}_2$-HT string stability. Besides $\mathcal{L}_2$-HT string stability, one may also want both CCC vehicles 2 and 3 to be capable of attenuating disturbances with respect to vehicle 0. To achieve this, control gains must be chosen from the overlap between the $\mathcal{L}_2$-HT string stable domain of $\mathrm{M}_2 \bigcap \mathrm{M}_2$ (dark gray region) and that of M_2 (enclosed by the black dashed-dotted curve). Such overlap is shaded by "\" lines in Figure 2.12(b) for $\sigma = 0.2$ [s].

To further investigate the effects of link intersections, we compare the dynamics of $\mathrm{M}_2 + \mathrm{M}_2$ and $\mathrm{M}_2 \bigcap \mathrm{M}_2 \bigcap \mathrm{M}_2$; see Figure 2.12(a). As discussed in Section 2.4.1, $\mathrm{M}_2 + \mathrm{M}_2$ and M_2 have the same stable domain. In Figure 2.12(c), the dark gray domain enclosed by the solid blue curve shows the $\mathcal{L}_2$-HT string stable domain of $\mathrm{M}_2 \bigcap \mathrm{M}_2 \bigcap \mathrm{M}_2$ for $\sigma = 0.2$ [s]. The $\mathcal{L}_2$-HT string stable domains of $\mathrm{M}_2 \bigcap \mathrm{M}_2$ and $\mathrm{M}_2 + \mathrm{M}_2$ are enclosed by the dashed blue and dashed-dotted black curves, respectively. The "\" line-shaded domain indicates the overlap of these three domains, where all CCC vehicles can attenuate disturbances with respect to vehicle 0. The Bode plots corresponding to the points K and L are shown in Figure 2.12(d) and (e), respectively. Panels (c) and (d) show that the $\mathcal{L}_2$-HT string stability of

CCC vehicles 2–4 can be ensured if control gains are chosen from the "\" line-shaded domain. Panels (c) and (e) demonstrate that $\mathrm{M}_2 + \mathrm{M}_2$ has a larger $\mathcal{L}_2$-HT string stable domain than $\mathrm{M}_2 \bigcap \mathrm{M}_2 \bigcap \mathrm{M}_2$, even though more CCC vehicles are included in the latter network. This implies that, if the connectivity structure is not appropriately designed, increasing the number of CCC vehicles may deteriorate the performance of a vehicle network.

Repeating the aforementioned process, one can obtain stability diagrams for M_2 intersections of any given size, as shown in Figure 2.13(a)–(c). As the network size n increases, the dark gray domain converges to the "/" line-shaded domain (enclosed by the cyan curve), which indicates the $\mathcal{L}_2$-HT stable domain as $n \to \infty$ and can be obtained by substituting $T_1(s) = T_{2,1}(s)$ and $T_2(s) = T_{2,0}(s)$ into (2.41) and (2.42). The "\" line-shaded domain is the overlap of $\mathcal{L}_2$-HT string stable domains for all M_2 intersections of size up to n; cf. Figure 2.12(b) and (c). This domain ensures that all CCC vehicles can attenuate disturbances with respect to the head vehicle.

In Figure 2.13(a), points M–P are marked to show the system performance when the control gains are chosen from different domains. To evaluate the disturbance attenuation of vehicle i, we use the criterion $\ln\left(\max_{\omega\geq 0}\left(|G_{i,0}(\mathrm{j}\omega)|\right)\right) = 0$ (cf. (2.33)) and show corresponding results in Figure 2.13(d)–(f). Note that the human-driven vehicle 1 always amplifies disturbances due to large delay $\tau > \xi_{\mathrm{cr}}$; cf. (2.64). One can observe that the control gains from the dark gray domain (case M) only ensure the $\mathcal{L}_2$-HT string stability of vehicle 10 but the disturbance is amplified for larger network size, as shown in Figure 2.13(d). When control gains are chosen from the "/" line-shaded domain (case N), it can eliminate the disturbances as $n \to \infty$ although some vehicles ahead amplify the disturbances, as shown in Figure 2.13(e). Control gains in the cross-shaded domain, which is the overlap between the "\" line-shaded and the "/" line-shaded domains (case P), ensure the string stability of all CCC vehicles, as shown in Figure 2.13(f). We remark that this cross-shaded domain does not significantly change with the network size.

When designing M_2 intersections, control gains should be chosen from the cross-shaded domain, which is smaller than the stable domain for M_2 cascades (enclosed by the black dashed-dotted curve). Moreover, in terms of the same network size, the cascade network uses less CCC vehicles than the intersection network. This implies that the intersection of communication links may deteriorate performance of vehicle networks. Suppose that the received information includes the connectivity topologies of other vehicles. Then, the CCC vehicle can disconnect the intersected links to improve the performance of traffic flow.

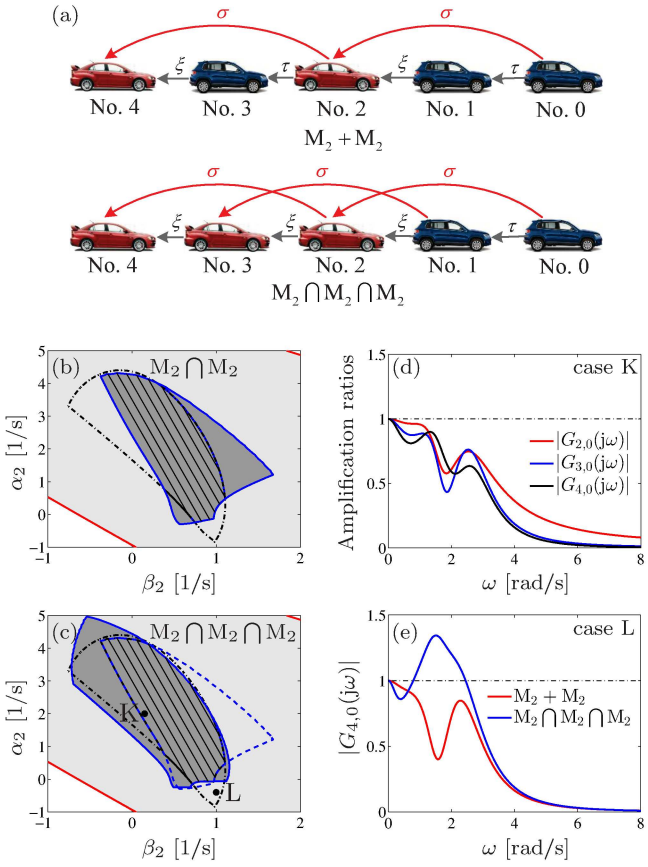

Figure 2.12: (a): Networks $M_2 + M_2$ and $M_2 \bigcap M_2 \bigcap M_2$. (b,c): Stability diagrams of $M_2 \bigcap M_2$ and $M_2 \bigcap M_2 \bigcap M_2$ for $\sigma = 0.2$ [s]. The solid blue curves represent stability boundaries for $M_2 \bigcap M_2$ and $M_2 \bigcap M_2 \bigcap M_2$ while the black dashed-dotted curve denotes the stability boundary of M_2. For comparison, the stability boundary of $M_2 \bigcap M_2$ is reproduced in panel (c) using dashed blue curve. Shading has the same meaning as in Figure 2.6(a) while the "\" line-shaded domain highlights where all CCC vehicles can attenuate disturbances respect to vehicle 0. (d,e): Bode plots corresponding to the gains marked by points K and L in (c).

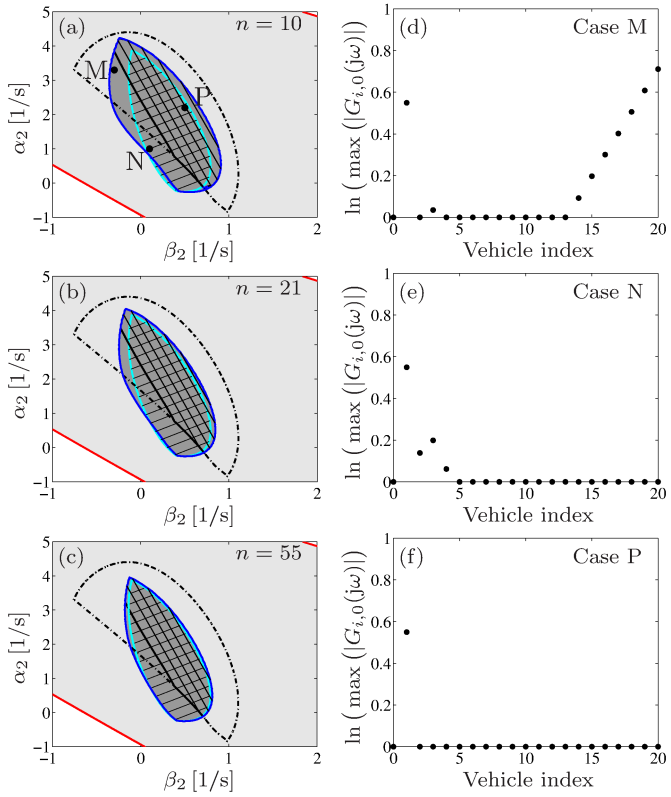

Figure 2.13: (a)–(c): Stability diagrams for M_2 intersections of different size as indicated by n. The black dashed-dotted curve encloses the $\mathcal{L}_2$-HT string stable domain for M_2. The "\" line-shaded domain is the overlap of the $\mathcal{L}_2$-HT string stable domains for all M_2 intersections of size up to n. The "/" line-shaded region enclosed by the cyan curve indicates the $\mathcal{L}_2$-HT string stable domain for $n \to \infty$. Other shadings are the same as in Figure 2.6(a). (d)–(f): Stability evaluations corresponding to points M–P.

2.5 Summary

In this chapter, we presented a general controller for the planning level of CCC that generated desired car-following dynamics by incorporating the motion data received from multiple vehicles ahead via V2V communication. Information delays and connectivity topologies were taken in account. This controller ensured the existence of a unique uniform flow equilibrium that was independent of the network size, connectivity topology, information delays, and control gains. Then, we investigated the dynamics of connected vehicle networks in the vicinity of uniform flow equilibrium. A systematic and efficient method was provided to calculate the head-to-tail transfer function, which was crucial for characterizing the stability of vehicle networks. Then, a motif-based approach was proposed for modular and scalable design of complex vehicle networks. The dynamics of fundamental

motifs and the effects of motif combinations were investigated, and the corresponding results were summarized by using stability diagrams for choosing control gains. Numerical simulation showed that V2V communication can be used to improve the dynamics of traffic flow if the control gains and the connectivity topologies are appropriately designed. On the other hand, the results also showed that CCC may deteriorate the performance of vehicle networks if the connectivity topologies and control gains are not appropriately designed.

The analysis in this chapter was based on the linearized models that only governed the dynamics in the vicinity of equilibrium. In the next chapter, we will investigate the impact of nonlinear dynamics on the performance of vehicle networks.

CHAPTER 3

Planning Level: Nonlinear Dynamics of Connected Vehicle Networks

In this chapter, we investigate the nonlinear dynamics of the planning-level controller presented in Chapter 2. Corresponding stability conditions are derived for designing control gains for plant stability, $\mathcal{L}_p$-HT string stability, and eventual string stability.

3.1 Plant Stability

Substituting (2.3) and (2.16) into (2.17) and subtracting the result from (2.17), we obtain

$$\begin{aligned}\dot{\tilde{s}}_i(t) &= \tilde{v}_i(t)\,,\\ \dot{\tilde{v}}_i(t) &= \sum_{j=p}^{i-1}\Big[\alpha_{i,j}\big(V\big(h_{i,j}(t-\xi_{i,j})\big)-V(h^*)-\tilde{v}_i(t-\xi_{i,j})\big)\\ &\qquad\qquad +\beta_{i,j}\big(\tilde{v}_j(t-\xi_{i,j})-\tilde{v}_i(t-\xi_{i,j})\big)\Big]\,,\end{aligned} \tag{3.1}$$

In practice, it is often desired to maintain the distance and the velocity in the given operating domains, that is,

$$h_{k,k-1}(t)\in\mathcal{D}_h\triangleq\{h:\ \underline{h}\le h\le\overline{h}\}\,,\quad\text{and}\quad v_k(t)\in\mathcal{D}_v\triangleq\{v:\underline{v}\le v\le\overline{v}\}\,, \tag{3.2}$$

for all $t\ge 0$ and for all k-s, where positive constants $\underline{h}$, $\overline{h}$, $\underline{v}$, and $\overline{v}$ are given bounds. In terms of the range policy (2.9), we assume $h_{\rm st}<\underline{h}<\overline{h}<h_{\rm go}$ and $0<\underline{v}<\overline{v}<v_{\max}$. It follows that $h_{i,j}(t),h^*\in\mathcal{D}_h$ for $i,j=1,\ldots,n$ and $v^*\in\mathcal{D}_v$; cf. (2.15). Since $V(h)$ is continuously differentiable, based on the mean value theorem [70], there exist variables

$\psi_{i,j} \in \mathcal{D}_h$ such that

$$V(h_{i,j}(t)) - V(h^*) = V'(\psi_{i,j})\big(h_{i,j}(t) - h^*\big) = \frac{V'(\psi_{i,j})}{i-j}\big(\tilde{s}_j(t) - \tilde{s}_i(t)\big)\,, \tag{3.3}$$

cf. (2.15). We remark that the expression of $\psi_{i,j}$ is unique if $V'(h)$ is invertible for $\forall h \in \mathcal{D}_h$, while the value of $\psi_{i,j}$ exists but may be not unique if $V'(h)$ is not invertible. In the subsequent analysis, we only need the existence of $\psi_{i,j}$. Note that $\psi_{i,j} = h^*$ when $h_{i,j}(t) = h^*$.

Substituting (3.3) into (3.1) and writing the result in the matrix form, we obtain

$$\dot{\tilde{x}}_i(t) = A_{i,0}\,\tilde{x}_i(t) + \sum_{j=p}^{i-1}\Big(A_{i,j}(\psi_{i,j})\,\tilde{x}_i(t-\xi_{i,j}) + B_{i,j}(\psi_{i,j})\,\tilde{x}_j(t-\xi_{i,j})\Big)\,, \tag{3.4}$$

where $\tilde{x}_i(t)$ is given in (2.5) and the matrices are defined as

$$A_{i,0} = \begin{bmatrix} 0 & 1 \\ 0 & 0 \end{bmatrix}\,, \quad A_{i,j}(\psi_{i,j}) = \begin{bmatrix} 0 & 0 \\ -\varphi_{i,j}(\psi_{i,j}) & -\kappa_{i,j} \end{bmatrix}\,, \quad B_{i,j}(\psi_{i,j}) = \begin{bmatrix} 0 & 0 \\ \varphi_{i,j}(\psi_{i,j}) & \beta_{i,j} \end{bmatrix}\,, \tag{3.5}$$

for $j = p, \ldots, i-1$, where

$$\varphi_{i,j}(\psi_{i,j}) = \frac{\alpha_{i,j}V'(\psi_{i,j})}{i-j}\,, \quad \kappa_{i,j} = \alpha_{i,j} + \beta_{i,j}\,. \tag{3.6}$$

Note that the model (3.4) is indeed nonlinear since the matrices $A_{i,j}(\psi_{i,j})$ and $B_{i,j}(\psi_{i,j})$ depend on states $h_{i,j}$ nonlinearly; cf. (3.3). This is different from the linearized model (2.18)–(2.20), where all matrices are constant.

One common approach to ensure plant stability in nonlinear time-delayed networks is to construct a Lyapunov functional for the whole network, which is challenging especially when the network contains a large number of vehicles. Here, we simplify the analysis by exploiting the property of the "forward-looking" chain topology, that is, adding an vehicle at the tail does not affect the dynamics of vehicles ahead. This allows one to achieve the plant stability of vehicle chains sequentially by ensuring the newly added vehicle can approach the uniform flow equilibrium asymptotically. That is, when studying the plant stability of vehicle i, we assume that all vehicles ahead are in the uniform flow equilibrium, i.e., $\tilde{x}_j(t) \equiv 0$ for $j = p, \ldots, i-1$. Considering this in (3.4) yields

$$\dot{\tilde{x}}_i(t) = A_{i,0}\,\tilde{x}_i(t) + \sum_{j=p}^{i-1} A_{i,j}(\psi_{i,j})\,\tilde{x}_i(t-\xi_{i,j})\,. \tag{3.7}$$

Note that in (3.7) the delays between different pairs of vehicles may have the same value. To eliminate such redundancy, we define an ordered set that contains different values of delays

$$\sigma_i \triangleq \{\sigma_{i,0}, \sigma_{i,1}, \ldots, \sigma_{i,m}\}\,, \tag{3.8}$$

where $\sigma_{i,0} = 0$, $m \leq i-p$, and $\sigma_{i,k} < \sigma_{i,\ell}$ for $k < \ell$ such that the set σ_i is equivalent to the set $\{0, \xi_{i,p}, \ldots, \xi_{i,i-1}\}$. Here, we include 0 as an element in the set σ_i to make the subsequent expressions more compact. Then, one can rewrite (3.7) by collecting the terms with same delays, which leads to

$$\dot{\tilde{x}}_i(t) = \sum_{k=0}^{m} \hat{A}_{i,k}(\Psi_i)\, \tilde{x}_i(t-\sigma_{i,k})\,, \tag{3.9}$$

where $\Psi_i = [\psi_{i,p}, \ldots, \psi_{i,i-1}] \in \mathcal{D}_h^{i-p}$ and the superscript $i-p$ refers to the direct product of $\mathcal{D}_h$ by $i-p$ times. Note that models (3.7) and (3.9) are equivalent but describe the system from different aspects. In particular, the model (3.7) highlights the connectivity topology, while the model (3.9) emphasizes different information delays.

Based on the Newton-Leibniz formula, we have the identity

$$\tilde{x}_i(t-\sigma_{i,k}) = \tilde{x}_i(t) - \int_{t-\sigma_{i,k}}^{t} \dot{\tilde{x}}_i(\tau)\,\mathrm{d}\tau = \tilde{x}_i(t) - \sum_{\ell=1}^{k} \int_{t-\sigma_{i,\ell}}^{t-\sigma_{i,\ell-1}} \dot{\tilde{x}}_i(\tau)\,\mathrm{d}\tau\,. \tag{3.10}$$

Substituting (3.10) into (3.9) results in

$$\dot{\tilde{x}}_i(t) = \overline{A}_{i,0}(\Psi_i)\, \tilde{x}_i(t) - \sum_{q=1}^{m} \overline{A}_{i,q}(\Psi_i) \int_{t-\sigma_{i,q}}^{t-\sigma_{i,q-1}} \dot{\tilde{x}}_i(\tau)\,\mathrm{d}\tau\,, \tag{3.11}$$

where

$$\overline{A}_{i,q}(\Psi_i) = \sum_{k=q}^{m} \hat{A}_{i,k}(\Psi_i)\,, \quad q = 0, \ldots, m\,. \tag{3.12}$$

To save space, we will not spell out the argument Ψ_i in $\hat{A}_{i,k}(\Psi_i)$ and $\overline{A}_{i,q}(\Psi_i)$ in the rest of this chapter. Then, based on (3.9) and (3.11), we provide a sufficient condition for plant stability of CCC vehicle i in the following theorem.

Theorem 8 Suppose that vehicles $j = p, \ldots, i-1$ are in the uniform flow equilibrium with $h^* \in \mathcal{D}_h$ and $v^* = V(h^*) \in \mathcal{D}_v$; cf. (2.3), (2.16) and (3.2). Then, vehicle i is plant stable if there exist positive definite matrices $P_i, Q_{i,1}, \ldots, Q_{i,m}, R_{i,2}, \ldots, R_{i,m}, W_{i,1}, \ldots W_{i,m}$ such

that the following matrices

$$\Xi_{i,1} = \begin{bmatrix} Z & Y_{0,1} & \cdots & Y_{0,m} & -P_i\overline{A}_{i,1} \\ Y_{1,0} & Y_{1,1} - Q_{i,1}/\sigma_{i,1} & \cdots & Y_{1,m} & 0_{2\times 2} \\ \vdots & \vdots & \ddots & \vdots & \vdots \\ Y_{m,0} & Y_{m,1} & \cdots & Y_{m,m} - Q_{i,m}/\sigma_{i,1} & 0_{2\times 2} \\ -\overline{A}_{i,1}^{\mathrm{T}} P_i & 0_{2\times 2} & \cdots & 0_{2\times 2} & -W_{i,1} \end{bmatrix}, \tag{3.13}$$

$$\Xi_{i,q} = \begin{bmatrix} -R_{i,q} & -P_i\overline{A}_{i,q} \\ -\overline{A}_{i,q}^{\mathrm{T}} P_i & -W_{i,q} \end{bmatrix}$$

are negative definite over the domain $\mathcal{D}_h^{i-p}$ for $q = 2, \ldots, m$, where $0_{2\times 2}$ denotes the 2-dimensional zero matrix and

$$\begin{aligned} Y_{j,k} &= \frac{1}{\sigma_{i,1}} \left(\sum_{q=1}^{m} (\sigma_{i,q} - \sigma_{i,q-1}) \hat{A}_{i,j}^{\mathrm{T}} \, W_{i,q} \, \hat{A}_{i,k} \right), \quad j,k = 0, \ldots, m\,, \\ Z &= \frac{1}{\sigma_{i,1}} \left(P_i \, \overline{A}_{i,0} + \overline{A}_{i,0}^{\mathrm{T}} \, P_i + \sum_{q=1}^{m} Q_{i,q} + \sum_{\ell=2}^{m} (\sigma_{i,\ell} - \sigma_{i,\ell-1}) R_{i,j} + \sigma_{i,1} \, Y_{0,0} \right). \end{aligned} \tag{3.14}$$

Note that $\Xi_{i,k}$ in (3.13) depends on Ψ_i for $k = 1, \ldots, m$; cf. (3.9) and (3.12), while the domain $\mathcal{D}_h^{i-p}$ contains all possible values of Ψ_i. The proof of Theorem 8 is given in Appendix A.2. When applying this theorem, we begin by discretizing the domain $\mathcal{D}_h^{i-p}$, and then solve the corresponding linear matrix inequalities (LMIs) numerically for $P_i, Q_{i,1}, \ldots, Q_{i,m}, R_{i,2}, \ldots, R_{i,m}, W_{i,1}, \ldots, W_{i,m}$ by using LMI numerical solvers. Note that the obtained solutions must ensure that the LMIs hold for all values in the domain $\mathcal{D}_h^{i-p}$. We remark that there may exist multiple solutions but we stop the calculation when a solution is found.

Theorem 8 ensures that vehicle i approaches the uniform flow equilibrium if its distance and velocity always stay inside the given operating domain (3.2), that is,

$$z_i(t) \triangleq [h_{i,i-1}(t)\,, v_i(t)]^{\mathrm{T}} \in \mathcal{D}_h \times \mathcal{D}_v \tag{3.15}$$

for all t. Thus, it is also important to find the *feasible region*.

Definition 6 Given a time-delayed system $\dot{z}(t) = f\big(z(t), z(t-\sigma_1), \ldots, z(t-\sigma_m)\big)$, where $z(t) \in \mathbb{R}^n$ is the state while $\sigma_1, \ldots, \sigma_m$ denote time delays with σ_m being the maximum time delay. Let $\mathcal{D} \subset \mathbb{R}^n$ be the operating domain. The feasible region $\mathcal{R}_{\mathrm{F}} \subseteq \mathcal{D}$ is defined such that, if $z(\theta) \in \mathcal{R}_{\mathrm{F}}$ for $\forall \theta \in [-\sigma_m, 0]$, then $z(t) \in \mathcal{D}$ for $\forall t \geq 0$ and $\lim_{t\to\infty} z(t) = z^*$, where z^* denotes the equilibrium.

Compared with the *region of attraction*

$$\mathcal{R}_{\mathrm{A}} = \left\{ z(\theta) \in C\big([-\sigma_m, 0], \mathbb{R}^n\big) : \lim_{t\to\infty} z\big(t; z(\theta)\big) = z^* \right\}, \tag{3.16}$$

defined for time-delayed systems [71], the feasible region is more applicable in our problem due to the following two reasons:

- Feasible region is defined in the finite-dimensional state space $\mathbb{R}^n$ while region of attraction is defined in infinite-dimensional space $C\big([-\sigma_m, 0], \mathbb{R}^n\big)$.
- Feasible region takes into account the constraint of the operating domain while region of attraction does not.

How to calculate the feasible region analytically is a challenging problem and left for future research. Assuming constant initial state, we can approximate the feasible region numerically, as will be demonstrated in Section 3.4.

3.2 Head-to-Tail String Stability

In a vehicle network, disturbances arising from a vehicle affect the motion of the following vehicles. For temporary disturbances, the vehicle network may reach the uniform flow equilibrium after transients. Thus, here we consider persistent disturbances and investigate their impacts on the dynamics of vehicle networks. For nonlinear networks, $\mathcal{L}_2$-HT string stability can be guaranteed by applying the Hamilton-Jacobi inequality [72]. However, to apply this method to nonlinear time-delayed networks, one needs to construct a Lyapunov functional for the whole network, which is challenging especially when the network contains a large number of vehicles. Moreover, the result of the Hamilton-Jacobi inequality is typically quite conservative and may not lead to a solution for large networks. Furthermore, the Hamilton-Jacobi inequality may not guarantee network performance in other $\mathcal{L}_p$ norms such as $\mathcal{L}_\infty$ norm, which is used to evaluate the largest deviation from the uniform flow equilibrium. Here, we investigate $\mathcal{L}_p$-HT string stability conditions that can be used in general norms while also remaining scalable for large networks.

Note that $\mathcal{L}_p$-HT string stability is evaluated by using the steady-state response; see Definition 3. Since general disturbance signals may not lead to steady-state response, we consider periodic disturbances imposed on the lead vehicle. We begin by providing a sufficient condition which ensures that a periodic input to the nonlinear time-delayed network (2.17) leads to periodic steady states with the same period, as stated in the following theorem.

Theorem 9 Consider the vehicle network (2.17) and assume that the disturbance arising from head vehicle 0 is T-periodic. If Theorem 8 holds, then the steady-state motion of vehicles $k = 1, \ldots, n$ is unique and T-periodic, that is,

$$\tilde{x}_k^{(\mathrm{s})}(t+T) = \tilde{x}_k^{(\mathrm{s})}(t)\,, \quad k = 1, \ldots, n\,, \tag{3.17}$$

where the superscript "(s)" denotes the steady state.

The proof of Theorem 9 is given in Appendix A.3. We remark that, for general nonlinear time-delayed networks, periodic disturbances from the head vehicle do not necessarily lead to periodic motion of the following vehicles. By applying the controller (2.12) to the vehicle network (2.2), Theorem 9 can ensure a periodic steady state of the whole vehicle network when a periodic disturbance is imposed on the head vehicle. This property allows one to investigate the $\mathcal{L}_p$-HT string stability by evaluating the frequency response. Thus, in order to investigate the $\mathcal{L}_p$-HT string stability, we consider sinusoidal disturbances and study the frequency response at the nonlinear level. In particular, for the head vehicle 0, we assume

$$\tilde{x}_0(t) = \begin{bmatrix} \tilde{s}_0(t) \\ \tilde{v}_0(t) \end{bmatrix} = \begin{bmatrix} v_{\mathrm{amp}} \sin(\omega t)/\omega \\ v_{\mathrm{amp}} \cos(\omega t) \end{bmatrix}\,, \tag{3.18}$$

where $v_{\mathrm{amp}} > 0$ and $\omega > 0$ denote the amplitude and the frequency of the disturbance, respectively. Since $\tilde{x}_0(t)$ is periodic with period $T = 2\pi/\omega$, Theorem 9 ensures that the steady states of all following vehicle are unique and T-periodic. However, due to nonlinear dynamics, the steady states are not sinusoidal but may be expressed by Fourier series.

To evaluate the frequency response, we define the amplification ratio function

$$\Phi_{n,0}(\omega, v_{\mathrm{amp}}) \triangleq \|\tilde{v}_n^{(\mathrm{s})}\|_{\mathcal{L}_p} / \|\tilde{v}_0^{(\mathrm{s})}\|_{\mathcal{L}_p}\,, \tag{3.19}$$

which describes how the velocity disturbance arising from the head vehicle 0 is amplified or attenuated when reaching the tail agent n in steady state. Different norms can be sued to characterize the magnitude of signals. Here, we use the $\mathcal{L}_\infty$ norm defined by $\|\tilde{v}\|_{\mathcal{L}_\infty} \triangleq \sup_{t>0} |\tilde{v}(t)|$, which accounts for the largest deviations from the equilibrium. Note that the amplification ratio of nonlinear networks (3.19) depends on both the input frequency and the input amplitude. This is different from the amplification ratio of LTI systems, which is only determined by the input frequency. Moreover, for LTI systems with sinusoidal excitations, $\mathcal{L}_\infty$-HT string stability is equivalent to $\mathcal{L}_2$-HT string stability, since both of them are determined by the amplitude of the sinusoidal output. However, they are not equivalent for nonlinear systems, because the output may be not sinusoidal. Then, we

present a condition for L_p-HT string stability in presence of sinusoidal disturbances, as stated in the following theorem.

Theorem 10 Suppose that Theorem 8 holds and the disturbance imposed on the head vehicle 0 is sinusoidal given by (3.18). Then, the vehicle network is $\mathcal{L}_p$-HT string stable if and only if

$$\sup_{\omega>0} \Phi_{n,0}(\omega, v_{\text{amp}}) < 1\,. \tag{3.20}$$

The proof can be given by combining Theorem 9 with Definition 3 and (3.19). To apply Theorem 10, an expression of the steady state of the tail vehicle n is needed, which may not be obtained in the closed form for general nonlinearities. Here, we approximate the steady-state response by applying Taylor expansion. To improve readability, the details of calculation are given in Appendix A.4. Compared with the harmonic balance approach [73], our results provide analytical approximation of the steady states, which simplifies the analysis and remains scalable for large complex networks. Note that Theorem 10 provides guidelines for choosing control gains but may not guarantee $\mathcal{L}_p$-HT string stability for other types of periodic disturbances.

3.3 Eventual String Stability

In this section, we study the eventual string stability of the nonlinear time-delayed network (2.17), and we derive a condition that only requires the analysis of the corresponding linearized model. According to the analysis in Chapter 2, one can obtain the HTTF of an $(n+1)$-vehicle network

$$\tilde{V}_n(s) = G_{n,0}(s, h^*)\tilde{V}_0(s)\,. \tag{3.21}$$

Note that, different from the transfer function (2.27) in Chapter 2, we also treat the equilibrium h^* as a variable in (3.21).

Theorem 11 The vehicle network (2.17) is eventual string stable if all the following conditions hold:

- Theorem 8 holds.
- The range policy function $V(h)$ in (2.9) satisfies

$$\left|\frac{\mathrm{d}^{k+1}V(h)}{\mathrm{d}\,h^{k+1}}\right| < \left|\frac{\mathrm{d}^{k}V(h)}{\mathrm{d}\,h^{k}}\right| < 1\,, \quad \text{and} \quad \lim_{n\to\infty}\left|\frac{\mathrm{d}^{n}V(h)}{\mathrm{d}\,h^{n}}\right| = 0\,, \tag{3.22}$$

  for all $k > 1$ and for all $h_{\text{st}} < h < h_{\text{go}}$.

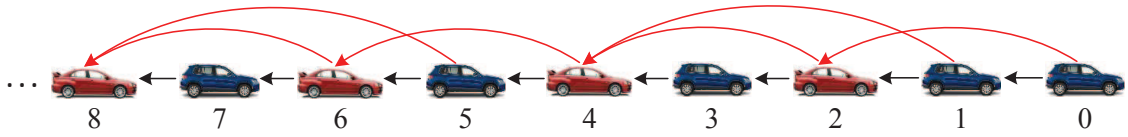

Figure 3.1: A cascading vehicle chain with recurrent connectivity topology; compare agents 0–4 and 4–8.

- The magnitude of the HTTF $G_{n,0}(s, h^*)$ given by (3.21) is always smaller than 1, that is,

$$\sup_{\omega>0,\, h^*\in\mathcal{D}_h} \left|G_{n,0}(\mathrm{j}\omega, h^*)\right| < 1, \tag{3.23}$$

  where $\mathrm{j}^2 = -1$.

The proof is given in Appendix A.5. Theorem 11 reduces the analysis complexity in two aspects. On the one hand, it allows one to analyze disturbance attenuation in nonlinear time-delayed networks by only studying the linearized model. On the other hand, it allows one to ensure the performance of cascading networks by only analyzing the dynamics of a single block. Note that in Theorem 11, one must ensure that the condition (3.23) holds for all possible values of h^* in the domain $\mathcal{D}_h$. This is different from the analysis of the linearized dynamics, which only needs to satisfy (3.23) for certain value of $h^* \in \mathcal{D}_h$.

3.4 Case Study and Simulations

In this section, we apply the theorems presented in this chapter to the vehicle network shown in Figure 3.1. We assume that all vehicles are driven by human drivers with reaction time $\xi_{k,k-1} = 0.5$ [s] and fixed control gains $\alpha_{k,k-1} = 0.3$ [1/s] and $\beta_{k,k-1} = 0.5$ [1/s] for $k = 1, 2, \ldots$. Moreover, we assume that every $(2k-1)$-th vehicle is a non-CCC vehicle while every $2k$-th vehicle is equipped with CCC. We consider communication delay to be $\sigma = 0.2$ [s]. Moreover, we assume the desired operating domain

$$\mathcal{D}_h = \{h:\ 15 \le h \le 25\ [\mathrm{m}]\}, \quad \mathcal{D}_v = \{v:\ 0 \le v \le 30\ [\mathrm{m/s}]\}. \tag{3.24}$$

Then, we apply both the linear analysis given in Chapter 2 and the nonlinear analysis presented in this chapter to such network and compare the results.

In particular, we consider the vehicle network in Figure 3.1 with 41 vehicles and design control gains $\alpha_{k,k-m}, \beta_{k,k-m}$ $(m = 2, 3)$ by applying Theorems 8, 10 and 11, in order to exploit the information received via wireless V2V communication. Fixing $\alpha_{k,k-2} = 0$

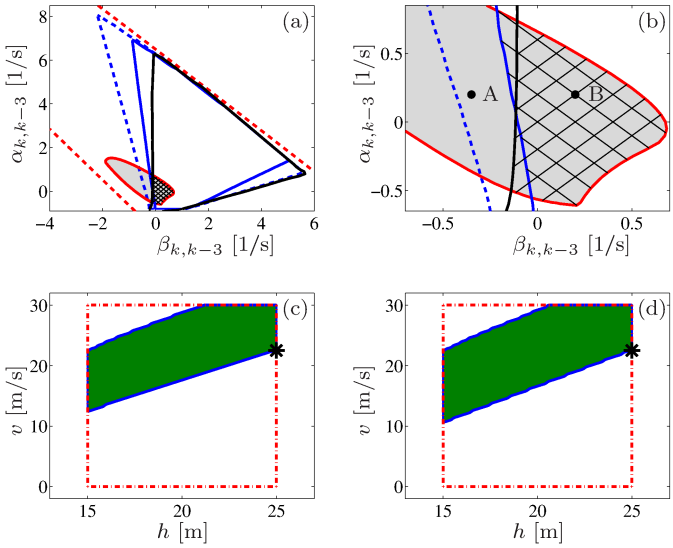

Figure 3.2: (a): Stability diagram in $(\beta_{k,k-3}, \alpha_{k,k-3})$-plane for plant stability and string stability. Gray-shaded, "\"-shaded, and "/"-shaded regions highlight the domains for plant stability, $\mathcal{L}_\infty$-HT string stability, and eventual string stability, respectively. Solid red, solid black, and solid blue curves are obtained by using Theorems 8, 10 and 11, respectively. The dashed red and the dashed blue curves enclose domains for plant stability and string stability that are obtained using the linearized model. (b): A zoomed-in view of panel (a). (c) and (d): Feasible regions (shaded) for cases A and B, respectively. The red dashed-dotted lines bound the operating domain $\mathcal{D}_h \times \mathcal{D}_v$, and the black star denotes the equilibrium.

[1/s] and $\beta_{k,k-2} = 1$ [1/s], we derive conditions for choosing control gains $\alpha_{k,k-3}$, $\beta_{k,k-3}$ and display the results using stability diagrams as shown in Figure 3.2(a) and (b). Here, the control gains inside the gray-shaded domain can ensure plant stability. Besides plant stability, the control gains from the '\'-shaded and the '/'-shaded areas can also ensure $\mathcal{L}_\infty$-HT string stability and eventual string stability, respectively. The solid red curve (enclosing the gray-shaded domain), the solid black curve, and the solid blue curve mark the boundaries resulting from Theorems 8, 10 and 11, respectively. The dashed red and the dashed blue curves are derived by using the linearized model for plant stability and $\mathcal{L}_\infty$-HT string stability, respectively.

To evaluate the effects of the long-range communication on the network performance, we first consider the network without communication as a benchmark, which corresponds to $\alpha_{k,k-2} = \beta_{k,k-2} = \alpha_{k,k-3} = \beta_{k,k-3} = 0$ for all k (see Figure 3.1 without red links). Then, we exploit communication and choose two sets of control gains corresponding to the points marked by A and B in Figure 3.2(b). To test the robustness, we consider an extreme case where the equilibrium is at the boundary of the operating domain (3.24), which is enclosed by the red dashed-dotted curve in Figure 3.2(c) and (d). In particular, we consider

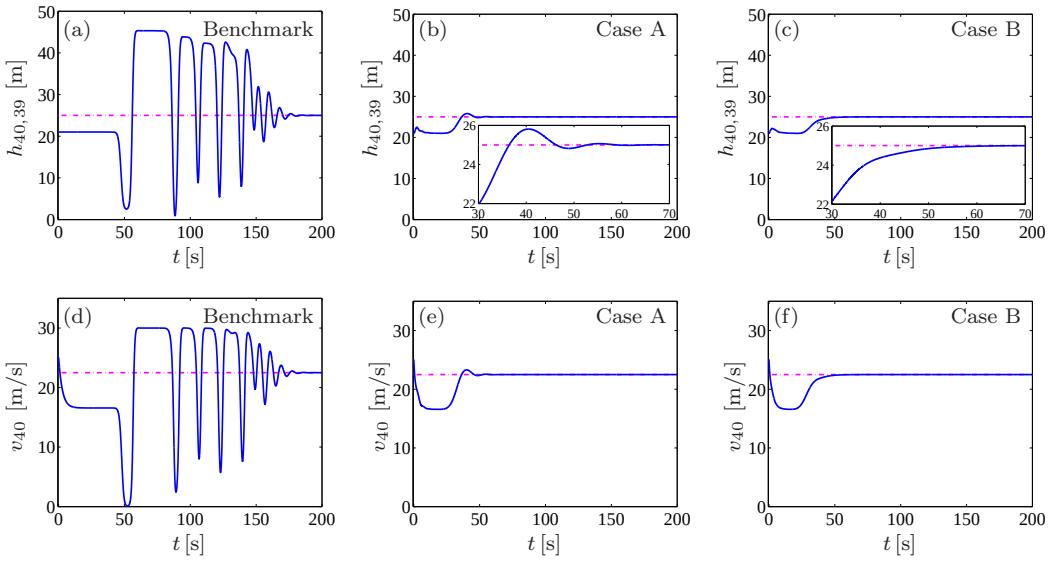

Figure 3.3: Simulations results when the head vehicle 0 moves at a constant speed. The top row shows the distance between vehicles 39 and 40 while the bottom row shows the velocity of vehicle 40, respectively. Dashed-dotted lines indicate the uniform flow equilibrium.

the equilibrium distance $h^* = 25$ [m] that leads to the equilibrium speed $v^* = 22.5$ [m/s]; cf. (2.9) with (2.11). The equilibrium is highlighted by the black star in Figure 3.2(c,d). Assuming constant initial velocities, that is, $v_i(\theta) \equiv v_{i,0}$ and $s_i(\theta) = s_{i,0} + v_{i,0}(\theta + 0.5)$ for $\forall \theta \in [-0.5,\ 0]$, we obtain the feasible regions for cases A and B numerically, as displayed in Figure 3.2(c) and (d), respectively. To simulate plant stability, we let vehicle 0 move at a constant speed $v_0(t) \equiv v^* = 22.5$ [m/s] with initial position $s_{0,0} = 0$ [m]. The initial conditions for the following vehicles are given by $v_{i,0} = 25$ [m/s] and $s_{i,0} = -21i$ [m] for $i = 1, \ldots, 40$. The corresponding simulation results for the benchmark and for the gains marked by points A and B are shown in Figure 3.3, where the top row displays the distance between vehicles 39 and 40, while the bottom row shows the speed of vehicle 40. Although the benchmark can eventually reach the equilibrium, the settling time is long, and there exist undesired transient oscillations that push the state outside the operating domain; see Figure 3.3(a,d). For the gains marked by point A (Figure 3.3(b,e)), such undesired transients are avoided, while there is a small overshoot around $t = 40$ [s] where the distance is outside the operating domain (see the zoomed-in panel in Figure 3.3(b)). The gains corresponding to point B are chosen to ensure both $\mathcal{L}_\infty$-HT string stability and eventual string stability. Now, the plant stability can be achieved without overshoot; see Figure 3.3(c,f). Comparison between cases A and B implies that, although our results for string stability are obtained by analyzing the steady-state response, they may also improve

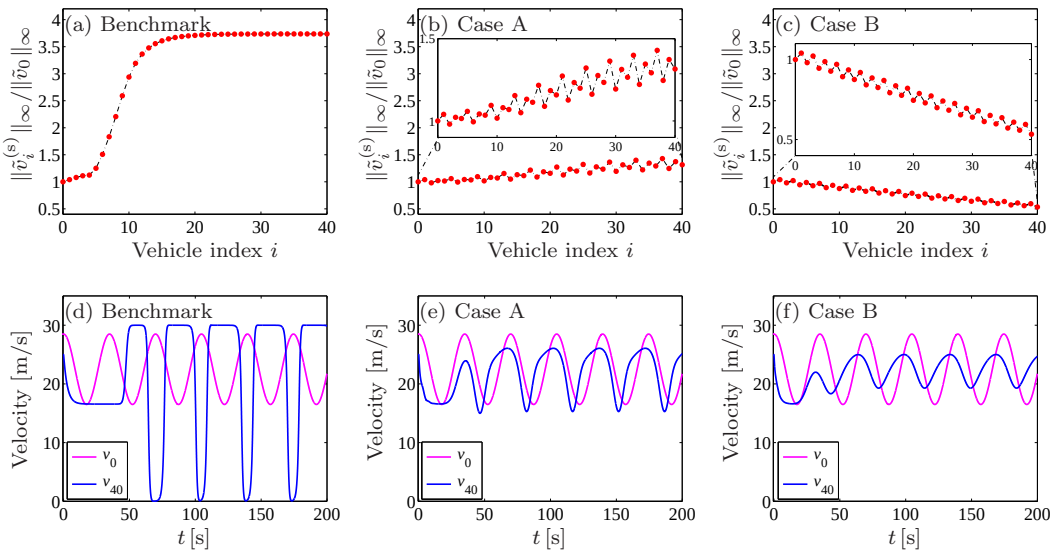

Figure 3.4: Simulation results for disturbance attenuation. In the top row, the red points show the amplification ratios between the perturbation of each following vehicle and that of the head vehicle in terms of $\mathcal{L}_\infty$ norm, while the bottom row displays the velocities of vehicles 0 and 40, respectively.

the transient behavior.

To test disturbance attenuation, we consider a sinusoidal velocity disturbance $v_0(t) = v^* + v_{\text{amp}} \cos(\omega t)$ for vehicle 0, where $v_{\text{amp}} = 6$ [m/s] and $\omega = 0.18$ [rad/s]. Using the same initial conditions as used in Figure 3.3, we conduct simulations for the benchmark and for the gains corresponding to points A and B, respectively. The results are displayed in Figure 3.4, where the top row demonstrates how the disturbance evolves when propagating along the network, while the bottom row shows the velocities of vehicles 0 and 40. In the benchmark, where the communication is not exploited, the disturbance arising from vehicle 0 is amplified when propagating to following vehicles and leads to stop-and-go motion of vehicle 40; see Figure 3.4(a,d). The saturations at $v = 0$ [m/s] and $v = 30$ [m/s] are caused by the saturation of the range policy (2.9) with $v_{\max} = 30$ [m/s]. Figure 3.2(b) shows that point A is inside the region for $\mathcal{L}_\infty$-HT string stability obtained by linear analysis but outside the corresponding regions obtained by nonlinear analysis. Simulation results in Figure 3.4(b,e) demonstrate that the disturbance is indeed amplified as it propagates along the chain. This implies that the results obtained from linearized dynamics may be not valid when perturbations are large. The control gains at point B are chosen inside the region for $\mathcal{L}_\infty$-HT & eventual string stability. Simulations in Figure 3.4(c,f) show that the disturbance is attenuated along the vehicle network although not uniformly since it is amplified by non-CCC vehicles.

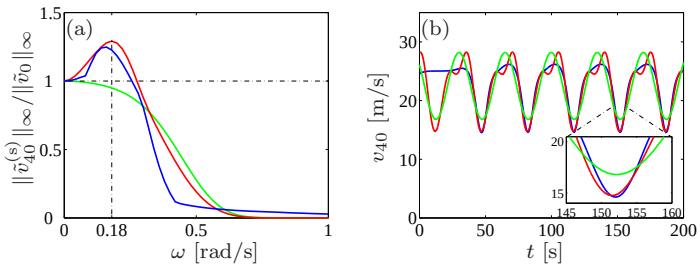

Figure 3.5: Comparison of linear approximation (green) and the nonlinear approximation (red) with the numerical simulation (blue). (a) Amplification ratio curves and (b) velocity of the tail vehicle 40.

For the gains marked by point A, we also investigate the frequency response by comparing the result obtained by linear analysis with that obtained by nonlinear approximation. Figure 3.5(a) displays the amplification ratio curves obtained by linear approximation (green), nonlinear approximation (red), and numerical simulation (blue). It shows that the nonlinear analysis is more accurate than the linear analysis. In particular, the nonlinear analysis reveals the disturbance amplification, which cannot be discovered by the linear analysis. Choosing $\omega = 0.18$ [rad/s], we also compare the approximation and the numerical simulation as shown in Figure 3.5(b), which shows that the nonlinear approximation captures the largest perturbation better and hence characterize the $\mathcal{L}_\infty$-HT string stability; see the zoomed-in inlet in Figure 3.5(b).

3.5 Summary

In this chapter, we investigated the nonlinear time-delayed dynamics of connected vehicle networks that were constructed by exploiting the V2V communication. For plant stability and string stability, we derived conditions that were simple for application and remained scalable for large complex networks. Numerical simulation results validated the analytical conditions and also showed that nonlinear analysis provided more accurate results than the linear analysis.

In Chapters 2 and 3, we presented a general controller for the planning level of CCC, in order to generate the desired car-following dynamics by incorporating the motion data of multiple vehicles ahead received via V2V communication. Effects of information delays, connectivity topologies, and nonlinear dynamics on the performance of the corresponding vehicle networks were investigated. To simplify the design of car-following dynamics, physical effects such as aerodynamic drag and rolling resistance were not taken into account. But these effects may significantly affect the vehicle dynamics. To make CCC

robust in practice, in the next chapter we will design control schemes such that the vehicle state can track the desired car-following dynamics in presence of uncertain parameters and external disturbances.

CHAPTER 4

Execution Level: Adaptive Control for Engine Torque

The objective of the execution level is to control the engine torque and select appropriate gears such that the vehicle state x_i can track the desired state $x_{i\mathrm{d}}$, that is,

$$x_i(t) \to x_{i\mathrm{d}}(t)\,, \quad \text{as } t \to \infty\,, \tag{4.1}$$

cf. Figure 1.2(b). To achieve this objective, we present an Adaptive Sliding-Mode Control (ASMC) scheme that guarantees tracking performance in presence of both uncertain parameters and external disturbances which were not considered in previous works [74,75].

4.1 Controller Design

To design control schemes for engine torque and gear shifts, we consider the physics-based vehicle model given by [50, 58] where the flexibility of tire and suspension is neglected. That is,

$$\dot{x}_i = \begin{bmatrix} \dot{s}_i \\ \dot{v}_i \end{bmatrix} = \begin{bmatrix} v_i \\ -\frac{mg\sin\phi_i}{m_{\mathrm{eff}}} - \frac{rmg\cos\phi_i}{m_{\mathrm{eff}}} - \frac{k(v_i+v_{\mathrm{w},i})^2}{m_{\mathrm{eff}}} + \frac{T_{\mathrm{a},i}}{m_{\mathrm{eff}}R} \end{bmatrix}, \tag{4.2}$$

where the effective mass $m_{\mathrm{eff}} = m + J/R^2$ contains the vehicle mass m, the moment of inertia J of the rotating elements, and the wheel radius R. Moreover, g is the gravitational constant, r is the rolling resistance coefficient, k is the aerodynamic drag constant. The external disturbances include the road angle ϕ_i and the headwind speed $v_{\mathrm{w},i}$. Here, we design the controller for the axle torque $T_{\mathrm{a},i} = \eta_i T_{\mathrm{e},i}$, which is the engine torque $T_{\mathrm{e},i}$ and the constant $\eta_i =$ gear ratio $\times$ final drive ratio; see Appendix B for parameters of a heavy-duty vehicle. We assume that the onboard sensors are able to measure the states sufficiently fast so that the corresponding time delays can be neglected. Thus, we drop the argument t in the states of (4.2) to make expressions more concise.

Then, we design the controller for the axle torque $T_{\mathrm{a},i}$ to achieve the tracking performance (4.1). Multiplying the second equation in (4.2) by $m_{\mathrm{eff}}R$ yields

$$\theta_{i,1}\dot{v}_i = -\theta_{i,2}\sin\phi_i - \theta_{i,3}\cos\phi_i - \theta_{i,4}(v_i + v_{\mathrm{w},i})^2 + T_{\mathrm{a},i}, \tag{4.3}$$

where

$$\theta_{i,1} = m_{\mathrm{eff}}R\,,\ \theta_{i,2} = mgR\,,\ \theta_{i,3} = rmgR\,,\ \theta_{i,4} = kR\,. \tag{4.4}$$

For compactness, we use $\theta_i = [\theta_{i,1},\ \theta_{i,2},\ \theta_{i,3},\ \theta_{i,4}]^{\mathrm{T}}$ that includes all vehicle parameters.

Estimating vehicle parameters

$$\hat{\theta}_i = [\hat{\theta}_{i,1},\ \hat{\theta}_{i,2},\ \hat{\theta}_{i,3},\ \hat{\theta}_{i,4}]^{\mathrm{T}} \tag{4.5}$$

and assuming constant headwind speed $\hat{v}_{\mathrm{w},i}$, one may design the execution-level controller in the form

$$T_{\mathrm{a},i} = \hat{\theta}_{i,1}u_i + \hat{\theta}_{i,2}\sin\phi_i + \hat{\theta}_{i,3}\cos\phi_i + \hat{\theta}_{i,4}(v_i + \hat{v}_{\mathrm{w},i})^2\,, \tag{4.6}$$

where u_i is given by the planning-level controller (2.12) but replacing the desired state $x_{i\mathrm{d}}$ with the real state x_i. Indeed, the controller (4.6) is designed by incorporating the desired dynamics (2.12) while trying to cancel out the nonlinear terms in (4.2) by using feedback signals. When the estimated values of parameters and headwind speed match the real ones, i.e., $\theta_{i,j} = \hat{\theta}_{i,j}$ for $j = 1, \ldots, 4$ and $v_{\mathrm{w},i}(t) \equiv \hat{v}_{\mathrm{w},i}$, the closed-loop dynamics (4.2) and (4.6) becomes the desired dynamics (2.17) so that the objective (4.1) is achieved.

However, in practice vehicle parameters may be not exactly known while the headwind speed varies in time. Hence, the benchmark controller (4.6) may not ensure the required tracking performance. Thus, we seek for controllers that can guarantee tracking performance while remaining robust against uncertainties in parameters and external disturbances. Here, we assume that vehicle parameters and headwind speed are bounded with known bounds. In particular, we denote

$$k \le \overline{k}\,, \quad R \le \overline{R}\,, \quad \underline{v}_{\mathrm{w}} \le v_{\mathrm{w},i} \le \overline{v}_{\mathrm{w}}\,, \tag{4.7}$$

where $\overline{k}$, $\overline{R}$, $\underline{v}_{\mathrm{w}}$, and $\overline{v}_{\mathrm{w}}$ are all constants. Then, it follows that

$$\theta_{i,4} \le \overline{k}\,\overline{R}\,, \tag{4.8}$$

cf. (4.4). We write the headwind speed in the form

$$v_{\mathrm{w},i}(t) = \hat{v}_{\mathrm{w},i} + \tilde{v}_{\mathrm{w},i}(t)\,, \tag{4.9}$$

where the first term denotes the average

$$\hat{v}_{\mathrm{w},i} = \frac{\underline{v}_{\mathrm{w}} + \overline{v}_{\mathrm{w}}}{2}\,, \tag{4.10}$$

while the second terms denotes the uncertainties bounded by

$$|\tilde{v}_{\mathrm{w},i}| \leq \frac{\overline{v}_{\mathrm{w}} - \underline{v}_{\mathrm{w}}}{2}\,. \tag{4.11}$$

Substituting (4.9) into (4.3) yields

$$\theta_{i,1}\dot{v}_i = -\theta_{i,2}\sin\phi_i - \theta_{i,3}\cos\phi_i - \theta_{i,4}(v_i + \hat{v}_{\mathrm{w},i})^2 + \delta(v_i, \tilde{v}_{\mathrm{w},i}) + T_{\mathrm{a},i}\,, \tag{4.12}$$

where the unknown disturbance $\delta(v_i, \tilde{v}_{\mathrm{w},i})$ is given by

$$\delta(v_i, \tilde{v}_{\mathrm{w},i}) = -\theta_{i,4}\big(2\tilde{v}_{\mathrm{w},i}(v_i + \hat{v}_{\mathrm{w},i}) + \tilde{v}_{\mathrm{w},i}^2\big)\,. \tag{4.13}$$

Considering (4.8) and (4.11), one can obtain the upper bound of the unknown disturbance

$$\big|\delta(v_i, \tilde{v}_{\mathrm{w},i})\big| \leq \overline{k}\,\overline{R}\left((\overline{v}_{\mathrm{w}} - \underline{v}_{\mathrm{w}})(v_i + \hat{v}_{\mathrm{w},i}) + \left(\frac{\overline{v}_{\mathrm{w}} - \underline{v}_{\mathrm{w}}}{2}\right)^2\right) \triangleq \overline{\delta}(v_i)\,. \tag{4.14}$$

We assume that the vehicle state x_i and the inclination angle ϕ_i can be obtained via onboard sensors, digital maps, and global positioning system (GPS). To enable the vehicle to track the desired dynamics while counteracting the uncertain vehicle dynamics, one may using the sliding-mode control technique [76]. However, this method may lead to conservative results since it relies on the upper bounds of uncertainties for robustness. Here, we combine the sliding-mode control with the adaptive control approach [77]. In particular, the adaptive control is used to adjust to the uncertain constant parameters and the sliding-mode control is applied to compensate for the uncertain time-varying disturbances. We remark that the combination of these two methods leads to robust tracking while also reducing the conservativeness.

To design the execution-level controller, we first define a sliding surface

$$S_i \triangleq v_i - v_{i\mathrm{d}} + \lambda_1(s_i - s_{i\mathrm{d}}) = 0\,, \tag{4.15}$$

where $s_{i\mathrm{d}}$ and $v_{i\mathrm{d}}$ are the desired states given by the planning level while λ_1 is a positive parameter. Note that tracking errors decay to zero along the sliding surface (4.15), i.e., $s_i(t) \to s_{i\mathrm{d}}(t)$ and $v_i(t) \to v_{i\mathrm{d}}(t)$ as $t \to \infty$. Then, we seek for a controller that regulates

the state to reach the sliding surface (4.15) so that the tracking error decays to zero along the sliding surface. Based on (4.14) and (4.15), we present the controller for the axle torque

$$T_{\mathrm{a},i}(t) = \hat{\theta}_i^{\mathrm{T}} w - \overline{\delta}(v_i)\mathrm{sgn}(S_i) - \lambda_2 S_i \,, \tag{4.16}$$

where the parameter estimate $\hat{\theta}_i$ is given in (4.5), the positive constant λ_2 is a tuning parameter, and the vector w is constructed as

$$w = \begin{bmatrix} w_1 \\ w_2 \\ w_3 \\ w_4 \end{bmatrix} = \begin{bmatrix} \dot{v}_{i\mathrm{d}} - \lambda_1(v_i - v_{i\mathrm{d}}) \\ \sin\phi_i \\ \cos\phi_i \\ (v_i + \hat{v}_{\mathrm{w},i})^2 \end{bmatrix} . \tag{4.17}$$

The adaptation law for the estimate $\hat{\theta}_i$ is given by

$$\dot{\hat{\theta}}_i = -S_i \Gamma w \,, \tag{4.18}$$

where the positive definite matrix $\Gamma \in \mathbb{R}^{4\times 4}$ contains the adaptation gains. In the controller (4.16), the first and the second terms are used to counteract the uncertainties arising from constant parameters and time-varying disturbances, respectively, and the third term is used to regulate the system to the sliding surface (4.15).

Theorem 12 If the modeling uncertainties have known bounds (4.7), the execution-level controller (4.15)–(4.18) ensures that the vehicle dynamics (4.2) tracks the desired motion generated by the planning level in the sense of (4.1).

The proof is given in Appendix A.6. In the controller (4.15)–(4.18), λ_1 determines the decaying speed of tracking errors along the sliding surface $S_i = 0$ while λ_2 determines the speed for approaching the sliding surface. In practice, λ_2 shall be a large number, since the effective gain on the acceleration for the closed-loop system is indeed $\lambda_2/\theta_{i,1}$ and $\theta_{i,1}$ is a large number; cf. (4.4).

In the adaptation law (4.18), we use a diagonal matrix $\Gamma = \mathrm{diag}\{\Gamma_1\,, \Gamma_2\,, \Gamma_3\,, \Gamma_4\}$, where $\Gamma_1\,, \ldots\,, \Gamma_4$ are all positive scalars. Note that the adaptation speed of $\hat{\theta}_{i,k}$ is proportional to $\Gamma_k w_k$ for $k = 1, \ldots, 4$. In practice, the inclination angle ϕ_i is small, yielding $w_2 \approx 0$. In this case, Γ_2 has little influence on the adaptation. Considering that the value of w_4 may be much larger than the values of w_1, w_2, and w_3, one may choose Γ_4 to be a small number. Note that in general the adaptation law (4.18) may not regulate $\hat{\theta}_i$ to approach the actual value θ_i since the excitation becomes weak when the state is around the sliding

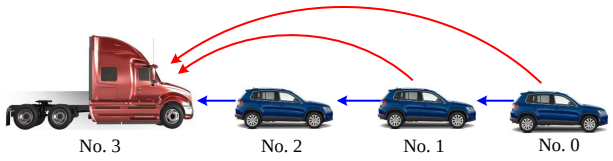

Figure 4.1: A 4-vehicle network where the vehicle 3 is a heavy-duty truck equipped with CCC. The other vehicles are human-driven vehicles that only respond to the vehicle immediately ahead.

surface, i.e., $S_i \approx 0$. However, this does not affect the tracking performance, as will be demonstrated by numerical simulations in Section 4.2

The parameters in the controller (4.15)–(4.18) should be appropriately designed to achieve fast tracking while avoiding transient oscillations. For different problems, the range of feasible parameters may vary. The tuning of these parameters is typically done through analysis and simulation, as will be shown in our case study in Section 4.2

When implementing the controller (4.16), the discontinuities of the term $\mathrm{sgn}(S_i)$ may cause undesired chattering around the sliding surface (4.15). In practice, we replace the term $\mathrm{sgn}(S_i)$ by a continuous saturation function

$$\mathrm{sat}(S_i/\Phi_i) = \begin{cases} S_i/\Phi_i\,, & \text{if } |S_i| \le \Phi_i\,, \\ \mathrm{sgn}(S_i)\,, & \text{otherwise}\,, \end{cases} \tag{4.19}$$

where the positive constant Φ_i defines the boundary layer that is an invariant region around the sliding surface. Note that large values of Φ_i may deteriorate the tracking performance while small values of Φ_i may still lead to chattering phenomenon. Thus, in practice, Φ_i should be chosen by considering the tradeoff between the tracking performance and the chattering avoidance.

4.2 Simulation Results

In this section, we apply the planning-level controller (2.12) and the execution-level controller (4.15)–(4.18) to a heavy-duty vehicle in a 4-vehicle network shown in Figure 4.1. In Figure 4.1, the heavy-duty vehicle 3 is equipped with CCC while human-driven vehicles 0–2 only respond to the motion of the vehicle immediately ahead. We consider that vehicle 3 receives motion data from vehicles 0 and 1 with delays $\xi_{3,0} = \xi_{3,1} = 0.2$ [s], which are caused by intermittency and packet drops in the wireless communication. We also consider the scenario where vehicle 3 is driven by a human driver who monitors the

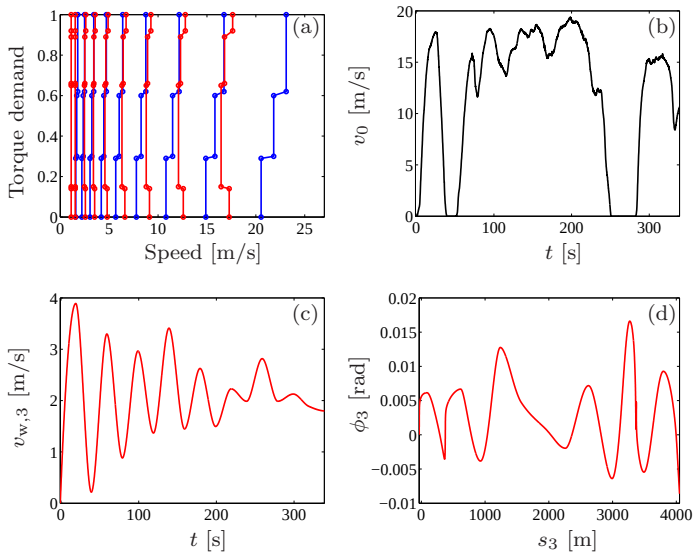

Figure 4.2: (a) Gear shift map for the heavy-duty vehicle, where the blue and the red curves indicate up- and down-shifts, respectively. (b) Velocity profile of vehicle 0. (c,d) Headwind speed and road inclination angle.

motion of vehicle 2 with reaction delay $\xi_{3,2} = 0.5$ [s] while the CCC is used to assist the driver. The parameters of the heavy-duty truck are provided in Appendix B while the gear shift map is shown in Figure 4.2(a), where the blue and the red curves represent the upshift and the downshift, respectively; see [54, 78].

We assume that the head vehicle 0 has length $l_0 = 4.8$ [m] while its velocity is given by the experimental data of UMTRI Safety Pilot Project [79] where the speed is measured every 0.1 [s], as shown in Figure 4.2(b). Moreover, we assume the car-following dynamics of vehicles $j = 1, 2$ are given by (2.8). The parameters of vehicles $j = 1, 2$ are set as follows.

- $l_1 = 4.5$ [m], $\alpha_{1,0} = 0.5$ [1/s], $\beta_{1,0} = 0.7$ [1/s], $h_{\mathrm{st},1} = 3$ [m], $h_{\mathrm{go},1} = 40$ [m], $v_{\max,1} = 30$ [m/s], and $\xi_{1,0} = 0.8$ [s].
- $l_2 = 4$ [m], $\alpha_{2,1} = 0.3$ [1/s], $\beta_{2,1} = 0.6$ [1/s], $h_{\mathrm{st},2} = 4$ [m], $h_{\mathrm{go},2} = 38$ [m], $v_{\max,2} = 32$ [m/s], and $\xi_{2,1} = 0.6$ [s].

For vehicle 3, we assume that the parameters in range policy (2.9) are $h_{\mathrm{st},3} = 5$ [m], $h_{\mathrm{go},3} = 35$ [m], and $v_{\max,3} = 30$ [m/s]. For the headwind speed, we assume that it can be modeled by autoregressive moving average model [80]. In particular, we use

$$v_{\mathrm{w},3}(t_k) + c_1 v_{\mathrm{w},3}(t_{k-1}) = \rho + \epsilon(t_k) + e_1 \epsilon(t_{k-1}) \,, \tag{4.20}$$

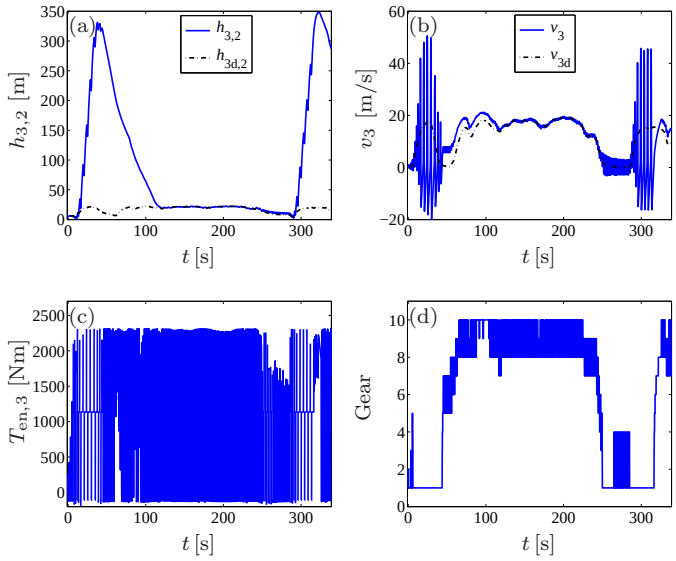

Figure 4.3: Simulation for the benchmark when using controller (4.6) at the execution level. (a,b) Distance $h_{3,2}$ and velocity v_3 of vehicle 3. (c,d) Engine torque $T_{\text{en},3}$ and gear shifts of vehicle 3.

where $t_k = t_{k-1} + 20$ [s] for $k = 1, 2, \ldots$, and c_1, ρ, e_1 are constants while ϵ is a random variable between 0 and 1. Here, we use $c_1 = 0.9$, $\rho = 3$ [m/s], and $e_1 = 0.8$ [m/s]. For the road angle, we assume that its model is also in the form of (4.20) but replacing $v_{\text{w},3}(t_k)$ by $\phi_3(t_k)$. The corresponding parameters are set to be $c_1 = 0.3$, $\rho = 0$ [deg], and $e_1 = -0.6$ [deg]. Then, we interpolate the discrete data of the headwind and the road angle by using the step size 0.1 [s], leading to the trajectories as displayed in Figure 4.2(c,d), respectively.

For vehicle 3, the desired car-following dynamics is given by (2.17). To satisfy Theorem 8 for plant stability, we choose the control gains to be $\alpha_{3,2} = 0.3$ [1/s], $\beta_{3,2} = 0.5$ [1/s], $\alpha_{3,1} = 0$ [1/s], $\beta_{3,1} = 1$ [1/s], $\alpha_{3,0} = 0.2$ [1/s], and $\beta_{3,0} = 0.2$ [1/s]. For the execution-level controller, we first use the controller (4.6) as the benchmark. When the estimated parameter values and headwind speed exactly match their real values, the benchmark controller leads to $s_3(t) = s_{3\text{d}}(t)$ and $v_3(t) = v_{3\text{d}}(t)$ for all $t > 0$. Here, we consider estimated values $\hat{m} = 30000$ [kg], $\hat{k} = 7.7$ [kg/m], $\hat{r} = 0.01$, and $\hat{R} = 0.6$ [m], which are different from the actual values given in Appendix B. The corresponding simulation results are shown in Figure 4.3. The trajectories displayed in Figure 4.3(a,b) show that the vehicle state (solid blue) cannot track the desired state (dashed-dotted black) generated at the planning level. Moreover, the benchmark controller leads to fast oscillations in the engine torque and gear shifts, as displayed in Figure 4.3(c,d). This may cause severe damage to the engine and the transmission.

Then we apply the ASMC scheme (4.15)–(4.18) at the execution level. In order to find

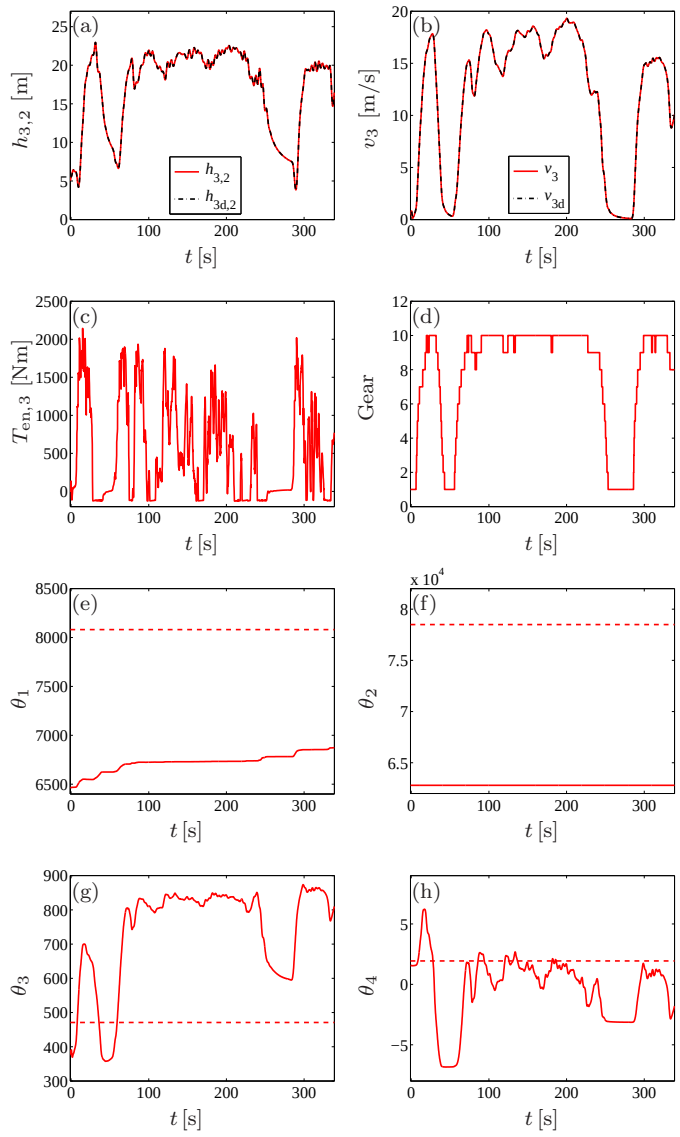

Figure 4.4: Simulation for the case when applying the adaptive sliding mode controller at the execution level. (a,b) Distance $h_{3,2}$ and velocity v_3 of vehicle 3. (c,d) Engine torque $T_{\mathrm{en},3}$ and gear shifts of vehicle 3. (e)–(h) Real vehicle parameters (dashed lines) and their estimates (solid curves).

feasible parameters to achieve fast tracking and avoid transient oscillations, we conducted a large number of simulations. Here, we summarize the range of feasible parameters as follows. The values of λ_1 and λ_2 can be selected in the ranges 0.1–10 and 10^4–10^5, respectively. The adaptation gains Γ_1 and Γ_3 should be selected in the range 10^2–10^3 while Γ_4 can be chosen between 0.1 and 1. Since Γ_2 has little impact on the parameter adaption, one can simply choose a value between 0 and 1. Here, we set the values to be $\lambda_1 = 1$ [1/s] and $\lambda_2 = 3 \times 10^4$ [kg·m/s] while the adaptation gains are given by Γ=diag$\{100, 1, 500, 0.1\}$

with units [kg·s/m], [N], [N], [kg·s^2/m^3], respectively. Moreover, the boundary layer in (4.19) is set to be $\Phi = 0.1$ [m/s]. The corresponding simulation results are displayed in Figure 4.4. As shown in Figure 4.4(a,b), the vehicle state (solid red) tracks the desired state (dashed-dotted black) generated at the planning level. Figure 4.4(c,d) show the engine torque and the gear shifts with no fast oscillations. Moreover, Figure 4.4(c) implies that the demanded torque is in a realistic range without always requiring the maximum torque 2314.3 [N·m]; see Appendix B. However, this is affected by many effects such as the motion of the preceding vehicles, road angle, and headwind speed, and thus, it may not be guaranteed in general cases. Comparing Figure 4.4(c) and Figure 4.3(c) also shows the advantage of the adaptive sliding-mode controller in leading to realistic torque inputs. Figure 4.4(e)–(h) show that the parameter estimates do not converge to the real value, but this does not affect the state tracking performance as shown in Figure 4.4(a) and (b).

In summary, comparing the simulation result for benchmark controller (blue curves in Figure 4.3(a)–(d)) and that for adaptive sliding mode controller (red curves in Figure 4.4(a)–(d)), one can observe that the latter one can regulate the vehicle to track the desired state while counteracting uncertainties in vehicle dynamics. When the planning level is designed for minimizing fuel consumption or for avoiding collisions, large deviations from the desired state may increase fuel consumption or lead to collision. In this sense, the adaptive sliding mode controller leads to better performance than the benchmark controller. Moreover, the adaptive sliding mode controller improves the actuator performance by avoiding fast oscillations.

4.3 Summary

In this chapter, we designed the execution-level controller by applying the adaptive sliding-model control approach, which regulates the engine torque and selects appropriate gears so that the state of the CCC vehicle can track the desired car-following dynamics generated at the planning level in presence of uncertain vehicle dynamics. Physical effects such as road angle, aerodynamic drag, and rolling resistance were taken into account. Numerical simulations were used to validate the analytical results and to show the advantage of the presented controller in robustly tracking states and avoiding transient oscillations.

CHAPTER 5

Perception Level: Beyond-Line-of-Sight Perception

In this chapter, we investigate the beyond-line-of-sight (BLOS) perception of CCC vehicles by utilizing the motion data received from distant vehicles via wireless V2V communication. To appropriately incorporate the received information into vehicle control systems, the CCC vehicle shall be able to determine whether the motion of broadcasting vehicles are relevant to its own motion. Moreover, to achieve system-level performance such as string stability and collision avoidance, the CCC vehicle needs to know the dynamics of surrounding vehicles, which is not available in real traffic. To address these issues, in this chapter we first present a *causality detector* that can determine whether the received information is relevant to the CCC vehicle. Then, we propose the *link-length estimator* and the *network-dynamics identifier* to identify the dynamics of the vehicle network.

5.1 Causality Detector

In this section, we propose a causality detector that determines whether the information received from a distant vehicle is relevant to the motion of the CCC vehicle. In particular, we focus on single-lane scenarios and assume that the CCC vehicle monitors the motion of the vehicle immediately ahead by using range sensors and also receives information from a distant vehicle via V2V communication. The key idea is that, if the motion of the broadcasting vehicle influences the motion of the vehicle immediately ahead, then the information of this broadcasting vehicle is considered to be relevant for the CCC vehicle.

As recorded during the UMTRI Safety Pilot Project [79], V2V communication provides motion data of vehicles every $\delta t = 0.1$ [s]. To make the subsequent expressions more compact, we define the time instant $t_k = k \cdot \delta t$ and also define the vector of motion data in

the form

$$\begin{aligned} \mathbf{s}_j(t_k) &= \left[s_j(t_{k-\Delta}),\, s_j(t_{k-\Delta+1}),\, \ldots,\, s_j(t_k)\right], \\ \mathbf{v}_j(t_k) &= \left[v_j(t_{k-\Delta}),\, v_j(t_{k-\Delta+1}),\, \ldots,\, v_j(t_k)\right], \end{aligned} \tag{5.1}$$

where the positive constant Δ represents the window size for data storage. Larger Δ means more data, which can enhance the robustness of BLOS perception but may also reduce the sensitivity to the change of situations. Thus, the value of Δ must be chosen by considering the tradeoff between robustness and sensitivity. Feasible values for Δ will be discussed in Section 5.4 based on numerical simulations.

To appropriately use the information received via V2V communication, it is important to detect whether the received information is relevant to the motion of the CCC vehicle. To determine such relevance, we propose a causality detector in this section. The motion of two vehicles are said to have a causal relationship if the motion of one vehicle influences the motion of the other vehicle. For example, consider the vehicle chain in Fig. 2.1. If there is a causal relation between the motion of vehicles p and i, the speed perturbation of vehicle p will lead to a speed perturbation of vehicle i since perturbations propagate along the chain of vehicles. Otherwise, vehicle i may not respond to the motion of vehicle p. Such non-causality occurs when there are no vehicles between vehicles $i-1$ and p while they maintain a large distance.

We evaluate the causality by using the lag phase, which we define as the time difference between similar motions of two vehicles. In practice, the lag phase may vary in time, but the possible values shall be in a bounded range when the number of vehicles between the broadcasting vehicle and the receiving vehicle is bounded. For implementation, we consider a set for values of lag phases

$$\mathcal{D}_\tau = \{\tau_1,\, \tau_2,\, \ldots,\, \tau_N\}, \tag{5.2}$$

where $\tau_\ell = \ell \cdot \delta\tau$ for $\ell = 1, 2, \ldots, N$. Here, we set the distribution size as $\delta\tau = \delta t = 0.1$ [s]. To construct the causality detector, we define the weights corresponding to the lag phase $\tau_\ell \in \mathcal{D}_\tau$ between vehicles i and j at time t_k as

$$w^{(t_k)}(\tau_\ell) = \frac{1}{\|\tilde{\mathbf{v}}_i(t_k) - \tilde{\mathbf{v}}_j(t_k - \tau_\ell)\|_2}, \tag{5.3}$$

for $\ell = 1, \ldots, N$, where

$$\tilde{\mathbf{v}}(t) = \mathbf{v}(t) \,/\, \|\mathbf{v}(t)\|_\infty \tag{5.4}$$

denotes the normalized signal such that all elements in the set $\tilde{\mathbf{v}}(t)$ are between 0 and 1;

cf. (5.1). The norms used in (5.3) and (5.4) are given by

$$\begin{aligned} \|\mathbf{v}_j(t_k)\|_2 &= \sqrt{\sum\nolimits_{m=k-\Delta}^{k} v_j^2(t_m)}\,, \\ \|\mathbf{v}_j(t_k)\|_\infty &= \max_{m=k-\Delta,\ldots,k} |v_j(t_m)|\,, \end{aligned} \tag{5.5}$$

cf. (5.1). Then, we normalize the weights given by (5.3)

$$\tilde{w}^{(t_k)}(\tau_\ell) = \frac{w^{(t_k)}(\tau_\ell)}{\sum_{\ell=1}^{N} w^{(t_k)}(\tau_\ell)}\,, \tag{5.6}$$

which yields $\sum_{\ell=1}^{N} \tilde{w}^{(t_k)}(\tau_\ell) = 1$.

When there is causal relationship between the motion of two vehicles, the distribution (5.6) becomes more concentrated; see Fig. 5.1. If the maximum value of the normalized weights (5.6) is larger than a given confidence threshold (denoted by the dashed-dotted line in Fig. 5.1), the element in (5.2) associated with the maximum weight is chosen to be the estimate of lag phase $\hat{\tau}(t_k)$; see Fig. 5.1(a). Otherwise, it implies lack of confidence for causality between the motion of two vehicles; see Fig. 5.1(b). We remark that when the motion of two vehicles are non-causal, the weights will be uniformly distributed. For instance, this happens when one vehicle moves with constant speed while the speed of the other vehicle varies. On the other hand, if the motion of one vehicle is exactly a time-shifted copy of the motion of the other vehicle, the weight of the corresponding lag phase will be one while the other weights are zeros. For periodic motions, there may exist multiple elements in (5.2) that have the same weight. In this case, we use the smallest element as the estimated lag phase.

Note that the normalized weight (5.6) alone is not sufficient to evaluate the causality between the motion of two vehicles, because it is determined by only the instantaneous motion that may vary significantly at each time step. To enhance the confidence of the causality detection, we construct a distribution by using current and historical data. In particular, we define

$$P^{(t_k)}(\tau_\ell) = \frac{Q^{(t_k)}(\tau_\ell)}{\sum_{m=1}^{N} Q^{(t_k)}(\tau_m)} \tag{5.7}$$

through the distributions

$$Q^{(t_k)}(\tau_\ell) = Q^{(t_{k-1})}(\tau_\ell) + \gamma \lambda^{(t_k)} \tilde{w}^{(t_k)}(\tau_\ell)\,, \tag{5.8}$$

for $\ell = 1, \ldots, N$; cf. (5.2). Here, the positive constant γ determines the update rate and

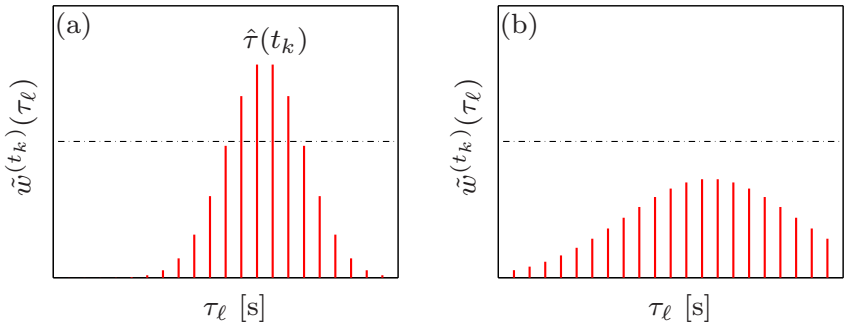

Figure 5.1: Normalized weight $\tilde{w}^{(t_k)}(\tau_\ell)$ for lag phase τ_ℓ at time t_k. The dashed-dotted line denotes the confidence threshold. (a) If the maximum weight is larger then the confidence threshold, the lag phase associated with the maximum weight estimates the most likely $\hat{\tau}(t_k)$. (b) If the maximum weight is smaller than the confidence threshold, it implies lack of causality between the motion of two vehicles.

$\lambda^{(t_k)}$ is given by the Kullback-Leibler divergence (KL-divergence) [81]

$$\lambda^{(t_k)} = \sum_{m=1}^{N} P^{(t_{k-1})}(\tau_m) \log \frac{P^{(t_{k-1})}(\tau_m)}{\tilde{w}^{(t_k)}(\tau_m)}\,, \tag{5.9}$$

which measures the difference between the two distributions $P^{(t_{k-1})}(\tau_\ell)$ and $\tilde{w}^{(t_k)}(\tau_\ell)$. The KL-divergence has the following properties:

- It is non-negative, and it is zero if and only if the two distributions are the same.
- It increase when the difference between the two distributions increases.

According to (5.7)–(5.9), the distribution $P^{(t_k)}(\tau_\ell)$ changes significantly compared with $P^{(t_{k-1})}(\tau_\ell)$ only when there is a large difference between $P^{(t_{k-1})}(\tau_\ell)$ and $\tilde{w}^{(t_k)}(\tau_\ell)$. As initial condition, we use the uniform distribution

$$P^{(t_0)}(\tau_\ell) = Q^{(t_0)}(\tau_\ell) = \frac{1}{N}\,, \tag{5.10}$$

for $\ell = 1, \ldots, N$.

To quantify how concentrated the distribution (5.7) is, we use the concentration function

$$C(t_k) = 1 - \frac{\min_{\tau_\ell} P^{(t_k)}(\tau_\ell)}{\max_{\tau_\ell} P^{(t_k)}(\tau_\ell)}\,. \tag{5.11}$$

Large $C(t_k)$ indicates high possibilities of causality between the motion of the two vehicles.

Setting a confidence threshold $0 < \overline{C} < 1$, we define the causality indicator

$$R_{i,j}(t_k) = \begin{cases} 1\,, & \text{if } C(t_k) > \overline{C}\,, \\ 0\,, & \text{otherwise}\,. \end{cases} \tag{5.12}$$

In practice, the causality between the motion of two vehicles may change due to the lane-change maneuvers. To enhance the sensitivity for detecting such changes, we propose the discrepancy function

$$S(t_k) = -\log\left(\frac{P^{(t_{k-1})}(\hat{\tau}(t_k))}{\max_{\ell=1,\dots,N} P^{(t_{k-1})}(\tau_\ell)}\right), \tag{5.13}$$

which quantifies the difference between the current lag phase $\hat{\tau}(t_k)$ (given by the maximum of the distribution $\tilde{w}^{(t_k)}(\tau_\ell)$) and most possible lag phase given by the distribution $P^{(t_{k-1})}(\tau_\ell)$. Large $S(t_k)$ implies that the current estimate disagrees with the historical data, and thus, the causal relation may have changed. Note that $S(t_k)$ decreases when $P^{(t_{k-1})}(\hat{\tau}(t_k))$ increases. In particular, if $\hat{\tau}(t_k)$ is equal to the most possible value given by the distribution $P^{(t_{k-1})}(\tau_\ell)$, we have $P^{(t_{k-1})}(\hat{\tau}(t_k)) = \max_{\ell=1,\dots,N} P^{(t_{k-1})}(\tau_\ell)$, leading to $S(t_k) = 0$.

5.2 Link-Length Estimator

In connected vehicle networks, to appropriately incorporate the motion data received from distant vehicles into CCC, one needs to know the number of vehicles between the broadcasting vehicle and the CCC vehicle. However, in practice such information is not available, especially when there exist vehicles that do not broadcast information. In this section, we present an estimator to identify the number of vehicles between the broadcasting vehicle and the CCC vehicle by using only the position and the velocity data obtained from V2V communication and range sensors.

To make the subsequent expressions more compact, we use the phrase *link length* to represent the number of vehicles between two vehicles. That is, the link length $n_{i,j}$ between vehicles i and j is given by

$$n_{i,j} = i - j\,. \tag{5.14}$$

The empirical traffic data in [59] show that, when vehicle j moves at a constant speed v_j^*, it aims to keep a desired speed-dependent headway $h_{j,j-1}^*$ from vehicle $j-1$. This

relationship is called a *range policy* and can be described by

$$h^*_{j,j-1} = H_j(v^*_j)\,, \tag{5.15}$$

where the strictly positive function $H_j(v)$ increases with v over the operating domain $0 < v < v_{\max}$. Here, the admissible maximum speed $v_{\max}$ may be determined by the speed limit or by the drivers' decision. When all vehicles move at the same constant speed and they have the identical range policy, i.e., $v^*_j = v^*$ and $H_j(v) = H(v)$ for all j-s, it leads to the *uniform flow equilibrium*

$$h^*_{i,j} = \frac{s^*_j - s^*_i - \sum_{k=j}^{i-1} l_k}{n_{i,j}} = H(v^*)\,, \tag{5.16}$$

cf. (2.15), (5.14), and (5.15). In real traffic, range policies may vary among different vehicles such that the equilibrium still exists but is not uniform, i.e., $v^*_j = v^*_k = v^*$ but $h^*_{j,j-1} \neq h^*_{k,k-1}$ for $j \neq k$. In this situation, the relationship (5.16) can be written in an average form

$$h^*_{i,j} = \frac{s^*_j - s^*_i - n_{i,j} l_{\rm av}}{n_{i,j}} = H_{\rm av}(v^*)\,, \tag{5.17}$$

where the average vehicle length $l_{\rm av}$ and the average range policy $H_{\rm av}(v^*)$ are given by

$$l_{\rm av} = \frac{1}{n_{i,j}} \sum_{k=j}^{i-1} l_k\,, \quad H_{\rm av}(v^*) = \frac{1}{n_{i,j}} \sum_{k=j+1}^{i} H_k(v^*)\,. \tag{5.18}$$

Notice that the length of vehicle i and the range policy of vehicle j are not included in (5.18); cf. (2.15) and (5.15).

If all vehicles broadcast information, the average quantities in (5.18) may be directly obtained, and hence the link length can be computed from (5.17), yielding

$$n_{i,j} = \frac{s^*_j - s^*_i}{l_{\rm av} + H_{\rm av}(v^*)}\,. \tag{5.19}$$

However, in practice, the average quantities in (5.18) are not available when there exist vehicles that do not broadcast information. Thus, in practice, we use the approximations

$$\bar{l}_{\rm av} \approx l_{\rm av}\,, \quad \overline{H}_{\rm av}(v^*) \approx H_{\rm av}(v^*)\,, \tag{5.20}$$

which may be obtained by statistical analysis of empirical traffic data.

In real traffic, vehicles may not move at constant velocity and the distance between two

vehicles varies in time. Considering the constant component in the Fourier series as the equilibrium, one can obtain the equilibrium by using the averages

$$\begin{aligned}
\xi_1(t_k) &\triangleq \mathbb{E}_{t_0}^{t_k}\big[s_j(t_q) - s_i(t_q)\big]\,,\\
\xi_2(t_k) &\triangleq \mathbb{E}_{t_0}^{t_k}\big[\eta v_j(t_q) + (1-\eta)v_i(t_q)\big]\,,\\
\xi_3(t_k) &\triangleq \mathbb{E}_{t_0}^{t_k}\left[\frac{\xi_1(t_q)}{\bar{l}_{\rm av} + \overline{H}_{\rm av}\big(\xi_2(t_q)\big)}\right]
\end{aligned} \tag{5.21}$$

for the distance, velocity, and link length, respectively, where $0 \le \eta \le 1$ is a constant and the averaging operator is defined by

$$\mathbb{E}_{t_0}^{t_k}\big[x(t_q)\big] = \frac{1}{k+1}\sum_{q=0}^{k} x(t_q)\,. \tag{5.22}$$

When the perturbations about the equilibrium have zero means, it follows that

$$\begin{aligned}
\xi_1(t_k) &\to s_j^* - s_i^*\,,\\
\xi_2(t_k) &\to v^*\,,\\
\xi_3(t_k) &\to \frac{s_j^* - s_i^*}{\bar{l}_{\rm av} + \overline{H}_{\rm av}(v^*)}\,,
\end{aligned} \tag{5.23}$$

as $k \to \infty$; cf. (5.19).

Rewriting (5.21) in the iterative form and defining $\hat{n}_{i,j}(t_k)$ as the output, we present the link length estimator

$$\begin{aligned}
\xi_1(t_k) &= \xi_1(t_{k-1}) + \frac{s_j(t_k) - s_i(t_k) - \xi_1(t_{k-1})}{k}\,,\\
\xi_2(t_k) &= \xi_2(t_{k-1}) + \frac{\eta v_j(t_k) + (1-\eta)v_i(t_k) - \xi_2(t_{k-1})}{k}\,,\\
\xi_3(t_k) &= \xi_3(t_{k-1}) + \frac{1}{k}\Big(\frac{\xi_1(t_k)}{\bar{l}_{\rm av} + \overline{H}_{\rm av}\big(\xi_2(t_k)\big)} - \xi_3(t_{k-1})\Big)\,,\\
\hat{n}_{i,j}(t_k) &= \mathrm{int}\big(\xi_3(t_k)\big)\,,
\end{aligned} \tag{5.24}$$

for $k = 1, 2, \ldots$, where $\mathrm{int}(\xi)$ rounds ξ to the nearest integer since the link length must be an integer. Here, the initial condition is set to be $\xi_1(t_0) = \xi_2(t_0) = \xi_3(t_0) = 0$.

Theorem 13 Suppose that the measurement errors in position s and velocity v have zero means. Then, the output of the link length estimator (5.24) converges to the actual link

length, i.e., $\hat{n}_{i,j}(t_k) \to n_{i,j}$ as $k \to \infty$, if and only if the following condition holds:

$$1 - \frac{1}{2n_{i,j}} < \frac{l_{\rm av} + H_{\rm av}(v^*)}{\bar{l}_{\rm av} + \overline{H}_{\rm av}(v^*)} < 1 + \frac{1}{2n_{i,j}}\,. \tag{5.25}$$

The proof is given in Appendix A.7. Theorem 13 implies that, as the link length $n_{i,j}$ increases, the convergence requires higher accuracy of the approximated quantities $\bar{l}_{\rm av}$ and $\overline{H}_{\rm av}(v^*)$. The accuracy of these approximations can be improved when more vehicles in the network broadcast information. However, we remark that the link length estimator (5.24) does not rely on the motion data of vehicles $j+1,\dots,i-1$ so that the estimator can be also applied when they do not broadcast.

The link length estimator (5.24) treats all history data equally, which may reduce the sensitivity of the estimator to the changing number of vehicles caused by the lane-changing behaviors of vehicles. To deal with this problem, we modify (5.24) by using a forgetting factor μ. This leads to the weighted link length estimator

$$\begin{aligned}
\Omega(t_k) &= 1 + \mu\Omega(t_{k-1})\,,\\
\xi_1(t_k) &= \xi_1(t_{k-1}) + \frac{s_j(t_k) - s_i(t_k) - \xi_1(t_{k-1})}{\Omega(t_k)}\,,\\
\xi_2(t_k) &= \xi_2(t_{k-1}) + \frac{\eta v_j(t_k) + (1-\eta)v_i(t_k) - \xi_2(t_{k-1})}{\Omega(t_k)}\,,\\
\xi_3(t_k) &= \xi_3(t_{k-1}) + \frac{1}{\Omega(t_k)}\Big(\frac{\xi_1(t_k)}{\bar{l}_{\rm av} + \overline{H}_{\rm av}\big(\xi_2(t_k)\big)} - \xi_3(t_{k-1})\Big)\,,\\
\hat{n}_{i,j}(t_k) &= \mathrm{int}\big(\xi_3(t_k)\big)\,.
\end{aligned} \tag{5.26}$$

Here, the forgetting factor μ decreases the influence of history data on the current estimation, which enhances the sensitivity. When $\mu = 1$, the weighted link-length estimator (5.26) is reduced to normal link-length estimator (5.24). Note that small values of μ may cause oscillation and hence cannot lead to convergence. In practice, the value of μ should be chosen by considering the trade-off between the robustness and the sensitivity. The feasible values for choosing μ will be investigated in Section 5.4 based on numerical simulations.

5.3 Network-Dynamics Identifier

Consider the vehicle network shown in Figure 2.1. To design CCC for vehicle i to achieve certain system-level performance such as string stability and collision avoidance, it is necessary to know the dynamics of the vehicle network comprised of vehicles $p,\dots,i-1$; see Chapters 2 and 3. Such information cannot be directly obtained in real traffic. In this sec-

tion, we present a network-dynamics identifier to approximate the nonlinear time-delayed dynamics of connected vehicle networks.

In particular, we consider the speed v_p and v_{i-1} as the input and the output of the vehicle network, since the speed perturbation of vehicle p propagates through the whole network and eventually affects the speed of vehicle $i-1$. Although a nonlinear model can improve the estimation accuracy, it will also increase the complexity for the subsequent control design. Thus, we approximate the nonlinear time-delayed dynamics by using the linear discrete-time model

$$\hat{v}_{i-1}(t_k) = \sum_{q=1}^{N} -a_q \hat{v}_{i-1}(t_{k-q}) + b_q v_p(t_{k-q}) = \begin{bmatrix} -\theta_a \\ \theta_b \end{bmatrix}^{\mathrm{T}} \begin{bmatrix} \phi_a \\ \phi_b \end{bmatrix}, \tag{5.27}$$

where the coefficients and the regressors are given by

$$\theta_a = \begin{bmatrix} a_1 \\ \vdots \\ a_N \end{bmatrix}, \quad \theta_b = \begin{bmatrix} b_1 \\ \vdots \\ b_N \end{bmatrix}, \quad \phi_a = \begin{bmatrix} \hat{v}_{i-1}(t_{k-1}) \\ \vdots \\ \hat{v}_{i-1}(t_{k-N}) \end{bmatrix}, \quad \phi_b = \begin{bmatrix} v_p(t_{k-1}) \\ \vdots \\ v_p(t_{k-N}) \end{bmatrix}, \tag{5.28}$$

respectively. Note that the ϕ_a is comprised of estimated states and ϕ_b is constructed by using measured states, while the coefficient vectors θ_a, θ_b and the regression length N are to be determined.

We assume that the car-following dynamics of each vehicle can be modeled by a second-order system. Hence, for a n-vehicle network, we set the regression length as $N = 2n$. Since n is typically unknown in practice, we set $N = 2\hat{n}$ where $\hat{n}$ is the estimated number of vehicles in the network given by the link-length estimator (5.24) or (5.26). In practice, the order of the car-following dynamics of a vehicle may be higher than two due to the information delays. The corresponding modeling mismatches will be minimized by designing the coefficients a_q, b_q in (5.27).

We define the cost function

$$J(\theta_a, \theta_b) = \frac{1}{\Delta + 1} \|\mathbf{v}_{i-1}(t_k) - \hat{\mathbf{v}}_{i-1}(t_k)\|_2 + c_1 \|\mathbf{v}_{i-1}(t_k) - \hat{\mathbf{v}}_{i-1}(t_k)\|_\infty + c_2 \|\theta_b\|_2 , \tag{5.29}$$

where $\Delta + 1$ is the number of elements in the vector $\mathbf{v}_{i-1}(t_k)$ and c_1, c_2 are positive constants. Here, the vectors $\mathbf{v}_{i-1}(t_k)$ and $\hat{\mathbf{v}}_{i-1}(t_k)$ are defined according to (5.1) while the 2-norm and ∞-norm are given in (5.5). The first term in (5.29) is used to evaluate the integral tracking error, the second term is for the peak of tracking error, while the third term is used to control the coefficient values to avoid over-fitting. Note that $J(\theta_a, \theta_b)$ explicitly

depends on θ_b through the the third term and also inexplicitly depends on θ_a and θ_b through $\hat{\mathbf{v}}_{i-1}(t_k)$; cf. (5.27).

Then, the coefficients can be obtained by solving the constrained optimization problem

$$\begin{aligned} &\underset{\theta_a,\,\theta_b}{\text{minimize}} \quad J(\theta_a,\,\theta_b)\,, \\ &\text{subject to} \quad \left\{ |\lambda| < 1 : \lambda^N + \sum_{q=1}^{N} a_q \lambda^{N-q} = 0 \right\}, \end{aligned} \tag{5.30}$$

where the constraint explicitly takes into account the stability of the model (5.27) by requiring all the roots inside the unit circle in the complex plane. The optimization problem (5.30) is challenging, since λ-s are complex numbers and the constraint may lead to disconnected regions for coefficients $a_1, \ldots, a_N$. Now we propose a method that finds suboptimal solutions for the problem (5.30) in an efficient way. We first generate a candidate pool of coefficients $a_1, \ldots, a_N$ that satisfy the stability constraint, and then minimize the cost function $J(\theta_a,\,\theta_b)$ based on the candidate pool. The process will be described in detail in the rest of this section.

The characteristic equation in the constraint of (5.30) can be written in the form

$$\prod_{i=1}^{N} (\lambda + \lambda_i) = 0\,, \tag{5.31}$$

that is, the corresponding roots are given by $-\lambda_i$ for $i = 1, \ldots, N$. To ensure the constraint of (5.30), one needs to guarantee $|\lambda_i| < 1$ for $i = 1, \ldots, N$. To begin with, we randomly sample N numbers inside the unit circle in the complex plane. Since $a_1, \ldots, a_N$ are all real numbers, complex roots must appear in a conjugate way while the real roots shall be mutually independent. To realize this, we begin by randomly sampling $N/2$ values $\lambda_1,\, \ldots,\, \lambda_{N/2}$. If λ_i is a real number, then we randomly sample $-1 < \lambda_{i+N/2} < 1$; otherwise, set $\lambda_{i+N/2} = \lambda_i^*$ where the superscript "$*$" represents the conjugate. Indeed, there are many methods for sampling complex numbers in the unit circle. Here, we sample the magnitude and the real part of complex values. If the real part is larger than the magnitude, then the sample is set to be a real number; otherwise it is set to be a complex number, where the imaginary part is calculated from the magnitude and the real part.

Using the characteristic roots $\lambda_1, \ldots, \lambda_N$, one can construct the corresponding coefficients as

$$a_q = \sum_{\{i_1, \ldots, i_q\} \in \mathcal{C}_N^q} \lambda_{i_1} \cdots \lambda_{i_q}\,, \tag{5.32}$$

where the set $\mathcal{C}_N^k$ contains all possible combinations for picking k values from the set $\{1, \ldots, N\}$. Then, we repeat the aforementioned random sampling for M times, where M is a sufficiently large number. This leads to M sets of candidate coefficients $\{a_q\}_m$ for $m = 1, \ldots, M$. A larger size of candidate pool may improve the accuracy of the solution to (5.30), but it also requires more computational resources. Considering that, for LTI systems, similar coefficients will lead to similar dynamics, we cluster these coefficients by using the k-means approach [82], which leads to K groups of representative coefficients $\{a_q\}_k$ for $k = 1, \ldots, K$. We remark that K is typically much smaller than M.

Then, we compute $\min_{\theta_a, \theta_b} J(\theta_a, \theta_b)$ by iterations $\ell = 0, \ldots, L$ with L denoting the maximum iteration steps. First, we randomly initialize $\theta_b^{(0)}$ where the superscript indicates the iteration index. Then, for each iteration $\ell = 1, \ldots, L$, we update $\theta_a^{(\ell)}$ according to

$$\theta_a^{(\ell)} = \underset{\{a_{q,k}\},\, k=1,\ldots,K}{\operatorname{argmin}} J\big(\{a_{q,k}\}, \theta_b^{(\ell-1)}\big)\,, \tag{5.33}$$

where $\{a_q\}_k$ is the k-th representative candidates. Since K is typically small, the minimizer of (5.33) can be obtained by comparing the cost for each $\{a_q\}_k$ where $k = 1, \ldots, K$. Then, we update $\theta_b^{(\ell)}$ by using the gradient descent approach

$$\theta_b^{(\ell)} = \theta_b^{(\ell-1)} - \rho\, \nabla_{\theta_b} J\big(\theta_a^{(\ell)}, \theta_b^{(\ell-1)}\big)\,, \tag{5.34}$$

where the step size ρ is used to ensure that the cost decreases at each step, i.e.,

$$J\big(\theta_a^{(\ell)}, \theta_b^{(\ell)}\big) \leq J\big(\theta_a^{(\ell)}, \theta_b^{(\ell-1)}\big)\,. \tag{5.35}$$

We remark that, once the coefficients θ_a and θ_b are obtained, we freeze these coefficients and use the model (5.27) to predict the motion of vehicle $i-1$, until the relevance detector or the link-length estimator indicates that the configuration of vehicle network has changed.

For BLOS perception, we have presented the causality detector (5.12), link-length estimator (5.24,5.26), and network-dynamics identifier (5.27). The time sequence for the activation of these three functions is shown in Fig. 5.2. In particular, the causality detector is activated when the V2V communication starts. The detection of causality activates the link-length estimator. Once the estimated link length converges, the network-dynamics identifier is activated. The estimated link length is said to converge if it maintains the same value for a sufficiently long time. In the subsequent simulation, we consider $\Delta \cdot \delta t$ as a sufficiently long time. Note that both the link-length estimator and the network-dynamics identifier use historical data. That is, when the link-length estimator is activated at t_1, it uses the data between $t_1 - \Delta \cdot \delta t$ and t_1; cf. (5.1). Similarly, when the network-dynamics

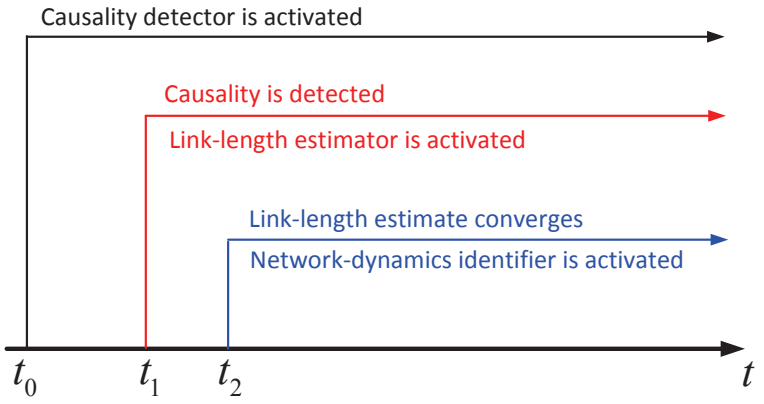

Figure 5.2: Time sequence for the activation of causality detector (5.12), link-length estimator (5.24) or (5.26), and network-dynamics identifier (5.27). The causality detector is activated when the V2V communication starts. If the causality is detected, the link-length estimator is activated. The convergence of estimated link length triggers the activation of the network-dynamics identifier.

Figure 5.3: A vehicle network where the CCC vehicle 4 monitors the motion of vehicle 3 via range sensors and also receives information from vehicle 0 by V2V communication.

identifier is activated at t_2, it uses the data between $t_2 - \Delta \cdot \delta t$ and t_2.

5.4 Numerical Simulations

In this section, we use numerical simulations to validate the analytical results and test the robustness of our presented estimators against varying configurations of vehicle networks. In particular, we consider the 5-vehicle network shown in Fig. 5.3, where CCC vehicle 4 monitors the motion of vehicle 3 via range sensors and also receives information from distant vehicles via V2V communication. Here, we consider the worst-case scenario where only vehicle 0 broadcasts information. We assume that the car-following dynamics of vehicles 1–3 are governed by the optimal velocity model [59]

$$\begin{aligned} \dot{s}_j(t) &= v_j(t)\,, \\ \dot{v}_j(t) &= \alpha_j\big(V_j(h_{j,j-1}(t-\sigma_j)) - v_j(t-\sigma_j)\big) + \beta_j\big(v_{j-1}(t-\sigma_j) - v_j(t-\sigma_j)\big)\,, \end{aligned} \tag{5.36}$$

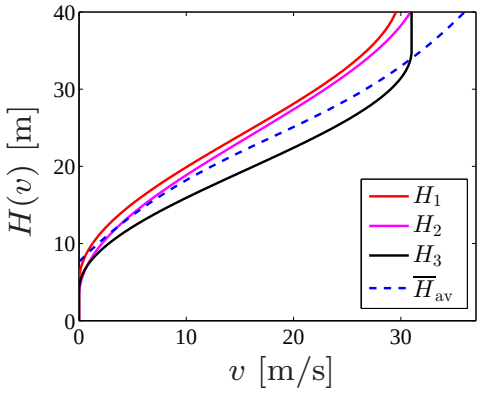

Figure 5.4: Range policies for vehicles 1–3 (solid curves) and the empirical average range policy (dashed curve).

for $j = 1, 2, 3$, where α_j, $\beta_j > 0$ are control gains, σ_j denotes the human reaction time, and the function V_j is in the form of (2.9) with (2.11).

Considering the heterogeneity in the real traffic, we use different parameters for different vehicles:

- Vehicle 0 has length $l_0 = 4.8$ [m] and follows a given speed profile.
- Vehicle 1 is with $\alpha_1 = 0.4$ [1/s], $\beta_1 = 0.6$ [1/s], $h_{\mathrm{st},1} = 5$ [m], $h_{\mathrm{go},1} = 43$ [m], $v_{\max,1} = 30$ [m/s], $\sigma_1 = 0.1$ [s], $l_1 = 5.5$ [m].
- Vehicle 2 is with $\alpha_2 = 0.4$ [1/s], $\beta_2 = 0.5$ [1/s], $h_{\mathrm{st},2} = 3$ [m], $h_{\mathrm{go},2} = 45$ [m], $v_{\max,2} = 32$ [m/s], $\sigma_2 = 0.2$ [s], $l_2 = 3.6$ [m].
- Vehicle 3 is with $\alpha_3 = 0.5$ [1/s], $\beta_3 = 0.6$ [1/s], $h_{\mathrm{st},3} = 4$ [m], $h_{\mathrm{go},3} = 35$ [m], $v_{\max,3} = 31$ [m/s], $\sigma_3 = 0.1$ [s], $l_3 = 4.6$ [m].

Here, we consider that vehicle 4 estimates the dynamics of the vehicle network comprised of vehicles 0–3.

To demonstrate the performance of the causality detector, we consider the following scenario. Initially, the distance between vehicles 0 and 1 is 1200 [m] while vehicles 2–4 follow vehicle 1 with initial distances 26 [m], 35 [m], and 30 [m], respectively. The initial velocities of all vehicles are set to 0 [m/s]. The velocity of vehicle 0 is given by using the UMTRI Safety Pilot data. For implementing the causality detector, we use the window size $\Delta = 400$ in (5.1), which corresponds to $\Delta \cdot \delta t = 40$ [s]. The confidence threshold in (5.12) is set to be $\overline{C} = 0.5$. After the causality is detected, the link-length estimator (5.26) is activated to identify the number of vehicles. To find appropriate values for the forgetting

factor μ in (5.26), we conduct a large number of simulations, which show that $0.98 < \mu < 1$ can lead to a balance between the sensitivity and the robustness. Here, we use $\mu = 0.99$. Moreover, we set $\eta = 0.5$ in (5.26) for equal weights on v_0 and v_3. Once the estimated link length converges, we activate the network-dynamics identifier (5.27). The empirical vehicle length is set to $\bar{l}_{\rm av} = 4.5$ [m]. To obtain the empirical range policy, we use (2.9) and assume the parameters in the ranges $3 \leq h_{\rm st} \leq 8$ [m], $35 \leq h_{\rm go} \leq 45$ [m], $30 \leq v_{\max} \leq 37$ [m/s]. Then, we randomly sample 10000 sets of parameters $\{h_{\rm st},\ h_{\rm go},\ v_{\max}\}$ using uniform distributions within their ranges. Then, we use the obtained range policies to calculate the empirical average range policy $\overline{H}_{\rm av}(v)$ by averaging them for each v; see Fig. 5.4.

The corresponding simulation results are shown in Fig. 5.5. The velocities of vehicles 0–3 are displayed in Fig. 5.5(a), where the zoomed-in panel highlights the moment when vehicle 1 catches up with vehicle 0. Fig. 5.5(b) shows the output of the causality detector, which detects the causality at $t_1 = 96.4$ [s]. The time difference between the instant when vehicle 0 begins to influence vehicle 3 and the instant when the causality is detected is around 40 [s], corresponding to the window size $\Delta = 400$; cf. (5.1). The estimated lag phase as a function of time is displayed in Fig. 5.5(c). The distribution of lag phases obtained at $t = 250$ [s] is shown in Fig. 5.5(d). The discrepancy function (5.13) and the concentration factor (5.11) are shown in Fig. 5.5(e) and (f), respectively. Note that the abrupt changes in the estimated lag phase $\hat{\tau}$ lead to the increase of discrepancy; cf. Fig. 5.5(c) and (e). The activation of the link length estimator is triggered by the detection of causality at $t_1 = 96.4$ [s]; see Fig. 5.5(a). Fig. 5.5(g) shows that the link length estimator starts by using the historical data from $t_1 - \Delta \cdot \delta t = 56.4$ [s], and the estimated link length $\hat{n}$ converges to the real value $n = 3$. The convergence is determined at $t_2 = 100.9$ [s], which triggers the activation of the network-dynamics identifier that uses the historical data from $t_2 - \Delta \cdot \delta t = 60.9$ [s]. Fig. 5.5(h) shows that the output of the network-dynamics identifier tracks the real velocity v_3 with small tracking errors, even though we use a linear discrete-time model to approximate the dynamics of a nonlinear time-delayed system. This implies that the linear model can be used for the subsequent control design.

In practice, the configuration of a vehicle network may change due to the lane changes. To test the response of our presented estimator, we consider the scenario where vehicles 0, 2, 3 move in the same lane while vehicle 1 cuts in between vehicles 0 and 2 at $t = 70$ [s]. To simulate this, we assume that vehicle 1 cuts in at speed 15 [m/s], and after the cut-in it responds to the motion of vehicle 0 using the car-following model (5.36). We also assume that vehicle 2 decelerates with constant acceleration -0.4 [$\mathrm{m/s^2}$] between $t = 64$ [s] and $t = 70$ [s] to leave a space for the cut-in, while vehicles 3 and 4 always responds to the motion of vehicle 2 using the car-following model (5.36). This is highlighted in the

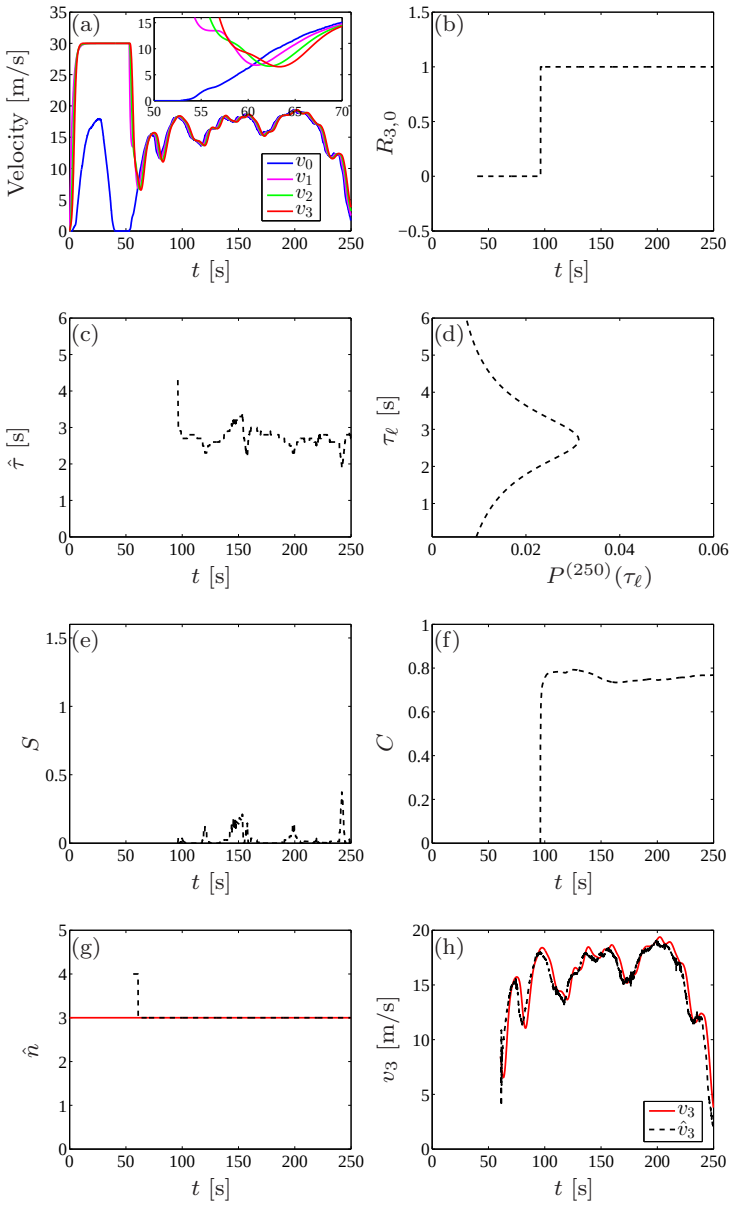

Figure 5.5: (a) Velocities of vehicles 0–3. (b) Causality indicator $R_{3,0}$ that implies whether the information of vehicle 0 is relevant to vehicle 3. (c) Estimated lag phase. (d) Distribution $P(\tau_\ell)$ at time $t = 250$ [s]. (e) Discrepancy function given by (5.13). (f) Concentration function (5.11). (g) Output of the link length estimator (5.26). (h) Comparison between the output of the network dynamics identifier (5.27) and the real velocity of vehicle 3.

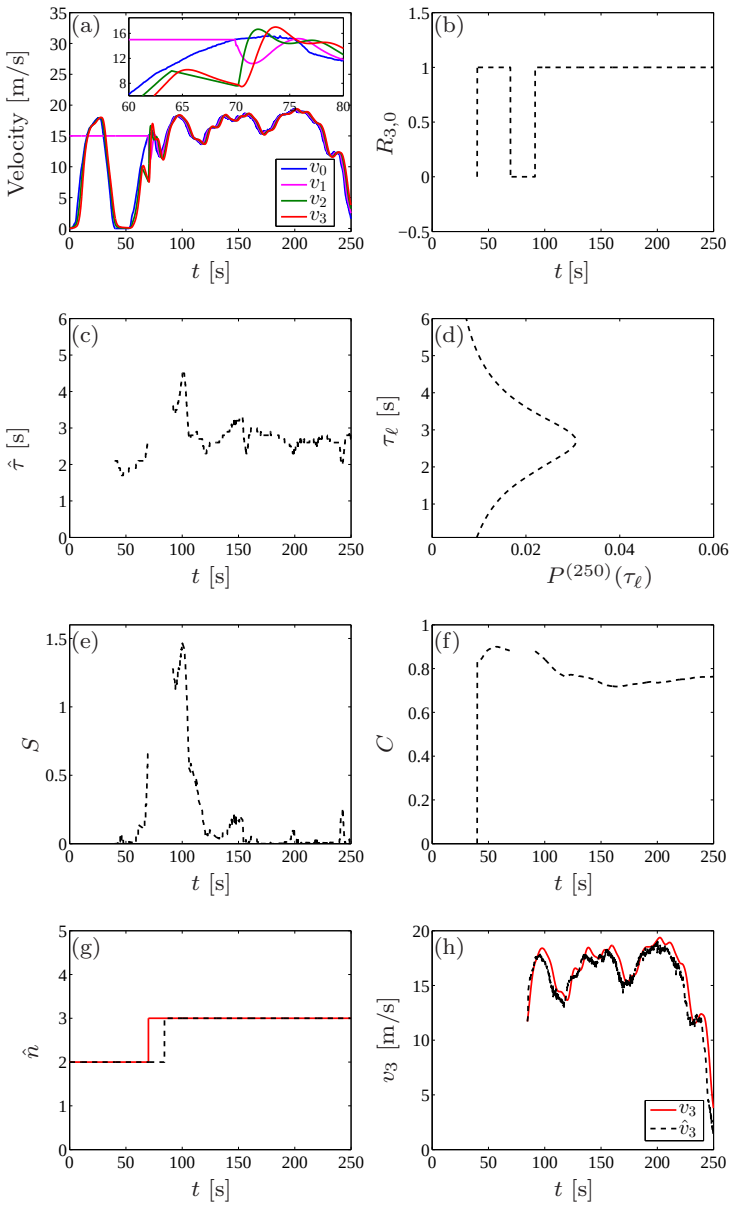

Figure 5.6: Simulation for the scenario where vehicle 1 cuts in between vehicle 0 and vehicle 2 at $t = 70$ [s]. Notations are the same with those in Fig. 5.5. The discontinuities in (c), (e), and (f) are caused by the cut-in of vehicle 1.

zoomed-in panel of Fig. 5.6(a). Fig. 5.6(b) indicates the causal relation between the motion of vehicles 0 and 3 at the beginning and after the cut-in of vehicle 1. In the middle time range, $R_{3,0}$ becomes 0 because the cut-in of vehicle 1 leads to non-causality between the motion of vehicles 0 and 3; cf. Fig. 5.6(a) and (b). In Fig. 5.6(c,e,f), the discontinuities are also caused by the cut-in of vehicle 1, which yields that $\max_\ell \tilde{w}^{(t_k)}(\tau_\ell)$ is smaller than the threshold. Fig. 5.6(g) shows that the estimation of link length converges to the real value in about 10 [s]. Fig. 5.6(h) demonstrates that the estimated dynamics can follow the real dynamics.

5.5 Summary

In this chapter, we investigated beyond-line-of-sight (BLOS) perception by exploiting wireless V2V communication. In particular, we proposed three estimators that play significant roles in the design of connected cruise control (CCC). First, we presented a causality detector that was used to indicate whether the information received from distant vehicles was relevant to the motion of the CCC vehicle. Then, we designed a link-length estimator to identify the number of vehicles between the broadcasting vehicle and the CCC vehicle, which was crucial for appropriately integrating the motion data of broadcasting vehicles in CCC. Finally, we provided a network-dynamics identifier to approximate the nonlinear time-delayed dynamics of connected vehicle networks, which was required for designing CCC for system-level performance such as string stability and collision avoidance. The coefficients of the identifier were obtained by minimizing a cost function and ensuring the stability of the model. An efficient approach was proposed in this chapter to solve the optimization problem with constraints on stability. Numerical simulations were used to validate the analytical results, which also showed their robustness against packet drops in V2V communication and their sensitivity to the change of configuration of vehicle networks.

CHAPTER 6

Conclusions and Future Work

6.1 Conclusions

In this dissertation, we investigated the design of connected cruise control (CCC) by exploiting vehicle-to-vehicle (V2V) communication to improve vehicle safety and mobility. To reduce the complexity for design and analysis, we used a hierarchical framework that was comprised of three levels: perception level, planning level, and execution level.

The perception level was designed for beyond-line-of-sight situation awareness. In particular, our presented perception level had three functions. First, it was able to detect whether the information broadcasted by other vehicles are relevant for the CCC vehicle. This is crucial for avoiding incorporating irrelevant information into the vehicle control systems, which may lead to safety issues. Moreover, the perception level can identify the number of vehicles between the broadcasting vehicle and the CCC vehicle. Such information is important when utilizing the motion data of the broadcasting vehicle in the controller. Furthermore, at the perception level we were able to approximate the nonlinear time-delayed dynamics of the vehicle network in front of the CCC vehicle, which is necessary for achieving system-level performance such as string stability.

At the planning level, we presented a general controller to generate desired car-following dynamics by incorporating the information received from multiple vehicles ahead. This controller was able to guarantee a unique uniform flow equilibrium that is independent of the network size, connectivity topologies, information delays, and control gains. Such property is important for ensuring the performance of vehicle network in varying traffic environment. The effects of information delays, connectivity topologies, and nonlinear dynamics on the dynamics of vehicle networks were investigated: we derived conditions for choosing control gains to mitigate traffic congestions. A motif-based approach was proposed to modularly construct vehicle networks so that the design remain scalable for large networks. Numerical simulations showed the potentials of CCC for enhancing vehicle mo-

bility by attenuating disturbances that propagated backward along the vehicle chain.

The execution level was designed to regulate the engine torque such that the vehicle state tracked the desired CCC dynamics generated at the planning level. In particular, we considered the physics-based vehicle model that included aerodynamic drag, rolling resistance, and road angle. Then, an adaptive sliding-mode controller was presented that guaranteed the tracking performance in presence of uncertainties arising from vehicle parameters and external disturbances.

6.2 Future Work

The work presented in this dissertation can be extended in the following directions. At the perception level, we rely on a relatively large amount of historical data to achieve a high estimation accuracy. However, this also increases the time for estimation. Thus, in the future we will investigate how to optimize the algorithm to reduce the memory size while keeping the estimation accuracy. Moreover, when identifying the dynamics of vehicle networks, we considered the information delays as modeling errors that were minimized when solving for the model coefficients. How to incorporate these information delays into the identification model to increase estimation accuracy will also be studied in the future.

At the planning level, the control gains were designed by assuming constant delays. However, in practice the values of delays may vary due to the stochastic packet drops in V2V communication. How to design control gains in presence of time-varying delays will be investigated in the future. Moreover, in this dissertation we focused on the disturbance attenuation in steady state, while the attenuation of transient disturbances will be studied in the future.

For designing the execution-level controller, we considered the physical effects including aerodynamic drag, rolling resistance, and road inclination angle. To improve the robustness of the controller, in the future we will take into account more effects such as flexibility of tire and suspension, dynamics of transmission, and engine dynamics. Furthermore, the fuel efficiency will also be considered in the design of the execution-level controller.

Finally, this dissertation was focused on single-lane scenarios. The current results will also be extended to multi-lane scenarios in the future.

APPENDIX A

Proofs of Theorems

A.1 Proof of Theorem 1

Substituting (2.12) into (2.2) while considering (2.15), we obtain the closed-loop dynamics

$$\begin{aligned}\dot{h}_{i\mathrm{d},i-1}(t) &= v_{i-1}(t) - v_{i\mathrm{d}}(t)\,,\\ \dot{v}_{i\mathrm{d}}(t) &= \sum_{j=p}^{i-1}\Big[\alpha_{i,j}\big(V\big(h_{i\mathrm{d},j}(t-\xi_{i,j})\big) - v_{i\mathrm{d}}(t-\xi_{i,j})\big) + \beta_{i,j}\big(v_j(t-\xi_{i,j}) - v_{i\mathrm{d}}(t-\xi_{i,j})\big)\Big]\,.\end{aligned} \tag{A.1}$$

When determining the equilibrium of vehicle i, we assume that vehicles $j = p, \ldots, i-1$ have reached equilibrium, i.e., $v_j(t) \equiv v^*$ and $h_{j,j-1}(t) \equiv h^*$. Then, to find the equilibrium of vehicle i, one needs to solve the equations

$$\begin{aligned}0 &= v^* - v^*_{i\mathrm{d}}(t)\,,\\ 0 &= \sum_{j=p}^{i-1}\Big[\alpha_{i,j}\big(V\big(h^*_{i\mathrm{d},j}(t-\xi_{i,j})\big) - v^*_{i\mathrm{d}}(t-\xi_{i,j})\big) + \beta_{i,j}\big(v^* - v^*_{i\mathrm{d}}(t-\xi_{i,j})\big)\Big]\,.\end{aligned} \tag{A.2}$$

The first equation in (A.2) yields

$$v^*_{i\mathrm{d}}(t) \equiv v^*\,. \tag{A.3}$$

Substituting this into the second equation in (A.2) leads to

$$0 = \sum_{j=p}^{i-1}\alpha_{i,j}\big(V\big(h^*_{i\mathrm{d},j}(t-\xi_{i,j})\big) - v^*\big)\,. \tag{A.4}$$

Considering (2.15), we have

$$h^*_{\mathrm{id},j}(t) = \frac{h^*_{\mathrm{id},i-1}(t) + (i-j-1)h^*}{i-j}\,. \tag{A.5}$$

Thus, one candidate solution for (A.4) is

$$h^*_{\mathrm{id},i-1}(t) \equiv h^*\,, \tag{A.6}$$

which satisfies (2.16). The equation (A.4) can be rewritten as

$$\sum_{j=p}^{i-1} \alpha_{i,j} V\big(h^*_{\mathrm{id},j}(t-\xi_{i,j})\big) = \sum_{j=p}^{i-1} \alpha_{i,j} v^*\,. \tag{A.7}$$

When $\overline{\alpha}_{i,j} > 0$ for $j = p, \ldots, i-1$ in (2.13), the left hand side of (A.7) is a strictly monotonically increasing function of $h^*_{\mathrm{id},i-1}$ for $0 < v^* < v_{\max}$; cf. (2.9). The right hand side of (A.7) is a constant. Therefore, if there exists a solution to (A.7), the solution is unique. Note that the equilibrium (A.3) and (A.6) is independent of the network size, connectivity topologies, control gains, and information delays.

A.2 Proof of Theorem 8

To investigate the plant stability of vehicle i at the nonlinear level, we use the Lyapunov-Krasovskii functional

$$\begin{aligned} L = {} & \tilde{x}_i^{\mathrm{T}}(t)\, P_i\, \tilde{x}_i(t) + \sum_{j=1}^{m_i} \int_{t-\sigma_{i,j}}^{t} \tilde{x}_i^{\mathrm{T}}(\tau)\, Q_{i,j}\, \tilde{x}_i(\tau)\, \mathrm{d}\tau \\ & + \sum_{j=1}^{m_i} \int_{-\sigma_{i,j}}^{-\sigma_{i,j-1}} \int_{t+\theta}^{t} \dot{\tilde{x}}_i^{\mathrm{T}}(\tau)\, W_{i,j}\, \dot{\tilde{x}}_i(\tau)\, \mathrm{d}\tau \mathrm{d}\theta\,, \end{aligned} \tag{A.8}$$

where matrices P_i, $Q_{i,j}$, and $W_{i,j}$ are all positive definite for $j = 1, \ldots, m_i$. Substituting (3.9) and (3.11) into the time derivative of (A.8) while adding the identity

$$0 = \sum_{q=2}^{m_i} (\sigma_{i,q} - \sigma_{i,q-1}) \tilde{x}_i^{\mathrm{T}}(t)\, R_{i,q}\, \tilde{x}_i(t) - \sum_{q=2}^{m_i} \int_{t-\sigma_{i,q}}^{t-\sigma_{i,q-1}} \tilde{x}_i^{\mathrm{T}}(t)\, R_{i,q}\, \tilde{x}_i(t)\, \mathrm{d}\tau \tag{A.9}$$

to the result leads to

$$\dot{L} = \Delta_i(t) - \sum_{j=1}^{m_i} 2\tilde{x}_i^{\mathrm{T}}(t) P_i \overline{A}_{i,j} \int_{t-\sigma_{i,j}}^{t-\sigma_{i,j-1}} \dot{\tilde{x}}_i(\tau)\,\mathrm{d}\tau - \sum_{j=1}^{m_i} \int_{t-\sigma_{i,j}}^{t-\sigma_{i,j-1}} \dot{\tilde{x}}_i^{\mathrm{T}}(\tau) W_{i,j} \dot{\tilde{x}}(\tau)\,\mathrm{d}\tau$$
$$- \sum_{q=2}^{m_i} \int_{t-\sigma_{i,q}}^{t-\sigma_{i,q-1}} \tilde{x}_i^{\mathrm{T}}(t) R_{i,q} \tilde{x}_i(t)\,\mathrm{d}\tau\,, \tag{A.10}$$

where

$$\Delta_i(t) = \sigma_{i,1} \tilde{x}_i^{\mathrm{T}}(t)(Z - Y_{0,0})\tilde{x}_i(t) - \sum_{j=1}^{m_i} \tilde{x}_i^{\mathrm{T}}(t-\sigma_{i,j}) Q_{i,j} \tilde{x}_i(t-\sigma_{i,j})$$
$$+ \Bigg(\sum_{k=0}^{m_i} \hat{A}_{i,k} \tilde{x}_i(t-\sigma_{i,k}) \Bigg)^{\mathrm{T}} \Bigg(\sum_{j=1}^{m_i} (\sigma_{i,j} - \sigma_{i,j-1}) W_{i,j} \Bigg) \Bigg(\sum_{k=0}^{m_i} \hat{A}_{i,k} \tilde{x}_i(t-\sigma_{i,k}) \Bigg)\,, \tag{A.11}$$

where $Y_{0,0}$ and Z are given in (3.14). Then, substituting the identity

$$\Delta_i(t) = \frac{1}{\sigma_{i,1}} \int_{t-\sigma_{i,1}}^{t} \Delta_i(t)\,\mathrm{d}\tau \tag{A.12}$$

into (A.10) and writing the results in matrix form results in

$$\dot{L} = \int_{t-\sigma_{i,1}}^{t} \tilde{\chi}_i^{\mathrm{T}}(t,\tau) \Xi_{i,1}(\Psi_i) \tilde{\chi}_i(t,\tau)\,\mathrm{d}\tau + \sum_{q=2}^{m_i} \int_{t-\sigma_{i,q}}^{t-\sigma_{i,q-1}} \tilde{X}_i^{\mathrm{T}}(t,\tau) \Xi_{i,q}(\Psi_i) \tilde{X}_i(t,\tau)\,\mathrm{d}\tau\,, \tag{A.13}$$

where $\tilde{\chi}_i^{\mathrm{T}}(t,\tau) = [\tilde{x}_i^{\mathrm{T}}(t-\sigma_{i,0}), \ldots, \tilde{x}_i^{\mathrm{T}}(t-\sigma_{i,m_i}), \dot{\tilde{x}}_i^{\mathrm{T}}(\tau)]$ and $\tilde{X}_i^{\mathrm{T}}(t,\tau) = [\tilde{x}_i^{\mathrm{T}}(t), \dot{\tilde{x}}_i^{\mathrm{T}}(\tau)]$ while $\Xi_{i,1}(\Psi_i)$ and $\Xi_{i,q}(\Psi_i)$ for $q = 2, \ldots, m_i$ are given in (3.13).

Suppose that the eigenvalues and the corresponding normalized eigenvectors of $\Xi_{i,j}(\Psi_i)$ are given by $\lambda_{j,k}(\Psi_i)$ and $\eta_{j,k}(\Psi_i)$, respectively, for $j = 1, \ldots, m_i$ and $k = 1, \ldots, n_j$, where $n_1 = 2m_i + 4$ and $n_j = 4$ for $j = 2, \ldots, m_i$; cf. (3.13). Since $\Xi_{i,j}(\Psi_i)$ is symmetric, the eigenvectors $\eta_{j,1}(\Psi_i), \ldots, \eta_{j,n_j}(\Psi_i)$ are orthogonal to each other for $\forall \Psi_i \in \mathcal{D}_h^{i-p_i}$ and for $j = 1, \ldots, m_i$. Here, the matrices

$$\begin{aligned} \Lambda_j(\Psi_i) &= \mathrm{diag}\big\{ \lambda_{j,1}(\Psi_i)\,, \ldots\,, \lambda_{j,n_j}(\Psi_i) \big\}\,, \\ T_j(\Psi_i) &= \big[\eta_{j,1}(\Psi_i)\,, \ldots\,, \eta_{j,n_j}(\Psi_i) \big] \end{aligned} \tag{A.14}$$

have the following properties

$$T_j(\Psi_i)\,T_j^{\mathrm{T}}(\Psi_i) = I\,, \quad \text{and} \quad T_j^{\mathrm{T}}(\Psi_i)\,\Xi_{i,j}(\Psi_i)\,T_j(\Psi_i) = \Lambda_j(\Psi_i)\,, \tag{A.15}$$

for $j = 1, \ldots, m_i$. Indeed, $\Lambda_j(\Psi_i)$ is negative definite for $\forall \Psi_i \in \mathcal{D}_h^{i-p_i}$ since $\Xi_{i,j}(\Psi_i)$ is negative definite for $\forall \Psi_i \in \mathcal{D}_h^{i-p_i}$.

Let

$$\begin{aligned} Y_1(\Psi_i, t, \tau) &= \big[y_{1,k}(\Psi_i, t, \tau)\big] = T_1^{\mathrm{T}}(\Psi_i)\,\tilde{\chi}_i(t, \tau)\,, \\ Y_j(\Psi_i, t, \tau) &= \big[y_{j,k}(\Psi_i, t, \tau)\big] = T_j^{\mathrm{T}}(\Psi_i)\,\tilde{X}_i(t, \tau)\,, \end{aligned} \tag{A.16}$$

for $j = 2, \ldots, m_i$. Then, it follows that

$$\begin{aligned} \tilde{\chi}_i^{\mathrm{T}}(t, \tau)\,\Xi_{i,1}(\Psi_i)\,\tilde{\chi}_i(t, \tau) &= Y_1^{\mathrm{T}}(\Psi_i, t, \tau)\,\Lambda_1(\Psi_i)\,Y_1(\Psi_i, t, \tau) \\ &= \sum_{k=1}^{n_1} \lambda_{1,k}(\Psi_i)\,y_{1,k}^2(\Psi_i, t, \tau)\,, \\ \tilde{X}_i^{\mathrm{T}}(t, \tau)\,\Xi_{i,j}(\Psi_i)\,\tilde{X}_i(t, \tau) &= Y_j^{\mathrm{T}}(\Psi_i, t, \tau)\,\Lambda_j(\Psi_i)\,Y_j(\Psi_i, t, \tau) \\ &= \sum_{k=1}^{n_j} \lambda_{j,k}(\Psi_i)\,y_{j,k}^2(\Psi_i, t, \tau) \end{aligned} \tag{A.17}$$

are negative definite for $\forall \Psi_i \in \mathcal{D}_h^{i-p_i}$ and $j = 2, \ldots, m_i$. Considering this in (A.13), $\dot{L}$ becomes negative definite since the integration does not change the negative sign. The only solution for $\dot{L} = 0$ is $Y_j(\Psi_i, t, \tau) = 0$ for $j = 1, \ldots, m_i$. It follows that $\tilde{\chi}_i(t, \tau) = 0$ and $\tilde{X}_i(t, \tau) = 0$ is the unique solution for $\dot{L} = 0$, implying that $\tilde{x}_i(t) \to 0$ as $t \to \infty$.

A.3 Proof of Theorem 9

First, we study the steady state of vehicle i by assuming that states of vehicles $j = 0, 1, \ldots, i-1$ are T-periodic such that

$$e_j(t) = \begin{bmatrix} e_{j,s}(t) \\ e_{j,v}(t) \end{bmatrix} \triangleq \begin{bmatrix} s_j(t+T) - s_j(t) \\ v_j(t+T) - v_j(t) \end{bmatrix} \equiv 0\,. \tag{A.18}$$

Substituting $t = t + T$ into the closed-loop system (2.17), subtracting the result from

(2.17) while considering the definition (A.18) for $j = i$, we obtain

$$\dot{e}_i(t) = \begin{bmatrix} e_{i,v}(t) \\ \sum_{j=p}^{i-1} \alpha_{i,j}\Big(V\big(h_{i,j}(t+T-\xi_{i,j})\big) - V\big(h_{i,j}(t-\xi_{i,j})\big)\Big) - \kappa_{i,j} e_{i,v}(t-\xi_{i,j}) \end{bmatrix}. \tag{A.19}$$

When $h_{i,j}(t) \in \mathcal{D}_h$, according to the mean value theorem, there exists $\mu_{i,j} \in \mathcal{D}_h$ such that

$$V\big(h_{i,j}(t+T)\big) - V\big(h_{i,j}(t)\big) = -\frac{V'(\mu_{i,j})}{i-j} e_{i,s}(t)\,. \tag{A.20}$$

Substituting (A.20) into (A.19) yields

$$\dot{e}_i(t) = A_0\, e_i(t) + \sum_{j=p}^{i-1} A_{i,j}(\mu_{i,j})\, e_i(t-\xi_{i,j})\,, \tag{A.21}$$

Similar to (3.7)–(3.9), we collect terms according to distinct delays $\sigma_{i,k}$ for $k = 0, \ldots, m_i$ and obtain

$$\dot{e}_i(t) = \sum_{k=0}^{m_i} \hat{A}_{i,k}(U_i)\, e_i(t-\sigma_{i,k})\,, \tag{A.22}$$

where $U_i = [\mu_{i,p}, \ldots, \mu_{i,i-1}]$. Note that (A.22) is equivalent to (3.9) since $\hat{A}_{i,k}(U_i)$ and $\hat{A}_{i,k}(\Psi_i)$ have the same bound for all $U_i, \Psi_i \in \mathcal{D}_h^{i-p_i}$. Therefore, $e_i(t) = 0$ is asymptotically stable for (A.22) if $\tilde{x}_i(t) = 0$ if asymptotically stable for (3.9), which implies that $\lim_{t\to\infty} e_i(t) = 0$ if Theorem 8 holds and $e_j(t) = 0$ for $j = p, \ldots, i-1$.

Since vehicle 1 only reacts to vehicle 0, when the disturbance imposed on vehicle 0 is T-periodic (i.e., $e_0(t) \equiv 0$), it follows that $\lim_{t\to\infty} e_1(t) = 0$. Repeating this process to vehicles $j = 2, \ldots, n$, one can show that the steady states of all vehicles in the network are T-periodic.

Then, we prove the uniqueness of the periodic steady states by contradiction. We assume that the steady states of vehicles $j = 0, 1, \ldots, i-1$ are unique but vehicle i has two distinct steady-state trajectories corresponding to different initial conditions. We denote these two steady-state trajectories by $s_i^{(1)}(t)$, $v_i^{(1)}(t)$ and $s_i^{(2)}(t)$, $v_i^{(2)}(t)$, of which the dynamics is governed by

$$\begin{aligned} \dot{s}_i^{(k)}(t) &= v_i^{(k)}(t)\,, \\ \dot{v}_i^{(k)}(t) &= \sum_{j=p}^{i-1} \alpha_{i,j}\big(V\big(h_{i,j}^{(k)}(t-\xi_{i,j})\big) - v_i^{(k)}(t-\xi_{i,j})\big) + \beta_{i,j}\big(v_j(t-\xi_{i,j}) - v_i^{(k)}(t-\xi_{i,j})\big)\,, \end{aligned} \tag{A.23}$$

for $k = 1, 2$, where $h_{i,j}^{(k)}(t) = \big(s_j(t) - s_i^{(k)}(t) - \sum_{q=j}^{i-1} l_q\big)/(i-j)$; cf. (2.15) and (2.17). Subtracting (A.23) with $k = 1$ from (A.23) with $k = 2$ yields

$$\begin{aligned} \dot{\zeta}_i(t) &= \nu_i(t)\,, \\ \dot{\nu}_i(t) &= \sum_{j=p}^{i-1} \alpha_{i,j} \Big(V\big(h_{i,j}^{(1)}(t-\xi_{i,j})\big) - V\big(h_{i,j}^{(2)}(t-\xi_{i,j})\big) \Big) - \kappa_{i,j}\nu_i(t-\xi_{i,j})\,, \end{aligned} \tag{A.24}$$

where $\zeta_i(t) = s_i^{(1)}(t) - s_i^{(2)}(t)$ and $\nu_i(t) = v_i^{(1)}(t) - v_i^{(2)}(t)$. When $h_{i,j}^{(1)}(t), h_{i,j}^{(2)}(t) \in \mathcal{D}_h$ holds for all $t \geq 0$, one can apply the mean value theorem and obtain variables $\vartheta_{i,j} \in \mathcal{D}_h$ such that

$$V\big(h_{i,j}^{(1)}(t)\big) - V\big(h_{i,j}^{(2)}(t)\big) = -\frac{V'(\vartheta_{i,j})}{i-j}\zeta_i(t)\,. \tag{A.25}$$

Defining $\phi_i(t) = [\zeta_i(t),\, \nu_i(t)]^{\mathrm{T}}$ and plugging (A.25) into (A.24) leads to

$$\dot{\phi}_i(t) = A_{i,0}\,\phi_i(t) + \sum_{j=p}^{i-1} A_{i,j}(\vartheta_{i,j})\,\phi_i(t-\xi_{i,j})\,. \tag{A.26}$$

Similar to (3.7)–(3.9), we collect terms according to distinct delays $\sigma_{i,k}$ for $k = 0, \ldots, m_i$ and obtain

$$\dot{\phi}_i(t) = \sum_{k=0}^{m_i} \hat{A}_{i,k}(\vartheta_i)\,\phi_i(t-\sigma_{i,k})\,, \tag{A.27}$$

where $\vartheta_i = [\vartheta_{i,p_i}, \ldots, \vartheta_{i,i-1}]$. This system is equivalent to (3.9), since $\hat{A}_{i,k}(\vartheta_i)$ and $\hat{A}_{i,k}(\Psi_i)$ have the same bound for all $\vartheta_i, \Psi_i \in \mathcal{D}_h^{i-p_i}$. Therefore, if Theorem 8 holds, we have $\lim_{t\to\infty} \phi_i(t) = 0$, implying that $s_i^{(1)}(t) = s_i^{(2)}(t)$ and $v_i^{(1)}(t) = v_i^{(2)}(t)$ at the steady state, which contradicts our original assumption. Hence the proof is completed by contradiction.

A.4 Approximation of the Steady State

Applying Taylor expansion to the system (2.17) about the uniform flow equilibrium (2.3) yields

$$\begin{aligned} \dot{\tilde{x}}_i(t) &= A_{i,0}\,\tilde{x}_i(t) + \sum_{j=p}^{i-1} \Big[A_{i,j}^*\,\tilde{x}_i(t-\xi_{i,j}) + B_{i,j}^*\,\tilde{x}_j(t-\xi_{i,j}) \Big] + F_i\,, \\ \tilde{y}_i(t) &= C\tilde{x}_i(t)\,. \end{aligned} \tag{A.28}$$

Here, $A_{i,0}$, $A^*_{i,j} = A_{i,j}(h^*)$, $B^*_{i,j} = B_{i,j}(h^*)$ are given in (3.5), $C = [0\ 1]$, and

$$F_i = \begin{bmatrix} 0 \\ \sum_{j=p_i}^{i-1} \alpha_{i,j} \sum_{m=2}^{M} \epsilon_m \Big(\frac{\tilde{s}_j(t-\xi_{i,j}) - \tilde{s}_i(t-\xi_{i,j})}{i-j} \Big)^m \end{bmatrix} , \tag{A.29}$$

where M denotes the order of Taylor expansion, and $\epsilon_m = \frac{1}{m!} \frac{\mathrm{d}^m V(h^*)}{\mathrm{d}h^m}$. Defining $\epsilon = [\epsilon_2, \ldots, \epsilon_M]$, one can express the solution of (A.28) as $\tilde{x}_i(t, \epsilon)$ and $\tilde{y}_i(t, \epsilon)$. To make the following expressions more compact, we also define a vector $r = [r_2, \ldots, r_M]$ such that

$$\epsilon^r \triangleq \prod_{m=2}^{M} \epsilon_m^{r_m} . \tag{A.30}$$

Moreover, we define $|r| \triangleq \sum_{m=2}^{M} r_m$. Then, we apply Taylor expansion to $\tilde{x}_i(t, \epsilon)$ and $\tilde{y}_i(t, \epsilon)$ about $\epsilon = 0$ up to the order R, which leads to

$$\tilde{x}_i(t, \epsilon) = \sum_{|r|=0}^{R} \epsilon^r \tilde{x}_{i,r}(t) , \quad \tilde{y}_i(t, \epsilon) = \sum_{|r|=0}^{R} \epsilon^r \tilde{y}_{i,r}(t) . \tag{A.31}$$

Substituting (A.31) into (A.28) and (A.29) while matching coefficients of ϵ^r yields

$$\begin{aligned} \dot{\tilde{x}}_{i,r}(t) &= A_{i,0} \tilde{x}_{i,r}(t) + \sum_{j=p_i}^{i-1} \Big[A^*_{i,j}\, \tilde{x}_{i,r}(t - \xi_{i,j}) + B^*_{i,j}\, \tilde{x}_{j,r}(t - \xi_{i,j}) \Big] + f_{i,r}\big(X_{i,\hat{r}}(t)\big) , \\ \tilde{y}_{i,r}(t) &= C \tilde{x}_{i,r}(t) , \end{aligned} \tag{A.32}$$

where $X_{i,\hat{r}}(t)$ is comprised of components with the order lower than $|r|$, that is,

$$X_{i,\hat{r}}(t) = \Big[\tilde{x}^{\mathrm{T}}_{p,\hat{r}}(t-\xi_{i,p}),\ \ldots,\ \tilde{x}^{\mathrm{T}}_{i-1,\hat{r}}(t-\xi_{i,i-1}),\ \tilde{x}^{\mathrm{T}}_{i,\hat{r}}(t-\xi_{i,p}),\ \ldots,\ \tilde{x}^{\mathrm{T}}_{i,\hat{r}}(t-\xi_{i,i-1}) \Big]^{\mathrm{T}} \tag{A.33}$$

for all possible $\hat{r}$-s that satisfy $|\hat{r}| < |r|$, while $f_{i,r}(X_{i,\hat{r}}(t))$ can be obtained from (A.29) and satisfies

$$f_{i,0}\big(X_{i,\hat{r}}(t)\big) \equiv 0 , \quad f_{i,r}\big(0\big) = 0 , \tag{A.34}$$

for all r's. Note that the functions $f_{i,r}(X)$ vary for different r-s and may not have a general expression. Here, we only use its property (A.34).

Typically, larger M and R in (A.30) and (A.31)) can improve the approximation accuracy but they also increase the computation complexity. Here, we consider $M = 3$ and

$R = 1$ such that (A.31) becomes

$$\tilde{x}_i(t,\epsilon) = \tilde{x}_{i,[0,0]}(t) + \epsilon_2 \tilde{x}_{i,[1,0]}(t) + \epsilon_3 \tilde{x}_{i,[0,1]}(t)\,, \tag{A.35}$$

for $i = 0, 1, \ldots, n$. For agent 0, considering (3.18) we have

$$\tilde{x}_{0,[0,0]}(t) = \begin{bmatrix} v_{\text{amp}} \sin(\omega t)/\omega \\ v_{\text{amp}} \cos(\omega t) \end{bmatrix}\,, \quad \tilde{x}_{0,[1,0]}(t) = \tilde{x}_{0,[0,1]}(t) \equiv \begin{bmatrix} 0 \\ 0 \end{bmatrix}\,. \tag{A.36}$$

Substituting (A.36) into (A.28) and (A.29) yields

$$\begin{aligned} f_{i,[1,0]}\big(X_{i,\hat{r}}(t)\big) &= \sum_{j=p}^{i-1} \alpha_{i,j} \left(\frac{\tilde{s}_{j,[0,0]}(t-\xi_{i,j}) - \tilde{s}_{i,[0,0]}(t-\xi_{i,j})}{i-j} \right)^2, \\ f_{i,[0,1]}\big(X_{i,\hat{r}}(t)\big) &= \sum_{j=p}^{i-1} \alpha_{i,j} \left(\frac{\tilde{s}_{j,[0,0]}(t-\xi_{i,j}) - \tilde{s}_{i,[0,0]}(t-\xi_{i,j})}{i-j} \right)^3, \end{aligned} \tag{A.37}$$

for $i = 1, \ldots, n$, where

$$X_{i,\hat{r}}(t) = \Big[\tilde{x}^{\mathrm{T}}_{p,[0,0]}(t-\xi_{i,p}),\, \ldots,\, \tilde{x}^{\mathrm{T}}_{i-1,[0,0]}(t-\xi_{i,i-1}),\, \tilde{x}^{\mathrm{T}}_{i,[0,0]}(t-\xi_{i,p}),\, \ldots,\, \tilde{x}^{\mathrm{T}}_{i,[0,0]}(t-\xi_{i,i-1}) \Big]^{\mathrm{T}}, \tag{A.38}$$

cf. (A.33) and (A.34).

For $r = [0, 0]$, the network (A.32) becomes a linear time invariant (LTI) system with excitations that arise from the head vehicle 0, i.e., $\tilde{x}_{0,[0,0]}(t)$ in (A.36), and propagate through all following vehicles to the tail vehicle n. Thus, the corresponding steady state are in the form

$$\tilde{x}^{(\mathrm{s})}_{i,[0,0]} = \begin{bmatrix} a_{i,[0,0]} \\ c_{i,[0,0]} \end{bmatrix} \cos(\omega t) + \begin{bmatrix} b_{i,[0,0]} \\ d_{i,[0,0]} \end{bmatrix} \sin(\omega t)\,, \tag{A.39}$$

where the superscript "(s)" indicates the steady state while $a_{i,[0,0]}, b_{i,[0,0]}, c_{i,[0,0]}, d_{i,[0,0]}$ are constant coefficients to be determined. For compactness, we define a coefficient vector

$$z_{i,[0,0]} = \big[a_{i,[0,0]},\ b_{i,[0,0]},\ c_{i,[0,0]},\ d_{i,[0,0]} \big]^{\mathrm{T}}. \tag{A.40}$$

Substituting (A.39) into (A.32) with $r = [0, 0]$ and matching coefficients of $\cos(\omega t)$ and $\sin(\omega t)$, respectively, we obtain

$$z_{i,[0,0]} = \big(D(\omega)\big)^{-1} E_{i,[0,0]}\,, \tag{A.41}$$

where

$$
\begin{aligned}
D(\omega) &= \begin{bmatrix} \omega F & -I_2 \\ \sum_{j=p}^{i-1} \varphi_{i,j}^* G(\omega\xi_{i,j}) & \omega F + \sum_{j=p}^{i-1} \kappa_{i,j} G(\omega\xi_{i,j}) \end{bmatrix}, \\
E_{i,[0,0]} &= \sum_{j=p}^{i-1} B_{i,j}^* \otimes G(\omega\xi_{i,j}) z_{j,[0,0]}\,,
\end{aligned}
\tag{A.42}
$$

while $\varphi_{i,j}^* = \varphi_{i,j}(h^*)$ is given in (3.6) and

$$
F = \begin{bmatrix} 0 & 1 \\ -1 & 0 \end{bmatrix}, \quad G(\theta) = \begin{bmatrix} \cos(\theta) & -\sin(\theta) \\ \sin(\theta) & \cos(\theta) \end{bmatrix}. \tag{A.43}
$$

Since $\tilde{x}_{0,[1,0]}(t) = \tilde{x}_{0,[0,1]}(t) \equiv 0$, the networks (A.32) with $r = [1,0]$ and $r = [0,1]$ become LTI systems with excitations only arising from $f_{i,[1,0]}$ and $f_{i,[0,1]}$ in (A.37), respectively. Note that $\tilde{x}_{j,[0,0]}^2(t)$ contains frequency 2ω while $\tilde{x}_{j,[0,0]}^3(t)$ contains frequencies ω and 3ω; cf. (A.39). Thus, the steady states of (A.32) for $r = [1,0]$ and $r = [0,1]$ take the form

$$
\begin{aligned}
\tilde{x}_{i,[1,0]}^{(\mathrm{s})} &= \begin{bmatrix} a_{i,[1,0]} \\ c_{i,[1,0]} \end{bmatrix} \cos(2\omega t) + \begin{bmatrix} b_{i,[1,0]} \\ d_{i,[1,0]} \end{bmatrix} \sin(2\omega t)\,, \\
\tilde{x}_{i,[0,1]}^{(\mathrm{s})} &= \begin{bmatrix} a_{i,[0,1],1} \\ c_{i,[0,1],1} \end{bmatrix} \cos(\omega t) + \begin{bmatrix} b_{i,[0,1],1} \\ d_{i,[0,1],1} \end{bmatrix} \sin(\omega t) \\
&\quad + \begin{bmatrix} a_{i,[0,1],3} \\ c_{i,[0,1],3} \end{bmatrix} \cos(3\omega t) + \begin{bmatrix} b_{i,[0,1],3} \\ d_{i,[0,1],3} \end{bmatrix} \sin(3\omega t)\,.
\end{aligned}
\tag{A.44}
$$

We define the coefficient vectors as

$$
\begin{aligned}
z_{i,[1,0]} &= \left[a_{i,[1,0]},\ b_{i,[1,0]},\ c_{i,[1,0]},\ d_{i,[1,0]}\right]^{\mathrm{T}}, \\
z_{i,[0,1],1} &= \left[a_{i,[0,1],1},\ b_{i,[0,1],1},\ c_{i,[0,1],1},\ d_{i,[0,1],1}\right]^{\mathrm{T}}, \\
z_{i,[0,1],3} &= \left[a_{i,[0,1],3},\ b_{i,[0,1],3},\ c_{i,[0,1],3},\ d_{i,[0,1],3}\right]^{\mathrm{T}}.
\end{aligned}
\tag{A.45}
$$

Substituting (A.44) into (A.32) and (A.37) with $r = [1,0]$ and $r = [0,1]$, respectively, we obtain

$$
\begin{aligned}
z_{i,[1,0]} &= \big(D(2\omega)\big)^{-1} E_{i,[1,0]}\,, \\
z_{i,[0,1],1} &= \big(D(\omega)\big)^{-1} E_{i,[0,1],1}\,, \\
z_{i,[0,1],3} &= \big(D(3\omega)\big)^{-1} E_{i,[0,1],3}\,,
\end{aligned}
\tag{A.46}
$$

where the matrix D is given in (A.42) and

$$\begin{aligned}
E_{i,[1,0]} &= \sum_{j=p_i}^{i-1} B_{i,j}^* \otimes G(2\omega\xi_{i,j}) z_{j,[1,0]} + \frac{\alpha_{i,j}}{(i-j)^2} I^* \otimes G(2\omega\xi_{i,j}) J_j \,, \\
E_{i,[0,1],1} &= \sum_{j=p_i}^{i-1} B_{i,j}^* \otimes G(\omega\xi_{i,j}) z_{j,[0,1],1} + \frac{\alpha_{i,j}}{(i-j)^3} I^* \otimes G(\omega\xi_{i,j}) K_j \,, \\
E_{i,[0,1],3} &= \sum_{j=p_i}^{i-1} B_{i,j}^* \otimes G(3\omega\xi_{i,j}) z_{j,[0,1],3} + \frac{\alpha_{i,j}}{(i-j)^3} I^* \otimes G(3\omega\xi_{i,j}) L_j \,,
\end{aligned} \tag{A.47}$$

where

$$\begin{aligned}
I^* &= \begin{bmatrix} 0 & 0 \\ 0 & 1 \end{bmatrix} , \\
J_j &= \begin{bmatrix} 0 \\ 0 \\ \big((a_{j,[0,0]} - a_{i,[0,0]})^2 - (b_{j,[0,0]} - b_{i,[0,0]})^2\big)/2 \\ (a_{j,[0,0]} - a_{i,[0,0]})(b_{j,[0,0]} - b_{i,[0,0]}) \end{bmatrix} , \\
K_j &= \begin{bmatrix} 0 \\ 0 \\ \big(3(a_{j,[0,0]} - a_{i,[0,0]})^3 + 3(a_{j,[0,0]} - a_{i,[0,0]})(b_{j,[0,0]} - b_{i,[0,0]})^2\big)/4 \\ \big(3(a_{j,[0,0]} - a_{i,[0,0]})^2(b_{j,[0,0]} - b_{i,[0,0]}) + 3(b_{j,[0,0]} - b_{i,[0,0]})^3\big)/4 \end{bmatrix} , \\
L_j &= \begin{bmatrix} 0 \\ 0 \\ \big((a_{j,[0,0]} - a_{i,[0,0]})^3 - 3(a_{j,[0,0]} - a_{i,[0,0]})(b_{j,[0,0]} - b_{i,[0,0]})^2\big)/4 \\ \big(3(a_{j,[0,0]} - a_{i,[0,0]})^2(b_{j,[0,0]} - b_{i,[0,0]}) - (b_{j,[0,0]} - b_{i,[0,0]})^3\big)/4 \end{bmatrix} .
\end{aligned} \tag{A.48}$$

Then, one can use (A.39) and (A.44) in (A.35) to approximate the steady states of all vehicles sequentially from 1 to n.

A.5 Proof of Theorem 11

Here, we still use the model (A.32). If the eventual string stability (2.7) can be achieved in (A.32) for $M \to \infty$ and $R \to \infty$, then the cascading vehicle network is capable of eliminating disturbances as the size increases to infinity.

For simplicity, we define O as a zero vector that has the same dimension with r; cf. (A.30). When $r = \mathrm{O}$, assuming zero initial condition, we obtain the Laplace trans-

form of (A.32)

$$\tilde{Y}_{i,\mathrm{O}}(s) = \sum_{j=p_i}^{i-1} T_{i,j}(s, h^*)\tilde{Y}_{j,\mathrm{O}}(s)\,, \tag{A.49}$$

cf. (A.34), where $\tilde{Y}_{i,\mathrm{O}}(s)$ is the Laplace transform of $\tilde{y}_{i,\mathrm{O}}(t)$ and $T_{i,j}(s, h^*)$ can be referred to (2.22) and (2.23) but noting that here φ is indeed $\varphi(h^*)$.

Applying (A.49) into (2.27) leads to the transfer function between vehicle 0 and vehicle n, which is given by $\tilde{Y}_{n,\mathrm{O}}(s) = G_{n,0}(s, h^*)\tilde{Y}_{0,\mathrm{O}}(s)$. Then, we cascade the network by k blocks, where vehicle kn is at the tail. It follows that the transfer function between the head vehicle 0 and the tail vehicle kn becomes

$$\tilde{Y}_{kn,\mathrm{O}}(s) = G^k_{n,0}(s, h^*)\tilde{Y}_{0,\mathrm{O}}(s)\,. \tag{A.50}$$

If the condition (3.23) holds, at the limit $k \to \infty$, we have $|G_{n,0}(\mathrm{j}\omega, h^*)|^k = 0$ and thus $|Y_{kn,\mathrm{O}}(\mathrm{j}\omega)| = 0$ for all $\omega > 0$. Considering $\tilde{X}_j(s) = E(s)\tilde{Y}_j(s)$; cf. (2.22), we have

$$\big\|\tilde{X}_{kn,\mathrm{O}}(\mathrm{j}\omega)\big\| = \big\|E(\mathrm{j}\omega)\tilde{Y}_{kn,\mathrm{O}}(\mathrm{j}\omega)\big\| \le \big\|E(\mathrm{j}\omega)\big\|\big|\tilde{Y}_{kn,\mathrm{O}}(\mathrm{j}\omega)\big| = 0\,, \tag{A.51}$$

for all $\omega > 0$, which implies that the steady state is zero, i.e., $\tilde{x}^{(\mathrm{s})}_{kn,\mathrm{O}}(t) \equiv 0$ with the superscript "(s)" denoting the steady state. Then, for vehicle kn, we assume the components of the steady state $\tilde{x}^{(\mathrm{s})}_{kn,\hat{r}}(t) \equiv 0$ for all $|\hat{r}| < |r|$ and investigate $\tilde{x}^{(\mathrm{s})}_{kn,r}(t)$. At the order $|r|$, substituting $\tilde{x}^{(\mathrm{s})}_{kn,\hat{r}}(t) \equiv 0$ in (A.32) while considering (A.34) also leads to an LTI system, which is the same as the system (A.32) with $r = \mathrm{O}$. Based on the analysis above for the components of order $r = \mathrm{O}$, one can show that $\tilde{x}^{(\mathrm{s})}_{kn,r}(t) \equiv 0$.

So far, we have shown that, at the limit $k \to \infty$, $\tilde{x}^{(\mathrm{s})}_{kn,\mathrm{O}}(t) \equiv 0$ while $\tilde{x}^{(\mathrm{s})}_{kn,r}(t) \equiv 0$ if $\tilde{x}^{(\mathrm{s})}_{kn,\hat{r}}(t) \equiv 0$ for all $|\hat{r}| < |r|$. By induction, it follows that $x^{(\mathrm{s})}_{kn,r}(t) \equiv 0$ for all r-s. Substituting this into (A.31) implies $\tilde{x}_{kn}(t) \to 0$ as $t \to \infty$ and $k \to \infty$. Since this result is independent of the order of Taylor expansion, it holds when $M \to \infty$ and $R \to \infty$ in (A.30) and (A.31). Considering the range policy function (2.9), we have that the values of ϵ_m are upper bounded for $m = 2, 3, \ldots$ and $\epsilon_m \to 0$ for $m \to \infty$. Moreover, we have $\epsilon^r \to 0$ as $|r| \to \infty$. Therefore, if the components $\tilde{x}^{(\mathrm{s})}_{kn,r}(t) \equiv 0$ for all r-s, it follows that the steady state $\tilde{x}^{(\mathrm{s})}_{kn} \equiv 0$; cf. (A.31).

A.6 Proof of Theorem 12

To prove the asymptotically tracking performance, we use the Lyapunov function

$$L = \frac{\theta_{i,1}}{2} S_i^2 + \frac{1}{2} \tilde{\theta}_i^{\mathrm{T}} \Gamma^{-1} \tilde{\theta}_i \,, \tag{A.52}$$

where $\theta_{i,1}$, S_i, and Γ are given in (4.15), (4.4) and (4.18), respectively, while $\tilde{\theta}_i = \hat{\theta}_i - \theta_i$ denotes the difference between the estimate $\hat{\theta}_i$ and the real value θ_i.

Differentiating (A.52) with respect to time yields

$$\dot{L} = \theta_{i,1} \dot{S}_i S_i + \tilde{\theta}_i^{\mathrm{T}} \Gamma^{-1} \dot{\hat{\theta}}_i \,. \tag{A.53}$$

Based on (4.12) and (4.15), we obtain

$$\begin{aligned} \theta_{i,1} \dot{S}_i &= \theta_{i,1} \dot{v}_i - \theta_{i,1} \big(\dot{v}_{i\mathrm{d}} - \lambda_1 (v_i - v_{i\mathrm{d}}) \big) \\ &= -\theta_i^{\mathrm{T}} w + \delta(v_i, \tilde{v}_{\mathrm{w},i}) + T_{\mathrm{a},i} \,, \end{aligned} \tag{A.54}$$

where the uncertain disturbance $\delta(v_i, \tilde{v}_{\mathrm{w},i})$ and the vector w are given in (4.13) and (4.17), respectively.

Substituting the controller (4.16) into (A.54) yields

$$\theta_{i,1} \dot{S}_i = \tilde{\theta}_i^{\mathrm{T}} w + \delta(v_i, \tilde{v}_{\mathrm{w},i}) - \overline{\delta}(v_i) \mathrm{sgn}(S_i) - \lambda_2 S_i \,. \tag{A.55}$$

Substituting this into (A.53) yields

$$\begin{aligned} \dot{L} &= S_i \tilde{\theta}_i^{\mathrm{T}} w + S_i \delta(v_i, \tilde{v}_{\mathrm{w},i}) - S_i \overline{\delta}(v_i) \mathrm{sgn}(S_i) - \lambda_2 S_i^2 + \tilde{\theta}_i^{\mathrm{T}} \Gamma^{-1} \dot{\hat{\theta}}_i \\ &= \tilde{\theta}_i^{\mathrm{T}} (S_i w + \Gamma^{-1} \dot{\hat{\theta}}_i) + S_i \delta(v_i, \tilde{v}_{\mathrm{w},i}) - S_i \overline{\delta}(v_i) \mathrm{sgn}(S_i) - \lambda_2 S_i^2 \,. \end{aligned} \tag{A.56}$$

Considering the adaptation law (4.18) in (A.56), we obtain

$$\begin{aligned} \dot{L} &= S_i \delta(v_i, \tilde{v}_{\mathrm{w},i}) - |S_i| \overline{\delta}(v_i) - \lambda_2 S_i^2 \\ &\leq |S_i| \big(\big| \delta(v_i, \tilde{v}_{\mathrm{w},i}) \big| - \overline{\delta}(v_i) \big) - \lambda_2 S_i^2 \\ &\leq -\lambda_2 S_i^2 \,, \end{aligned} \tag{A.57}$$

cf. (4.14). Since $\dot{L}$ is negative semi-definite, it follows that $L(t) \leq L(0)$ so that S_i and $\tilde{\theta}_i$ are bounded, which implies that the difference between the desired state and the real state $x_{i\mathrm{d}} - x_i$ is always bounded.

Consider the worst-case scenario where $\delta(v_i, \tilde{v}_{\mathrm{w},i}) = \mathrm{sgn}(S_i) \overline{\delta}(v_i)$, which corresponds

to the least decaying speed

$$\dot{L} = -\lambda_2 S_i^2 \,, \tag{A.58}$$

cf. (A.57). Differentiating (A.58) with respect to time while considering (4.12) yields

$$\ddot{L} = -\frac{2\lambda_2}{\theta_{i,1}} S_i \big(\tilde{\theta}_i^{\mathrm{T}} w + \delta(v_i, \tilde{v}_{\mathrm{w},i}) - \overline{\delta}(v_i) \mathrm{sgn}(S_i) - \lambda_2 S_i \big) \,. \tag{A.59}$$

In practice, the vehicle speed v_i and the inclination angle ϕ_i are both bounded such that the vector w is also bounded. Thus, $\ddot{L}$ is always bounded, implying that $\dot{L}$ is uniformly continuous [83]. Since L is positive definite while $\dot{L}$ is semi-negative definite and also uniformly continuous, based on the Barbalet's lemma [83], we have $\dot{L} \to 0$, i.e., $S_i \to 0$, as $t \to \infty$; cf. (A.58). For non-worst-case scenarios, we have $\dot{L} < -\lambda_2 S_i^2$ when $S_i \neq 0$, and thus, L decays at a faster speed until $S_i = 0$. At the sliding surface $S_i = 0$, we have $s_i \to s_{i\mathrm{d}}$ and $v_i \to v_{i\mathrm{d}}$ as $t \to \infty$; cf. (4.15).

A.7 Proof of Theorem 13

Assuming that all vehicles move around their equilibrium, we have

$$\begin{aligned} s_{i-n} - s_i &= s_{i-n}^* - s_i^* + \tilde{d}_{i,j} \,, \\ v_{i-n} &= v^* + \tilde{v}_{i-n} \,, \end{aligned} \tag{A.60}$$

where $s_j^* - s_i^* \equiv d_{i,j}^*$ and v^* can be seen as the constant components in the Fourier series of $s_j - s_i$ and v_j while the perturbations $\tilde{d}_{i,j}$ and $\tilde{v}_j$ are composed of all sinusoidal terms of the Fourier series. Note that the measurement noises may also be included in $\tilde{d}_{i,j}$ and $\tilde{v}_j$. When the perturbations have zero means, it follows that

$$\mathbb{E}_{m=1}^k \big[\tilde{d}_{i,j}(t_m) \big] \to 0 \,, \quad \mathbb{E}_{m=1}^k \big[\tilde{v}_j(t_m) \big] \to 0 \,, \tag{A.61}$$

as $k \to \infty$.

Substituting (A.60) and (A.61) into (5.21) yields

$$\xi_1(t_k) \to s_{i-n}^* - s_{i-1}^* \,, \quad \xi_2(t_k) \to v^* \,, \quad \xi_3(t_k) \to \frac{s_{i-n}^* - s_{i-1}^*}{\overline{l}_{\mathrm{av}} + \overline{H}_{\mathrm{av}}(v^*)} \,, \tag{A.62}$$

as $k \to \infty$. Hence, the steady-state output of link-length estimator (5.24) becomes

$$\hat{n}_{\mathrm{std}} \triangleq \lim_{k \to \infty} \hat{n}(t_k) = \mathrm{int} \left(\frac{s_{i-n}^* - s_{i-1}^*}{\overline{l}_{\mathrm{av}} + \overline{H}_{\mathrm{av}}(v^*)} \right) . \tag{A.63}$$

At the equilibrium, we have

$$s^*_{i-n} - s^*_i = n\big(l_{\mathrm{av}} + H_{\mathrm{av}}(v^*)\big)\,. \tag{A.64}$$

Substituting (A.64) into (A.63) leads to

$$\hat{n}(t_\infty) = \mathrm{int}\left(\frac{l_{\mathrm{av}} + H_{\mathrm{av}}(v^*)}{\overline{l}_{\mathrm{av}} + \overline{H}_{\mathrm{av}}(v^*)} n\right). \tag{A.65}$$

When the condition (5.25) holds, it follows that

$$n - 0.5 < \frac{l_{\mathrm{av}} + H_{\mathrm{av}}(v^*)}{\overline{l}_{\mathrm{av}} + \overline{H}_{\mathrm{av}}(v^*)} n < n + 0.5\,. \tag{A.66}$$

Considering this in (A.65) yields $\hat{n}(t_k) \to n$ as $t \to \infty$, which completes the proof.

APPENDIX B

Physical Vehicle Parameters

Parameter	Value
Mass (m)	15876 [kg]
Aerodynamic Drag Coefficient (k)	3.8448 [$\mathrm{kg/m}$]
Tire Rolling Radius (R)	0.5040 [m]
Tire Rolling Resistance Coefficient (γ)	0.006
Engine Rotational Inertia (J)	5 [$\mathrm{kg \cdot m^2}$]
Gravitational Constant (g)	9.81 [$\mathrm{m/s^2}$]
Maximum Engine Torque	2314.3 [$\mathrm{N \cdot m}$]
Number of Forward Gears	10
1st Gear Ratio	12.94
2nd Gear Ratio	9.29
3rd Gear Ratio	6.75
4th Gear Ratio	4.90
5th Gear Ratio	3.62
6th Gear Ratio	2.64
7th Gear Ratio	1.90
8th Gear Ratio	1.38
9th Gear Ratio	1.00
10th Gear Ratio	0.74
Final Drive Ratio	3.73

BIBLIOGRAPHY

[1] X. Zeng, K. Balke, and P. Songchitruksa, "Potential connected vehicle applications to enhance mobility, safety, and environmental security," Texas Transportation Institute, Tech. Rep., 2012.

[2] G. Dimitrakopoulos and P. Demestichas, "Intelligent transportation systems," *IEEE Vehicular Technology Magazine*, vol. 5, no. 1, pp. 77–84, 2010.

[3] J. Zhang, F.-Y. Wang, K. Wang, W.-H. Lin, X. Xu, and C. Chen, "Data-driven intelligent transportation systems: A survey," *IEEE Transactions on Intelligent Transportation Systems*, vol. 12, no. 4, pp. 1624–1639, 2011.

[4] G. Marsden, M. McDonald, and M. Brackstone, "Towards an understanding of adaptive cruise control," *Transportation Research Part C: Emerging Technologies*, vol. 9, no. 1, pp. 33–51, 2001.

[5] A. Vahidi and A. Eskandarian, "Research advances in intelligent collision avoidance and adaptive cruise control," *IEEE Transactions on Intelligent Transportation Systems*, vol. 4, no. 3, pp. 143–153, 2003.

[6] J. Zhou and H. Peng, "Range policy of adaptive cruise control vehicles for improved flow stability and string stability," *IEEE Transactions on Intelligent Transportation Systems*, vol. 6, no. 2, pp. 229–237, 2005.

[7] L. Xiao and F. Gao, "A comprehensive review of the development of adaptive cruise control systems," *Vehicle System Dynamics*, vol. 48, no. 10, pp. 1167–1192, 2010.

[8] B. Ganji, A. Z. Kouzani, S. Y. Khoo, and M. Shams-Zahraei, "Adaptive cruise control of a HEV using sliding mode control," *Experts Systems with Applications*, vol. 41, no. 2, pp. 607–615, 2014.

[9] S. E. Shladover, "Longitudinal control of automotive vehicles in close-formation platoons," *Journal of Dynamic Systems, Measurement, and Control*, vol. 113, no. 2, pp. 231–241, 1991.

[10] S. E. Shladover, D. Su, and X.-Y. Lu, "Impacts of cooperative adaptive cruise control on freeway traffic flow," *Transportation Research Record: Journal of the Transportation Research Board*, vol. 2324, no. 1, pp. 63–70, 2012.

[11] S. I. Guler, M. Menendez, and L. Meier, "Using connected vehicle technology to improve the efficiency of intersections," *Transportation Research Part C: Emerging Technologies*, vol. 46, pp. 121–131, 2014.

[12] V. Milanés and S. E. Shladover, "Handling cut-in vehicles in strings of cooperative adaptive cruise control vehicles," *Journal of Intelligent Transportation Systems*, vol. 20, no. 2, pp. 178–191, 2016.

[13] D. Caveney, "Cooperative vehicular safety applications," *IEEE Control Systems Magazine*, vol. 30, no. 4, pp. 38–53, 2010.

[14] Y. Li, H. Wang, W. Wang, L. Xing, S. Liu, and X. Wei, "Evaluation of the impacts of cooperative adaptive cruise control on reducing rear-end collision risks on freeways," *Accident Analysis & Prevention*, vol. 98, pp. 87–95, 2017.

[15] C. Suthaputchakun, Z. Sun, and M. Dianati, "Applications of vehicular communications for reducing fuel consumption and CO_2 emission: the state of the art and research challenges," *IEEE Communications Magazine*, vol. 50, no. 12, pp. 108–115, 2012.

[16] S. Tsugawa, "An overview on an automated truck platoon within the Energy ITS project," in *IFAC Symposiums on Advances in Automotive Control*, vol. 46, no. 21, 2013, pp. 41–46.

[17] D. Jiang, A. Meier, W. Holfelder, and R. Herrtwich, "Design of 5.9 GHz DSRC-based vehicular safety communication," *IEEE Wireless Communications*, vol. 13, no. 5, pp. 36–43, 2006.

[18] "United States Department of Transportation," http://www.its.dot.gov/factsheets/dsrc_factsheet.htm.

[19] J. B. Kenney, "Dedicated short-range communications (DSRC) standards in the United States," in *Proceedings of the IEEE*, vol. 99, no. 7, 2011, pp. 1162–1182.

[20] Y. L. Morgan, "Notes on DSRC & WAVE standards suite: Its architecture, design, and characteristics," *IEEE Communication Survey & Tutorials*, vol. 12, no. 4, pp. 504–518, 2010.

[21] M. Bando, K. Hasebe, K. Nakanishi, and A. Nakayama, "Analysis of optimal velocity model with explicit delay," *Physical Review E*, vol. 58, no. 5, pp. 5429–5435, 1998.

[22] P. J. Jin, D. Yang, B. Ran, M. Cebelak, and C. M. Walton, "Bi-directional control characteristics of General Motors (GM) and optimal velocity car-following models: implications for coordinated driving in connected vehicle environment," *Transportation Research Record: Journal of the Transportation Research Board*, vol. 2381, pp. 110–119, 2013.

[23] J. C. Zegers, E. Semsar-Kazerooni, J. Ploeg, N. van de Wouw, and H. Nijmeijer, "Consensus-based bi-directional CACC for vehicular platooning," in *American Control Conference*, 2016, pp. 2578–2584.

[24] G. J. L. Naus, R. P. A. Vugts, J. Ploeg, M. J. G. van de Molengraft, and M. Steinbuch, "String-stable CACC design and experimental validation: A frequency-domain approach," *IEEE Transactions on Vehicular Technology*, vol. 59, no. 9, pp. 4268–4279, 2010.

[25] R. Kianfar, B. Augusto, A. Ebadighajari, U. Hakeem, J. Nilsson, A. Raza, R. S. Tabar, N. V. Irukulapati, C. Englund, P. Falcone, S. Papanastasiou, L. Svensson, and H. Wymeersch, "Design and experimental validation of a cooperative driving system in the grand cooperative driving challenge," *IEEE Transactions on Intelligent Transportation Systems*, vol. 13, no. 3, pp. 994–1007, 2012.

[26] M. R. I. Nieuwenhuijze, T. van Keulen, S. Öncü, B. Bonsen, and H. Nijmeijer, "Cooperative driving with a heavy-duty truck in mixed traffic: experimental results," *IEEE Transactions on Intelligent Transportation Systems*, vol. 13, no. 3, pp. 1026–1032, 2012.

[27] J. Ploeg, E. Semsar-Kazerooni, G. Lijster, N. van de Wouw, and H. Nijmeijer, "Graceful degradation of cooperative adaptive cruise control," *IEEE Transactions on Intelligent Transportation Systems*, vol. 16, no. 1, pp. 488–497, 2015.

[28] J. I. Ge and G. Orosz, "Dynamics of connected vehicle systems with delayed acceleration feedback," *Transportation Research Part C*, vol. 46, pp. 46–64, 2014.

[29] W. B. Qin, M. M. Gomez, and G. Orosz, "Stability and frequency response under stochastic communication delays with applications to connected cruise control design," *IEEE Transactions on Intelligent Transportation Systems*, p. (published online), 2016.

[30] G. Guo and W. Yue, "Sampled-data cooperative adaptive cruise control of vehicles with sensor failures," *IEEE Transactions on Intelligent Transportation Systems*, vol. 15, no. 6, pp. 2404–2418, 2014.

[31] A. Alam, J. Mårtensson, and K. H. Johansson, "Experimental evaluation of decentralized cooperative cruise control for heavy-duty vehicle platooning," *Control Engineering Practice*, vol. 38, pp. 11–25, 2015.

[32] D. Yanakiev and I. Kanellakopoulos, "Nonlinear spacking policies for automated heavy-duty vehicles," *IEEE Transactions on Vehicular Technology*, vol. 47, no. 4, pp. 1365 – 1377, 1998.

[33] S. S. Avedisov and G. Orosz, "Nonlinear network modes in cyclic systems with applications to connected vehicles," *Journal of Nonlinear Science*, vol. 4, pp. 1015–1049, 2015.

[34] R. Rajamani and S. E. Shladover, "An experimental comparative study of autonomous and cooperative vehicle-follower control systems," *Transportation Research Part C: Emerging Technologies*, vol. 9, no. 1, pp. 15–31, 2001.

[35] V. Milanés and S. E. Shladover, "Modeling cooperative and autonomous adaptive cruise control dynamic response using experimental data," *Transportation Research Part C: Emerging Technologies*, vol. 48, pp. 285–300, 2014.

[36] S. Sheikholeslam and C. A. Desoer, "Longitudinal control of a platoon of vehicles with no communication of lead vehicle information: a system level study," *IEEE Transactions on Vehicular Technology*, vol. 42, no. 4, pp. 546 – 554, 1993.

[37] X. Liu, A. Goldsmith, S. S. Mahal, and J. K. Hedrick, "Effects of communication delay on string stability in vehicle platoons," in *Proceedings of IEEE Intelligent Transportation Systems Conference*, 2001, pp. 625 – 630.

[38] P. Seiler, A. Pant, and K. Hedrick, "Disturbance propagation in vehicle strings," *IEEE Transactions on Automatic Control*, vol. 49, no. 10, pp. 1835–1842, 2004.

[39] A. A. Peters, R. H. Middleton, and O. Mason, "Leader tracking in homogeneous vehicle platoons with broadcast delays," *Automatica*, vol. 50, no. 1, pp. 64–74, 2014.

[40] T. Robinson, E. Chan, and E. Coelingh, "Operating platoons on public motorways: an introduction to the SARTRE platooning programme," in *Proceeings of the 17th World Congress on Intelligent Transport Systems*, 2010, pp. 1–11.

[41] A. Geiger, M. Lauer, F. Moosmann, B. Ranft, H. Rapp, C. Stiller, and J. Ziegler, "Team AnnieWAY's entry to the 2011 grand cooperative driving challenge," *IEEE Transactions on Intelligent Transportation Systems*, vol. 13, no. 3, pp. 1008–1017, 2012.

[42] L. Zhang and G. Orosz, "Motif-based design for connected vehicle systems in presence of heterogeneous connectivity structures and time delays," *IEEE Transactions on Intelligent Transportation Systems*, vol. 17, no. 6, pp. 1638–1651, 2016.

[43] J. I. Ge and G. Orosz, "Optimal control of connected vehicle systems," in *Proceedings of IEEE Conference on Decision and Control*, 2014, pp. 4107–4112.

[44] L. Zhang and G. Orosz, "Nonlinear dynamics of connected vehicle systems with communication delays," in *Proceedings of the American Control Conference*, 2015, pp. 2759–2764.

[45] ——, "Stability analysis of nonlinear connected vehicle systems," in *Proceedings of the ASME Dynamic Systems and Control Conference*, no. DSCC2014-6358, 2014, p. V001T10A006.

[46] ——, "Consensus and disturbance attenuation in multi-agent chains with nonlinear control and time delays," *International Journal of Robust and Nonlinear Control*, p. (published online), 2016.

[47] Y. Zheng, S. E. Li, J. Wang, D. Cao, and K. Li, "Stability and scalability of homogeneous vehicular platoon: Study on the influence of information flow topologies," *IEEE Transactions on Intelligent Transportation Systems*, vol. 17, no. 1, pp. 14–26, 2016.

[48] K. C. Dey, L. Yan, X. Wang, Y. Wang, H. Shen, M. Chowdhury, L. Yu, C. Qiu, and V. Soundararaj, "A review of communication, driver characteristics, and controls aspects of cooperative adaptive cruise control," *IEEE Transactions on Intelligent Transportation Systems*, vol. 17, no. 2, pp. 491–509, 2016.

[49] L. Zhang and G. Orosz, "Designing network motifs in connected vehicle systems: delay effects and stability," in *Proceedings of the ASME Dynamic Systems and Control Conference*, no. DSCC2013-4081, 2013, p. V003T42A006.

[50] G. Orosz, "Connected cruise control: modeling, delay effects, and nonlinear behavior," *Vehicle System Dynamics*, vol. 54, no. 8, pp. 1147–1176, 2016.

[51] U. Alon, *An introduction to systems biology: deisgn principles of biological circuits*. CRC Press, Taylor & Francis Group, 2007.

[52] D. Hajdu, L. Zhang, T. Insperger, and G. Orosz, "Robust stability analysis for connected vehicle systems," in *Proceedings of the 13th IFAC Workshop on Time-Delay Systems*, 2016, pp. 165–170.

[53] L. Zhang and G. Orosz, "Connected vehicle systems with nonlinear dynamics and time delays," in *Proceedings of the 12th IFAC Workshop on Time-Delay Systems*, 2015, pp. 370–375.

[54] L. Zhang, C. He, J. Sun, and G. Orosz, "Hierarchical design for connected cruise control," in *Proceedings of ASME Dynamic Systems and Control Conference*, no. DSCC2015-9993, 2015, p. V001T17A005.

[55] L. Zhang, J. Sun, and G. Orosz, "Hierarchical design of connected cruise control in presence of heterogeneous information delays and uncertain dynamics," *IEEE Transactions on Control Systems Technology*, p. (submitted), 2016.

[56] L. Zhang and G. Orosz, "Black-box modeling of connected vehicle networks," in *Proceedings of the American Control Conferences*, 2016, pp. 2421–2426.

[57] ——, "Beyond-line-of-sight dynamics estimation in connected vehicle networks," *IEEE Transactions on Intelligent Transportation Systems*, p. (to be submitted), 2016.

[58] A. G. Ulsoy, H. Peng, and M. Çakmakci, *Automotive Control Systems*. Cambridge University Press, 2012.

[59] G. Orosz, R. E. Wilson, and G. Stépán, "Traffic jams: dynamics and control," *Philosophical Transactions of the Royal Society A*, vol. 368, no. 1928, pp. 4455–4479, 2010.

[60] S. Sheikholeslam and C. A. Desoer, "Control of interconnected dynamic systems: the platoon problem," *IEEE Transactions on Automatic Control*, vol. 37, no. 6, pp. 806–810, 1992.

[61] X. Y. Lu, S. Shladover, and J. K. Hedrick, "Heavy-duty truck control: short inter-vehicle distance following," in *Proceedings of the American Control Conference*, 2004, pp. 4722–4727.

[62] F. Bai and H. Krishnan, "Reliability analysis of DSRC wireless communciation for vehicle safety applications," in *IEEE Intelligent Transporation Systems Conference*, Toronto, Canada, 2006, pp. 355–362.

[63] K. H. Rosen, *Discrete mathematics and its applications, 7th edition*. McGraw-Hill, 2012.

[64] S.-I. Niculescu, *Delay effects on stability: a robust control approach*. Springer, 2001.

[65] K. Zhou, J. C. Doyle, and K. Glover, *Robust and optimal control*. Prentice Hall, 1996.

[66] T. Insperger and G. Stépán, *Semi-discretization for time-delay systems*. Springer, 2011.

[67] C. A. Rabbath and N. Léchevin, *Discrete-time contrl system design with applications*. Springer, 2014.

[68] P. Wagner, "Fluid-dynamical and microscopic description of traffic flow: a data-driven comparison," *Philosophical Transactions of the Royal Society A*, vol. 368, no. 1928, pp. 4481–4495, 2010.

[69] K. Engelborghs, T. Luzyanina, and G. Samaey, "DDE-BIFTOOL v. 2.00: a Matlab package for bifurcation analysis of delay differential equations," Department of Computer Science, Katholieke Universiteit Leuven, Belgium, Tech. Rep. TW-330, 2001.

[70] A. Ben-Israel and R. Gilbert, *Computer-Supported Calculus*. Springer, 2002.

[71] G. Franzè, D. Famularo, and A. Casavola, "Constrained nonlinear polynomial time-delay systems: a sum-of-squares approach to estimate the domain of attraction," *IEEE Transactions on Automatic Control*, vol. 57, no. 10, pp. 2673–2679, 2012.

[72] H. K. Khalil, *Nonlinear Systems (3rd Edition)*. New Jersey: Prentice Hall, 2002.

[73] V. Marinca and N. Herisanu, *Nonlinear Dynamical Systems in Engineering: Some Approximate Approaches*. Springer, 2011.

[74] P. Setlur, J. R. Wagner, D. M. Dawson, and D. Braganza, "A trajectory tracking steer-by-wire control system for ground vehicles," *IEEE Transactions on Vehicular Technology*, vol. 55, no. 1, pp. 76–85, 2006.

[75] D. Swaroop, J. K. Hedrick, and S. B. Choi, "Direct adaptive longitudinal control of vehilce platoons," *IEEE Transactions on Vehicluar Technology*, vol. 50, no. 1, pp. 150–161, 2001.

[76] B. Bandyopadhyay, S. Janardhanan, and S. K. Spurgeon, *Advances in sliding mode control: concept, theory and implementation*. Springer, 2013.

[77] P. A. Ioannou and J. Sunc, *Robust adaptive control*. Prentice Hall, 1996.

[78] C. R. He, H. Maurer, and G. Orosz, "Fuel consumption optimization of heavy-duty vehicles with grade, wind, and traffic information," *ASME Journal of Computational and Nonlinear Dynamics*, vol. 11, no. 6, p. 061011, 2016.

[79] "UMTRI Safety Pilot," http://safetypilot.umtri.umich.edu/.

[80] J. L. Torres, A. García, M. D. Blas, and A. D. Francisco, "Forecast of hourly average wind speed with ARMA models in navarre (spain)," *Solar Energy*, vol. 79, no. 1, pp. 65–77, 2005.

[81] C. M. Bishop, *Pattern recognition and machine learning*. Springer, 2006.

[82] T. Kanungo, D. M. Mount, N. S. Netanyahu, C. D. Piatko, R. Silverman, and A. Y. Wu, "An efficient k-means clustering algorithm: analysis and implementation," *IEEE Transactions on Pattern Analysis and Machine Intelligence*, vol. 24, no. 7, pp. 881–892, 2002.

[83] J.-J. E. Slotine and W. Li, *Applied Nonlinear Control*. Prentice Hall, 1991.